NONLINEAR INDUCED-CHARGE ELECTROKINETICS

By

ZHEMIN WU

Dissertation

Submitted to the Faculty of the

Graduate School of Vanderbilt University

in partial fulfillment of the requirements

for the degree of

DOCTOR OF PHILOSOPHY

in

Mechanical Engineering

December, 2008

Nashville, Tennessee

Approved:

Professor Dongqing Li

Professor Robert W. Pitz

Professor Deyu Li

Professor Taylor G. Wang

Professor John P. Wikswo

ACKNOWLEDGMENTS

I am grateful to all of those who made this dissertation possible. First and foremost, I would like to express my sincere gratitude to my advisor, Prof. Dongqing Li, for his guidance and help during my whole Ph.D. period. Appreciation also goes to other members of my dissertation committee, Dr. Robert W. Pitz, Dr. Taylor G. Wang, Dr. Deyu Li and Dr. John P. Wikswo for their precious time examining my dissertation. I would also like to thank Dr. Guoqin Hu and Mr. Yandong Gao for the valuable discussions about the numerical simulations of particle motions. Valuable help from fellow members and graduate students, Mr. Yuejun kang, Mr. Barbaros Cetin, Dr. Xiangchun Xuan, Mr. Jacky Lee and Mr. Xudong Wu is also highly appreciated.

This work would not have been possible without the financial support from Vanderbilt University and H Fort Flowers Fund.

VITA

Zhemin Wu was born on May 27th, 1978, in Hangzhou, Zhejiang, People's Republic of China. He obtained Bachelor of Science degree in July 2001 after four years undergraduate study at Shanghai University, Shanghai, China. After that, He continued his study at the same university and received Master of Science degree in July 2004. In September 2004, he joined University of Toronto, Toronto, Canada as a graduate student for a Ph.D. degree in Mechanical Engineering. In October 2005, he transferred to the Department of Mechanical at Vanderbilt University, Nashville, Tennessee, U.S.

LIST OF PUBLICATIONS

Refereed Journals

1. **Zhemin Wu**, Yandong Gao, Dongqing Li, "*Electrophoretic motion of ideally polarizable particles in a microchannel*", Electrophoresis, 2008 (accepted)

2. Yuejun Kang, Barbaros Cetin, **Zhemin Wu**, Dongqing Li, "*Continuous Particle Separation with Localized AC-Dielectrophoresis Using Embedded Electrodes and an Insulating Hurdle*", Electrochimica Acta, 2008 (accepted)

3. Barbaros Cetin, Yuejun Kang, **Zhemin Wu**, Dongqing Li, "*Continuous particle separation by size via AC-dielectrophoresis using a lab-on-a-chip device with 3D electrodes*", Electrophoresis, 2008 (accepted)

4. **Zhemin Wu,** Dongqing Li, "*Micromixing using induced-charge electrokinetic flow*", Electrochimica Acata, 2008, 53(19): 5827-5835

5. **Zhemin Wu,** Dongqing Li, "*Mixing and flow regulating by induced-charge electrokinetic flow in a microchannel with a pair of conducting triangle hurdles*", Microfluidics and Nanofluidics, 2008, 5(1): 65-76

6. Jacky S.H. Lee, Irena Barbulovic-Nad, **Zhemin Wu**, Xiangchun Xuan, "*Electrokinetic flow in a free surface-guided microchannel*", Journal of Applied Physics, 2006, 99(5): 054905

7. **Zhemin Wu**, Chi Chen, Gaolian Liu, "*Multipoint Inverse Shape Design of Airfoils Based On Variable-Domain Variational Principle*", Aircraft Engineering and Aerospace Technology, 2004, 76(4): 376-383

8. **Zhemin Wu**, Hong Li, Gaolian Liu, "*A New Characteristics-Based Finite Difference Method for Hyperbolic Partial Differential Equations*", International Journal of Turbo and Jet Engines, 2004, 21(1): 39-46

9. Liqun Chen, **Zhemin Wu**, "*Amplitude-Frequency Characteristics of Nonlinear Vibration of a Serpentine Belt Drive System*", Engineering Mechanics, 2003, 20(1): 149-152

10. Liqun Chen, **Zhemin Wu**, "*Averaging Method for Analyzing a Multi-Degrees-of-Freedom Nonlinear Oscillation*", Journal of Vibration and Shock, 2002, 21(3): 63-64

11. Liqun Chen, **Zhemin Wu**, "*The Averaging Analysis of a Dumped Oscillator with Dry Friction*", Journal of Shangqiu Teachers College, 2002, 18(2): 1-2

Conference papers

1. **Zhemin Wu,** Dongqing Li, " *Mixing Enhancement by Induced-Charge Electrokinetic Flow*", Proceedings of MNHT2008 Micro/Nanoscale Heat Transfer International Conference, 2008, Tainan, Taiwan

ABSTRACT

This dissertation presents the study of non-linear induced-charge electrokinetic phenomena and the corresponding applications. The study shows that a nonlinear induced surface charge distribution is immediately caused when a conducting object is immersed in an external applied electric field. The induced charge on the conducting surfaces results in a non-linear zeta potential distribution when the surfaces contact with an aqueous buffer solution. The non-constant zeta potential gives a varying slipping velocity along the conducting surface, which produces micro vortexes in the liquid. A numerical scheme is suggested to estimate the induced zeta potential on the conducting surfaces. The induced-charge electrokinetic flows (ICEKF) in a microchannel with embedded conducting hurdles are studied. Two-dimensional pressure-linked Navier-Stokes equation is used to model the flow field in the channel. The numerical results show flow circulations generated from the induced non-uniform zeta potential distribution along the conducting hurdle surfaces, which provide effective means to enhance the flow mixing between different solutions. The mixing enhancement effect is experimentally validated using PDMS based microchannels with embedded platinum hurdles. The dependence of the degree of mixing enhancement on the hurdle geometries and hurdle numbers is also predicted. It's also found that, by adjusting the electric field applied through the microchannel with an asymmetric conducting triangle hurdle pair, an electrokinetic flow regulating effect can be obtained and this effect depends on the dimensions of the conducting converging-diverging section. The induced-charge electrophoretic (ICEP) motions of conducting particles in microchannel are also numerically studied. A complete theoretical model of ICEP motion is set up and a moving grid technique is utilized to fulfill the numerical simulation of the particle-liquid coupled multi-physics system under various conditions. The corresponding effects of micro vortex generation, particle-wall interaction and particle-particle interaction are discussed. The unique wall-lifting effect of the ICEP motion of conducting particles in a microchannel and the attracting and repelling effects between two conducting particles in an unbounded large field are investigated. The induced-charge electrokinetics described in this study can be used in various microfluidics and lab-on-a- chip (LOC) applications.

TABLE OF CONTENTS

Page

Chapter

IV. INDUCED-CHAGE ELECTROPHORESIS OF CONDUCTING PARTICLES 65

LIST OF FIGURES

Figure Page

LIST OF TABLES

Table Page

CHAPTER I

INTRODUCTION

Recent developments in micro-fabrication technology have led to advances in microelectronics and computer technology with a super fast speed, which constantly change the way we live and work. Scientists and engineers have already realized the advantages and the application potentials of the micro-fabrication technology in the fields of mechanical engineering and biomedical engineering, which leads to the rapid development of microfluidic lab-on-a-chip (LOC) devices. A microfluidic lab-on-a-chip device is a micro-scale chemical or biological laboratory built on a small silicon or glass chip with a network of microchannels, electrodes, actuators, sensors and the electronic circuits. The miniaturized lab-on-a-chip can duplicate the specific biological or chemical analysis as the normal room-sized counterparts, including sample treatment, transport, reaction, and detection. The lab-on-a-chip devices show tremendous advantages over the conventional instruments, such as dramatic reduction in the amount of reagents, short reaction and analysis time, high throughput, automation and portability (Knight 2002; Freemantle 1999; Wickelgren 1998; Sinha 1999; Borman 1999).

Electrokinetic phenomena, including electroosmosis, electrophoresis and dielectrophoresis, provide one of the most important non-mechanical techniques in microfluidic devices. The basic idea behind electrokinetic phenomena is as follows: a rearrangement of ions in an aqueous liquid solution occurs when the liquid contacts with a charged solid surface, where an electric double layer (EDL) with a diffuse cloud of oppositely charged counter ions is built up to balance the surface charge. An externally applied electric field gives a body force on the charged diffuse ions layer, driving the ions and the bulk liquid into a motion relative to the solid-liquid interface. The electrokinetic flow around stationary surfaces is referred as electroosmotic flow (EOF), and the electrokinetic migration of freely suspended particles is referred as electrophoresis (EP).

The standard electrokinetic flow involves the interaction between the applied electric field and the electric double layer near a non-conducting surface with fixed electric charge, or equivalently fixed zeta potential, which is defined as the potential drop across the screening cloud of the EDL. The velocity of the resultant fluid flow is linearly proportional to the applied electric field (Hunter 1981). Generally, the linear electrokinetically-driven flows in microchannels are laminar because of the slow velocity and small characteristic length scale and thus small Reynolds number ($\mathrm{Re} << 1$). The micro-scale mixing of miscible fluids must thus occur without the benefit of turbulence, by molecular diffusion alone. In a typical microfluidic devices using linear electrokinetic flow, the mixing time can be prohibitively long. Another limitation arises because of the difficulties of the flow control using simple uniform electrokinetically-driven flows. Additional mechanical parts such as membrane pumps and valves are needed with different actuation methods including piezoelectric or thermopneumatic actuations (Laser and Santiago 2004).

The variants to this basic picture and the nonlinearity in electrokinetics have recently been explored. As the first study, Anderson pointed out that counter-intuitive effects occur with the surfaces having spatially heterogeneous zeta-potential distributions (Anderson 1985). Eddies and flow circulations were found in inhomogeneously charged pores (Anderson & Idol 1985). The surface charge heterogeneity was utilized for both flow control and mixing enhancement in microchannels. Ajdari (1995, 2002) and Stroock et al. (2000) indicated that a net electro-osmotic flow could be driven either parallel or perpendicular to an applied field by modulating the surface and charge density of a microchannel, and Gitlin et al. (2003) have implemented these ideas to make a ‘transverse electrokinetic pump’. Such transverse pumps have the advantage that a strong field can be established with a low voltage applied across a narrow channel. As the second application, surface charge heterogeneities have been suggested as a mechanism for enhanced mixing in electroosmotic flows (Erickson & Li 2002; Stroock et al. 2000; Barker et al. 2000; Hau et al. 2003). The method was further extended with a non-uniform distribution of zeta potential along the channel wall to generate micro flow circulation to enhance the mixing between two solutions (Biddiss et al. 2004). The surface charge heterogeneity can be achieved either by chemical surface patterning (Liu et al. 2000) or by auxiliary electrode induction (Lee et al. 1990; Hayes & Ewing 1992; Schasfoort et al. 1999), and both require complex special fabrication treatments.

Nonlinear electrokinetic flows around polarizable (metallic or dielectric) objects have been studied in the recent decades. The phenomena falls into two major categories:

second-kind electrokinetics and induced-charge electrokinetics (ICEK). Second-kind electrokinetic flow refers to the flow occurring around ion-selective porous granules subject to very large applied electric field. The large electric field generates strong currents of certain ions through the conducting surface, and leads to large concentration polarization and space charge in the bulk electrolyte, which interact with the applied field to produce fluid motion. The similar phenomena occur near the surface of non-porous conducting colloids undergoing strong electrochemical reactions with very large Faradaic currents. The effect was extensively studied by Dukhin (1991), Barany et al (1998) and Ben & Chang (2002, 2004). The major disadvantages of the second-kind electrokinetics are the involvement of large applied electric field and strong surface and bulk chemical reactions, which prevent the second-kind electrokinetics from being applied to most bio-medical applications.

Induced-charge electrokinetics occurs near a polarizable object when an applied electric field acts on the double-layer charge that is induced by the electric field itself, resulting in micro flow circulations near the object. Levich (1962) first calculated the perturbed slip profile around a polarizable sphere in an external electric field using the induced-charge double layer concept. Gamayunov, Murtsovkin & Dukhin (1986) and Dukhin & Murtsovkin (1986) first calculated the nonlinear electro-osmotic flow arising from double-layer polarization around a spherical conducting particle, and Dukhin (1986) extended this calculation to include a dielectric surface coating (as a model of a dead biological cell). The idea was experimentally proved by Murtsovkin (1996), who demonstrated that an alternating electric (AC) field can drive steady quadrupolar flow around a polarizable particle. The effect has recently been unified using the term 'induced-charge electro-osmosis' (ICEO) (Squires & Bazant 2004), which refers the nonlinear electroosmotic flow resulting from the action of an electric field on its own induced nonlinear diffuse charge distribution near a polarizable solid surface. And a complex general theoretical model of ICEO was systematically set up (Squires & Bazant 2004).

Induced-charge electrokinetic phenomena provide promising application potentials with lab-on-a-chip devices. The application of induced-charge electroosmosis for mixing enhancement with microelectrode arrays and streaming flow pumping with asymmetric conducting bodies using AC electric field were theoretically predicted (Squires & Bazant 2004; Squires & Bazant 2006; Bazant & Ben 2006). So far, the investigated applications of ICEO are purely based on complicated fabrications of complex microelectrode arrays and no further flow controlling effect other than pumping was studied. On the other hand, with the rapid development of microfluidics and nanotechnology, various electrically conducting and polarizable particles (e.g., carbon, gold, silver, and nickel) are involved in microfluidic systems for variety of applications such as biochemical sensing, separation and particle production (Lin et al. 2007; Sparks et al. 2003; Shim et al. 2008; Boleininger et al. 2006). Thus, it is important to develop fundamental understanding of the electrophoretic motion of electrically polarizable particles. Gamayunov et al (1986) first studied the hydrodynamic interaction between two polarizable particles and calculated the non-linear electro-osmotic flow arising from double-layer polarization around spherical polarizable particles, which was experimentally proved by Murtsovkin (1996). Yariv (2005) developed a general model to calculate the induced-charge electrophoretic (ICEP) velocities of non-spherical polarizable particles. A more systematic theoretical model of ICEP motion of polarizable particles was recently proposed to study the dependence of the ICEP velocities and directions on the effects of broken geometry symmetry (Squires & Bazant 2006). The transient alignment of asymmetric polarizable particles was theoretically studied (Squires & Bazant 2004; Yariv 2005; Squires & Bazant 2006) and similar effect was found in the ICEP dynamics of rod-like metal particles (Rose et al. 2007). Saintillan et al (2006) analyzed far-field hydrodynamic interactions in the ICEP of colloidal rod dispersions using a statistical method. Yossifon et al. (2007) studied the rotational ICEP motion of a polarizable dielectric spheroid in the presence of a uniform arbitrarily oriented external electric field. So far, there is no published work conducting complete transient numerical simulation of ICEP motion of ideally polarizable particles and all the above mentioned systematic theoretical works (Yariv 2005; Squires & Bazant 2006) developed the ICEP models using steady flow approximations on an unbounded large field with no channel wall effects. But for real lab-on-a-chip applications, the existence of channel will definitely affect the particle motion. Also, particle-particle interaction will play another important role on particle's motions and thus is necessary to be investigated.

This dissertation will discuss the work on nonlinear induced-charge electrokinetic phenomena in microchannels and the corresponding lab-on-a-chip applications. The organization of the dissertation is as follows: Chapter I reviews the previous works on the nonlinear electrokinetic phenomena. Chapter II introduces the fundamentals of induced-charge electrokinetics and proposes a simple numerical approach to model the nonlinear induced charge distributions on polarizable surfaces. Chapter III studies the nonlinear induced-charge electroosmotic flows in a microchannel with embedded conducting hurdles are studied and a micro vortex generation mechanism in microchannels is established. The corresponding unique micro-mixing and flow regulating effects are also investigated. Chapter IV discusses the induced-charge electrophoretic (ICEP) motions of conducting particles in a microchannel. A complete theoretical model of ICEP motion is set up and a moving grid technique is utilized to fulfill the numerical simulation of the particle-liquid coupled multi-physics system under various conditions. The corresponding effects of micro vortex generation, particle-wall interaction and particle-particle interaction are discussed. Finally, Chapter V presents the conclusions of this work.

CHAPTER II

FUNDAMENTALS OF INDUCED-CHARGE ELECTROKNIETICS

This chapter presents the fundamentals of induced-charge electrokinetics (ICEK). The basics of electric double layer (EDL) and electrokinetic phenomena are briefly reviewed, based on which the complete theory is set up to describe the induced-charge electrokinetic phenomena when a perfectly polarizable conducting object is immersed in an external applied electric field. The nonlinear induced surface charge distribution at the polarizable surface and the corresponding mechanism of micro vortex generation are introduced. A correction method is suggested to estimate numerically the induced zeta potential on the conducting surface. The numerical simulations perfectly match the analytical solutions. The correction method provides a certain simplification to calculate the needed zeta potential for the study of ICEK behaviors of the objects with arbitrary geometries.

2.1 Electric double layer and electrokinetic phenomena

When a solid contacts with an aqueous solution, the solid surfaces generally carry electrostatic charges, which will attract the counterions in the liquid. The electrostatic attraction causes a rearrangement of the local free ions in the liquid so as to produce a thin region of nonzero net charge (excess counterions) close to the solid-liquid surface, as shown in Figure 2.1. This net charge should balance the charge at the solid surface. The charged surface and the layer of liquid containing the balancing charges are called the electric double layer (EDL) (Hunter 1981). Immediately next to the charged solid surface, there is a layer of ions those are strongly attracted to the solid surface and are immobile. This layer is called the compact layer. From the compact layer to the electrically neutral bulk liquid, the net charge density gradually reduces to zero and the ions in this region are mobile. This region is called the diffuse layer of the EDL. The boundary between the compact layer and the diffuse layer is usually referred as the shear plane. And the electrical potential at the shear plane is called zeta potential, ζ. The zeta potential is considered as an approximation of the surface potential in most electrokinetic models and is given by (Squires & Bazant 2004)

$$\zeta = \frac{q}{\varepsilon\varepsilon_0\kappa} \tag{2.1}$$

where q is the net surface charge, ε is the dielectric constant, ε_0 is the vacuum permittivity and κ^{-1} is the Debye EDL thickness given by

$$\kappa^{-1} = \lambda_D = \sqrt{\frac{\varepsilon_w k_B T}{2n_0(ze)^2}} \tag{2.2}$$

where k_B is the Boltzmann constant, T is the temperature and n_0 is the bulk ionic concentration.

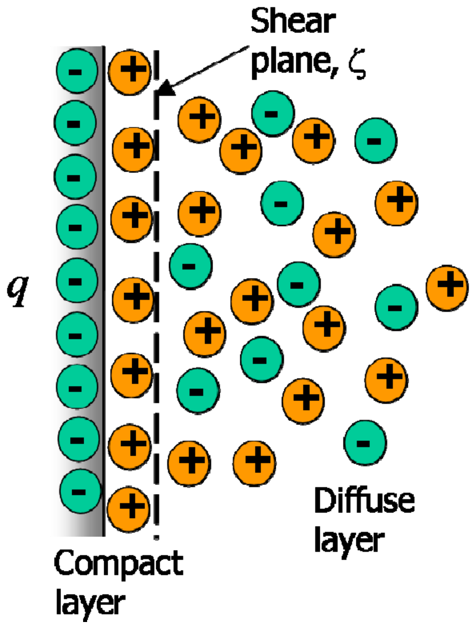

Figure 2.1 Schematic diagram of electric double layer

When an external electric field is applied along a microchannel with the charged channel walls, the applied electric field exerts a body force on the excess counterions in the EDL, driving the ions and thus the bulk liquid into motion. The resulting liquid flow is just called electroosmotic flow (EOF) as shown in Figure 2.2. If the EDL thickness is thin in comparison with the microchannel dimensions, the flow appears to slip just outside the double layer and causes a plug like flow profile. The local slip velocity is given by the well-known Helmholtz-Smoluchowski formula (Hunter 1981):

$$\vec{u} = -\frac{\varepsilon\varepsilon_0\zeta}{\mu}\vec{E} = \mu_{eo}\vec{E} \tag{2.3}$$

where ζ is the zeta potential at the channel wall, μ is the viscosity of the liquid and $\mu_{eo} = -\frac{\varepsilon\varepsilon_0\zeta}{\mu}$ is just so called electroosmotic mobility of the liquid.

The second basic electrokinetic effect, which is called electrophoresis, refers the particle motion in an aqueous liquid solution in response to an applied electric field. When a charged particle is freely suspended in a liquid, the electroosmotic slip velocity mentioned above will give rise to motion of the particle itself, as shown in Figure 2.3. In the thin double layer limit, the electrophoretic velocity of particle is given by Helmholtz-Smoluchowski formula (Hunter 1981)

$$\vec{u}_{ep} = \frac{\varepsilon\varepsilon_0\zeta}{\mu}\vec{E} = \mu_{ep}\vec{E} \tag{2.4}$$

where $\mu_{ep} = \frac{\varepsilon\varepsilon_0}{\mu}$ refers the so called electrophoretic mobility of particle.

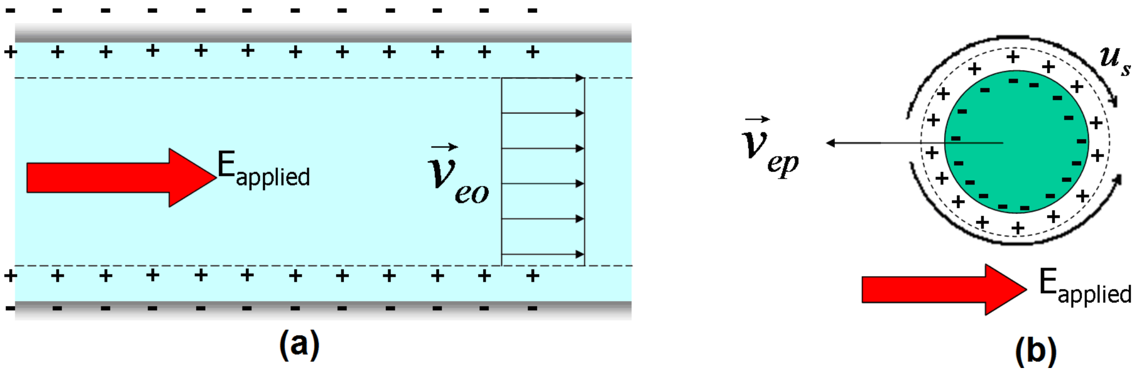

Figure 2.2 Schematic illustration of (a) Electroosmotic flow (b) Electrophoresis of a particle

2.2 Induced-charge electrokinetics

The standard electrokinetic flow involves the interaction between an externally applied electric field and the EDL near a non-conducting surface with fixed electric charge. The velocity of the resultant electroosmotic flow is linearly proportional to the applied electric field (see Eq. (2.3)). However, such a correlation will be very different if the charged surface is ideally polarizable and electrically conducting. To clarify the basic principles of ICEKF, a simple case is considered as shown in Figure 2.3: an arbitrary-shaped conducting object with an ideally polarizable conducting surface immersed in an aqueous solution and under a uniform electric field ($\vec{E}_0$).

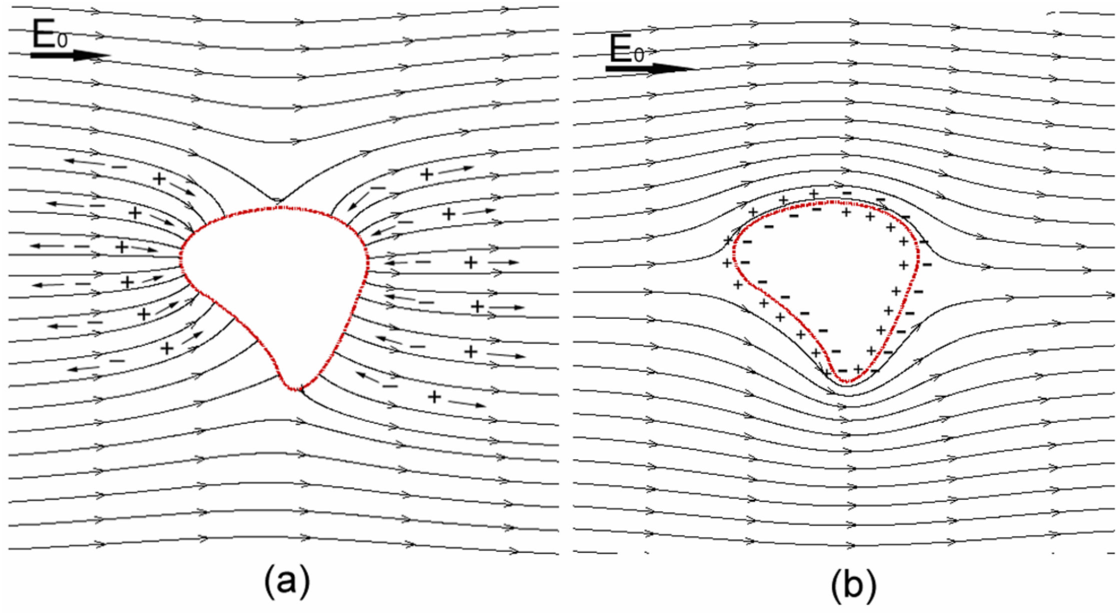

Figure 2.3 Schematic charging process of a conducting object in a uniform applied electric field: a) initial electric field b) steady-state electric field

Once the electric field is suddenly applied over the object, a non-zero current $J = \sigma \vec{E}$ drives ions in the aqueous solution to the conducting surface of the conductivity σ. Thus, the electric field lines initially intersect the conducing surface at right-angles (see Figure 2.3a). The current drives positive ions into a thin layer on one side of the conductor and the negative ions into the other, inducing an equal and opposite surface charge q on the conducting surface and also attracting equal and opposite image charges within the conductor itself. Consequently, a dipolar screening cloud adjacent to the solid-liquid surface is forming. The induced surface charge q and the corresponding induced zeta potential ζ_i change with time (Squires and Bazant 2004), and are given by

$$\frac{\mathrm{d}q}{\mathrm{d}t} = \vec{J} \cdot \vec{r} = \sigma \vec{E} \cdot \vec{r} \tag{2.5}$$

and

$$\frac{\mathrm{d}\zeta_i}{\mathrm{d}t} = \frac{\sigma}{\varepsilon_w \kappa} \vec{E} \cdot \vec{r} \tag{2.6}$$

where $\kappa^{-1} = \lambda_D$ is the Debye EDL thickness, and ζ_i and ε_w are the induced zeta potential and the dielectric permittivity of the solution, respectively.

Because of the presence of the screening charge cloud, the electric field lines are expelled and the ionic flux into the charge could is reduced. When the conductor is fully polarized and reaches a steady state, the conductor behaviors like an insulator because an induced dipolar double layer is formed, as shown in Figure 2.3b. Then, a steady-state electric field is established. This steady-state electrostatic configuration is equivalent to the no-flux electrostatic boundary condition assumed in standard electrokinetic analysis and the external applied electric potential ϕ_e at this steady state is governed by Laplace's equation

$$\nabla^2 \phi_e = 0 \tag{2.7}$$

The charging time to set up this steady field is quite small (on the order of 10^{-4} s) for a highly polarizable conductor (Squires and Bazant 2004) and is negligible. The resultant induced steady-state zeta potential ζ_i is proportional to the local electric strength E and hence varies with position on the conducting surface. For relatively simple and regular geometries, there exist exact steady-state solutions to Eq. (2.6). For instance, Squires and Banzant have derived the exact analytical formulation of the induced zeta potential on the surface of a 2D circular cylinder (Squires and Bazant 2004), given by

$$\zeta_i(\theta) = 2E_0 a \cos\theta \tag{2.8}$$

where θ is angular coordinate and a is the radius of the cylinder. However, for a surface with a complex or irregular shape, there is no simple analytical solution for the distribution of the induced zeta potential. Thus, a numerical scheme is needed to relate the induced zeta potential with the external applied field.

To numerically determine the steady-state induced zeta potential distribution ζ_i, we considered the following:

1. The induced screening cloud generates a local electric field and acts as an insulating shell over the surface so that the field lines of the externally applied electric field cannot intersect the surface. Thus, the local strength of the induced field E_i on the conducting surface, i.e. the local potential gradient along the surface, should be in the same magnitude as that of the externally applied electrical field E_e, i.e.,

$$|E_i| = |E_e| \tag{2.9}$$

2. Because the image charges in the conductor have an opposite sign to that of the ions attracted at the conducting surface from the liquid, the induced electric field on the conductor-liquid interface should be in the opposite direction to that of the

external field, that is

$$E_i = -E_e \tag{2.10}$$

or

$$\nabla \zeta_i = -\nabla \phi_e \tag{2.11}$$

where ϕ_e is the local externally-applied electric potential given by Eq. (2.7).

3. Assuming that the conducting hurdles are initially uncharged, the integration of the induced charge over the whole conducting surface should be zero because of the initial electric neutrality of the surface. Thus, the linear relationship between surface charge and zeta potential Eq. (2.1) gives zero integration of the induced zeta potential around the conducting surface, that is

$$\oint_{\mathrm{S}} \zeta_i \mathrm{ds} = 0 \tag{2.12}$$

where S is the conducting surface in the applied electric field. If the conducting surface is initially charged, the final steady-state zeta potential distribution is simply a superposition of the initial equilibrium zeta potential $\zeta_0 = \zeta(t=0)$ and the induced zeta potential ζ_i, which follows from the linearity of Eq. (2.6) (Squires and Bazant 2004). In this study, only the case of initially uncharged conducting hurdles is considered.

If we limit our attention to the case of thin double layer and small Dukhin number ($Du \ll 1$), i.e., surface conduction is negligible compared to the bulk conduction, and no electrochemical reactions are present at the conductor-liquid interface, the above conditions are valid (Squires and Bazant 2004). A correction method is suggested herein to numerically calculate the induced zeta potential distribution on the conducting surfaces from the known external electric potential ϕ_e. Directly integrating Eq. (2.11), the local induced zeta potential is obtained as

$$\zeta_i = -\phi_e + \phi_c \tag{2.13}$$

where ϕ_c is a constant correction potential. By inserting Eq. (2.13) into Eq. (2.12), we can evaluate the correction potential as

$$\phi_c = \frac{\int_S \phi_e \mathrm{dA}}{\mathrm{A}} \tag{2.14}$$

where A is the area of the entire surface of the conducting object. By using the numerical formulation Eq. (2.13), all the three conditions are met. Eq. (2.13) and Eq. (2.14) give a quick and simple numerical method to calculate the final steady state induced zeta potential distribution on the conducting surfaces with arbitrary geometries. The numerical scheme is validated by the comparison with the analytical formulation Eq. (2.8) for a 2-D cylinder, as shown in Figure 2.4. The results show a good matching between the numerical and the analytical formulations.

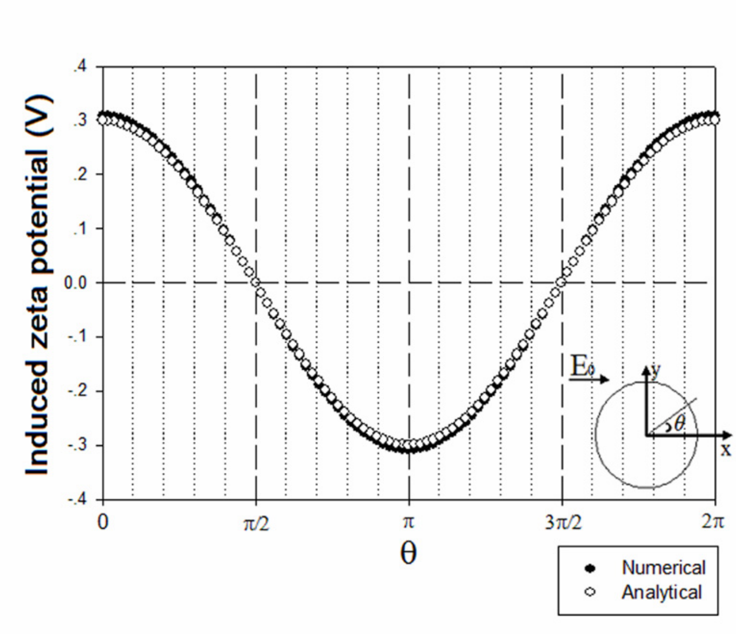

Figure 2.4 Induced zeta potential on a conducting circular cylinder surface (*a* =15 μm, E_0=10v/cm).

Once the dipolar induced double layer is formed, the externally applied field exerts a body force on the ions in the screening cloud in the liquid, driving the ions and the liquid into motion (Figure 2.5). The resultant electrokinetic flow appears to slip just outside the screening layer of thickness λ_D and the slip flow velocity varies proportionally to the local tangential electric field $E_{||}$ and given by the Helmholtz-Smoluchowski formula Eq. (2.3). It is important to recognize that the velocity of ICEKF is nonlinearly dependent on the applied electric field, considering the dependence of the local induced zeta potential ζ_i on the local electric strength *E*. As shown in Figure 2.5, the flow is non-uniform, resulting in vortex near the solid-liquid interface.

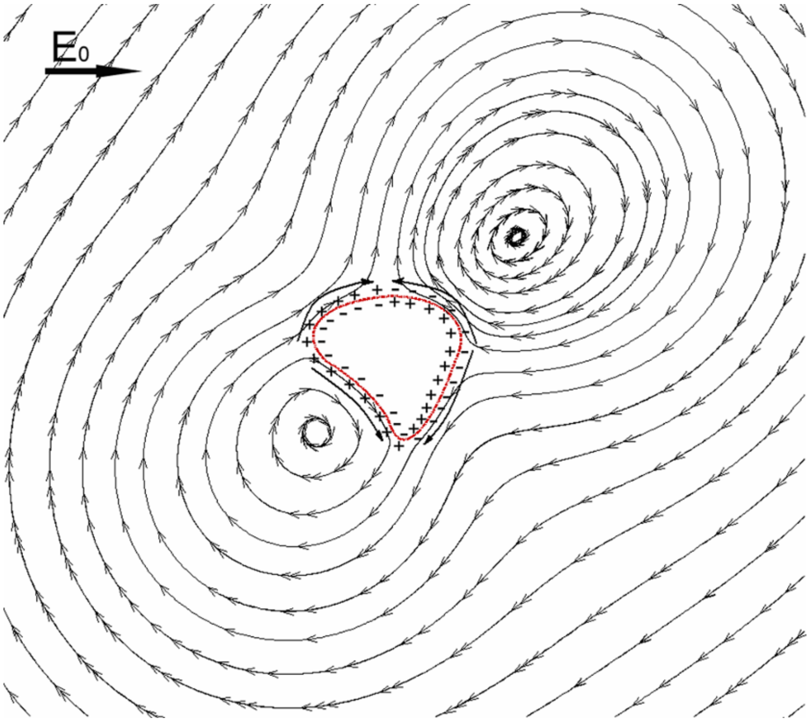

Figure 2.5 Induced-charge elelctrokinetic flow field around a conducting object.

2.3 Summary

A fundamental theory of induced charge electrokinetics is set up in this chapter. It's found that a nonlinear induced surface charge distribution is immediately caused when a conducting object is immersed in an external applied electric field. The induced charge on the conducting surfaces results in a non-linear zeta potential distribution and an induced electric double layer when the surfaces contact with an aqueous buffer solution. The non-constant zeta potential gives a varying slipping velocity along the conducting surface, which produces micro vortexes in the liquid. A correction method is suggested to numerically estimate the induced zeta potential on the conducting surfaces. With the perfect matching with the analytical solutions, the numerical scheme suggested in this chapter provides certain simplification to study the ICEK behaviors of the objects with arbitrary geometries.

CHAPTER III

MICROMIXING AND FLOW REGULATING USING INDUCED-CHARGE ELECTROKINETIC FLOWS

This chapter describes the induced-charge electrokinetic flow (ICEKF) in a rectangular microchannel with embedded conducting hurdles. Two-dimensional pressure-linked Navier-Stokes equation is used to model the flow field in the channel. The numerical results show flow circulations generated from the induced non-uniform zeta potential distribution along the conducting hurdle surfaces. It is demonstrated that the local flow circulations provide effective means to enhance the flow mixing between different solutions. The mixing enhancement effect is experimentally validated using PDMS based microchannels with embedded platinum hurdles. The dependence of the degree of mixing enhancement on the hurdle geometries and hurdle numbers is also predicted. It's also found that, by adjusting the electric field applied through the microchannel with a non-symmetric conducting triangle hurdle pair, an electrokinetic flow regulating effect can be obtained and this effect depends on the dimensions of the conducting converging-diverging section. The mixing and flow regulating using ICEKF described in this chapter can be used in various microfluidics and lab-on-a-chip applications.

3.1 Introduction

During the past decade, significant advance has been achieved in the area of the micro total analysis systems (μTAS) or lab-on-a-chip (LOC) devices (Whitesides 2006; DeMello 2006; Chin et al. 2007; Dittrich and Manz 2006; El-Ali et al. 2006), showing great promise for performing a variety of chemical and biochemical analyses. An integrated lab-on-a-chip device can incorporate many of the necessary components and functions of a typical room-sized laboratory into a small chip that performs a specific biological or chemical analysis, including sample treatment, transport, reaction, and detection. Lab-on-a-chip devices are not simply the smaller versions of the conventional instruments; miniaturization raises many new challenges, and LOC devices often involve new physical phenomena and new processes that are dominated by the forces important at microscale. Controlled transport of liquids and chemical and biological samples is one of crucial issues in these LOC devices.

Electrokinetic methods, including electroosmosis, electrophoresis, and dielectrophoresis, are playing important roles in microfluidic devices. These phenomena have been extensively used for pumping, mixing, gradient generation, separation, and sorting on lab-on-a-chip devices. Electroosmosis is widely used as a pumping method due to its significant advantages over the conventional pressure-driven flow, such as plug-like velocity profile, ease to control and switch flow, and no mechanical moving parts. Generally, electrokinetically-driven flows in microchannels are laminar because of the slow velocity and small characteristic length scale and thus small Reynolds number ($\mathrm{Re} << 1$). Consequently, mixing in such a laminar flow of parallel streams occurs only by diffusion, which is problematic for situations requiring rapid mixing of different solutions in microchannels. Overcoming the challenges associated with microscale mixing has been the focus of numerous endeavors intent on introducing supplementary mixing schemes based on a variety of technologies such as piezoelectrics (Yang et al. 2000; Woias et al. 2000), pneumatics (Hosokawa et al. 2000) and acoustic radiation (Yasuda 2000) as well as multiple voltage arrangements (Jonson et al. 2001). Some electrokinetic based devices have been developed to perform mixing enhancement, such as T-shaped microchannel mixers, which employ electroosmotic flow to pump liquids from two horizontal channels to the T-intersection and mix liquids in the vertical channel while the liquid flows to downstream. T-shaped mixers have been applied in various lab-on-a-chip devices, for example, to dilute sample in a buffer solution (Harrison et al. 1993) and to generate concentration gradients (Dertinger et al. 2001). Furthermore, Jacobson et al. (Jacobson et al. 1999) proposed an electroosmotic-based microfluidic device designed with series T-intersections capable of multiple samples parallel mixing. Electrokinetic based focusing (Jacobson & Ramsey 1997) is another way for parallel lamination mixing, which splits inlet mixing stream into two or more sub-streams, and then joins them horizontally as individual laminae in a single stream so that the width of the sample flow can be restricted and consequently the diffusion length is reduced. The use of electroosmotic flows has also expanded the potential of surface chemistry as a means of mixing enhancement. Surface charge heterogeneities have been suggested as a mechanism for enhanced mixing in electroosmotic flows (Erickson & Li 2002; Stroock et al. 2000; Barker et al. 2000; Hau et al. 2003). The method was further extended with a non-uniform distribution of zeta potential along the channel wall to generate micro flow circulation to enhance the mixing between two solutions (Biddiss et al. 2004). To avoid the complex channel surface heterogeneity, a technique called electrokinetic instability mixing (Oddy et al. 2001) utilizes time-dependent electric fields to generate more chaotic flow patterns, which can improve the mixing performance at a low intensity of DC electric field (Lin et al. 2004) or a high intensity AC electric field (Shin et al. 2005). The major disadvantages of electrokinetic instability mixing is that the electrical conductivity gradients must exist in the bulk flow (i.e. two flow streams with different conductivities are required) and a high electric field strength is required. The phenomena called electroosmosis of the second kind (Dukhin 1991) provides another way for active mixing enhancement, in which nonlinear electroosmotic vortices are generated around a conducting ion-exchange granular or near a dielectric sharp corner. The technique was successfully applied to improve micro-mixing in a closed flow system (Wang et al. 2004). All these electrokinetic based mixing methods mentioned herein highly rely on the complex channel design, surface modification and voltage control.

To regulate the flow in the microchannels, typically membrane pumps and valves are used with different actuation methods including piezoelectric, electrostatic, and thermopneumatic actuation in silicon, glass, some plastic devices (Laser and Santiago

2004), and pneumatic actuation in PDMS devices (Unger et al. 2000; Ismagilov et al. 2001; Jeon et al. 2002). All these mechanisms require complicated fabrication techniques to introduce moving parts into the microfluidic systems. Electroosmotic flow (EOF) involves simple channel design and fabrication, and does not require mechanical valves. However, EOF-based flow regulating can be more complex because it requires multiple power supplies and timed switching of voltages among these power supplies (Harrison et al. 1992; Seiler et al. 1993; Jacobson et al. 1994; Jacobson et al. 1999).

As indicated in Chapter II, induced-charge electrokinetic flow (ICEKF) provides a mechanism of micro vortex generation near a highly polarizable conducting object in an external electric field, which is caused by the induced non-uniform charges at the conductor-liquid interface and the resulting non-uniform electroosmotic flow. Thus, it can be predicted that, by introducing conducting surfaces in a microchannel, irregular flow field with micro vortex can be obtained, which can be used to enhance the species mixing. Additionally, the flow circulations in the microchannel may provide a potential way to gate the flow in the microchannel. The applications of induced-charge electroosmosis for mixing enhancement with microelectrode arrays and streaming flow pumping with asymmetric conducting bodies were theoretically predicted (Squires and Bazant 2004; Squires and Bazant 2006). So far, the investigated applications of ICEO require complicated fabrications of complex microelectrode arrays and no flow regulating effect was studied.

In this Chapter, I present a study of the mixing and flow regulating effects of the induced-charge electrokinetic flow in a microchannel with embedded conducting hurdles on the channel sidewalls. A correction method is proposed to numerically estimate the induced zeta potential on the conducting surface. A two-dimensional numerical model is used to obtain the electric field, the flow field and the concentration field. The induced-charge electrokinetic flow behaviors in the channel are investigated.

3.2 Theory and numerical scheme

This study initially considers the electroosmotically driven flow through a rectangular microchannel with embedded conducting triangular hurdles, which have a height of 125 μm and a width of 250 μm and form a converging-diverging section, as shown in Figure 3.1. The channel has a depth of 36 μm and a width of 300 μm. The two ends of the microchannel connect two reservoirs containing an aqueous solution. Electrodes are inserted in these reservoirs. As mentioned in Chapter II, when an electrical field is applied through the channel via the two electrodes, electroosmotic flow will be generated in the channel. Micro vortices will be produced near the conducting converging-diverging section of the channel because of the induced non-uniform charges on the conducting surfaces. Strict saying, the problem proposed here is three-dimensional with the effects of top and bottom walls. However, by assuming the homogeneous non-conducting channel walls with uniform zeta potential distribution and thus the uniform slipping EOF velocity on non-conducting surfaces, the top and bottom walls will not affect the EOF in main channel branches. In the region with conducting hurdles, the induced zeta potential on the conducting surface, which is in the magnitude of volts (see Figure 2.4), is much larger than that on the non-conducting bottom and top walls, which is normally in the magnitude of mili-volts. Thus, to qualitatively study the dominant induced-charge effects in x-y plane, the problem can be simplified as a 2-D model as shown in Figure 3.1.

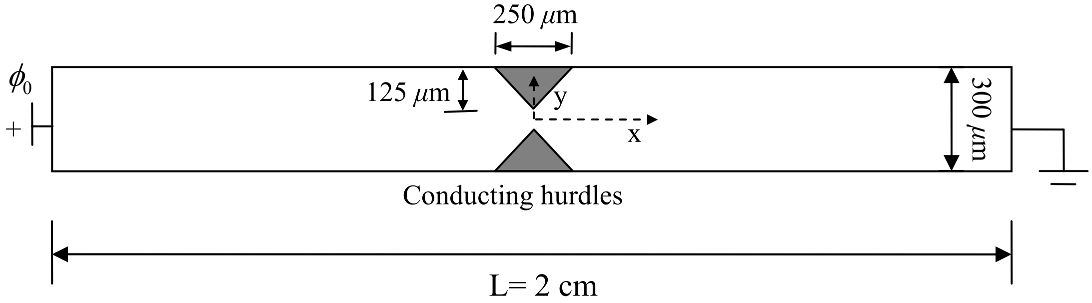

Figure 3.1 Schematic diagram of the microchannel with a pair of conducting triangle hurdles.

Once the electric field is applied, the conducting hurdles are polarized immediately. The final steady-state electric field in the microchannel is shown in Figure 3.2. The applied electrical potential in the liquid ϕ_e is governed by the Laplace's equation (Keh and Anderson 1985)

$$\nabla^2\phi_e = 0 \tag{3.1}$$

with the boundary conditions

$$n\cdot\nabla\phi = 0 \text{ at channel wall} \tag{3.2}$$

$$\phi = \phi_0 \text{ at inlet} \tag{3.3}$$

$$\phi = 0 \text{ at outlet.} \tag{3.4}$$

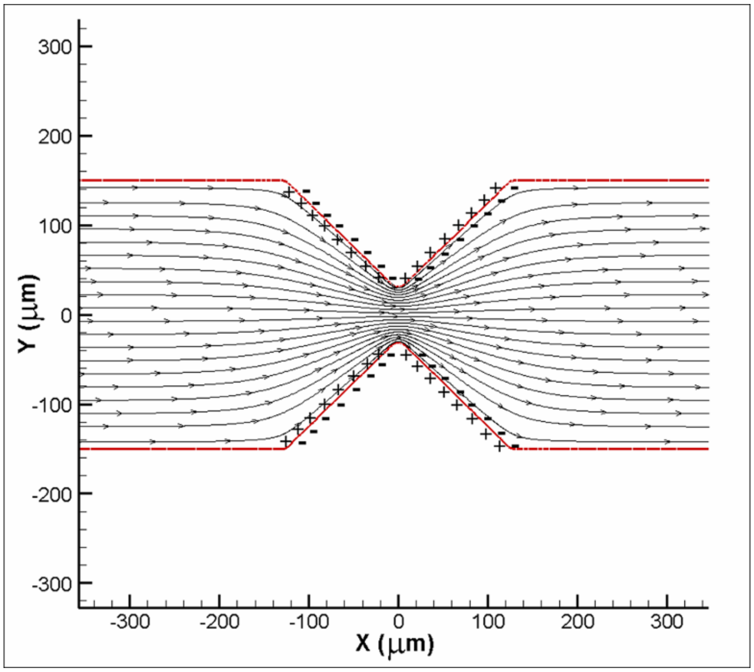

Figure 3.2 The steady-state electric field in the converging-diverging section and the induced charge on the conducting hurdles.

The induced charge clouds on the conducting hurdle surfaces give rise to a non-constant zeta potential distribution, as indicated by Eq. (2.13) and Eq. (2.14). Figure 3.3 shows a typical induced zeta potential distribution along the conducting triangle hurdle surface with an external field of 275 V/cm. Obviously, the induced zeta potential is non-uniformly distributed.

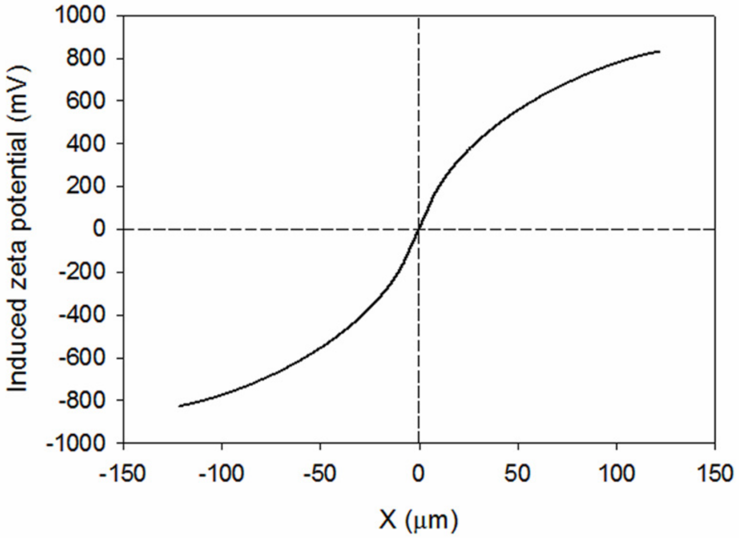

Figure 3.3 Induced zeta potential distribution along the triangle conducting hurdle surface.

Once the electric field is set up through the liquid in the microchannel, electrical force is exerted on the net charges within the electric double layer, no matter the double layer is induced on the conducting hurdle surfaces by the applied field or formed by the electrostatic charges on the non-conducting channel wall. The motion of the net charges will draw the adjacent liquids to move, generating the electroosmotic flow. Because the local net charges on the conducting hurdle surfaces are non-uniformly distributed and have opposite signs between the upstream side and the downstream side (see Figure 3.3), the resultant liquid motion will also be non-uniform and in opposite directions, causing the vortexes near the conducting hurdles.

The equations governing incompressible liquid flow are the Navier-Stokes equation and the continuity equation.

$$\rho\left[\frac{\partial\vec{u}}{\partial t}+\vec{u}\cdot\nabla\vec{u}\right]=-\nabla P+\mu\nabla^2\vec{u}+\vec{E}\rho_e \tag{3.5}$$

$$\nabla\cdot\vec{u}=0 \tag{3.6}$$

where $\vec{u}$ is the velocity vector, ∇P is the pressure gradient, μ is the viscosity, ρ is the density of the fluid, ρ_e is the local net charge density and $\vec{E}=-\nabla\phi_e$ is the local applied electrical filed strength. Since the local net charge density is not zero only in the electrical double-layer (EDL), the driving force for electroosmotic flow, $\vec{E}\rho_e$, exists only in EDL. The electroosmotic flow velocity changes sharply in a thin layer of the liquid near the solid wall. The thickness of EDL is given by Debye length (Hunter 1981)

$$\lambda_D=\sqrt{\frac{\varepsilon_w k_B T}{2n_0(ze)^2}} \tag{3.7}$$

where k_B is the Boltzmann constant, T is the temperature and n_0 is the bulk ionic concentration. For most on-chip microfluidic applications, buffer solutions have an ionic concentration of the order of mM, which results in a very thin EDL negligible in comparison with the microchannel dimensions. Therefore, for the purpose of modeling the bulk liquid flow outside the EDL, the driving force term $\vec{E}\rho_e$ in Eq. (3.5) will be dropped off and the electroosmotic effect is considered by applying Helmholtz-Smoluchowski slip velocity as a boundary condition (Hunter 1981):

$$\vec{u}\big|_{\text{wall}}=-\frac{\varepsilon\varepsilon_0\zeta}{\mu}\vec{E} \tag{3.8}$$

where ζ is the zeta potential at the channel wall and $\vec{E}=-\nabla\phi_e$ is local electric field.

Here, careful attention should be paid to the zeta potential, which is constant only on the non-conducting channel wall. On the conducting hurdle surfaces, ζ is replaced by the local induced zeta potential ζ_i as defined in Eq. (2.13). By considering the steady state flow, the transient term in Eq. (3.5) can be dropped off and the Eq. (3.5) is reduced to a 2-D form as

$$\rho\left(u_x \frac{\partial u_x}{\partial x} + u_y \frac{\partial u_x}{\partial y} \right) = -\frac{\partial P}{\partial x} + \mu\left(\frac{\partial u_x}{\partial x^2} + \frac{\partial u_x}{\partial y^2} \right) \tag{3.9a}$$

$$\rho\left(u_x \frac{\partial u_y}{\partial x} + u_y \frac{\partial u_y}{\partial y} \right) = -\frac{\partial P}{\partial y} + \mu\left(\frac{\partial u_y}{\partial x^2} + \frac{\partial u_y}{\partial y^2} \right) \tag{3.9b}$$

The corresponding boundary conditions for the velocity are:

$$u_x = \frac{\varepsilon_w \zeta}{\mu} E_x,\ u_y = \frac{\varepsilon_w \zeta}{\mu} E_y \text{ at non-conducting channel wall} \tag{3.10a}$$

$$u_x = \frac{\varepsilon_w \zeta_i}{\mu} E_x,\ u_y = \frac{\varepsilon_w \zeta_i}{\mu} E_y \text{ at conducting hurdle surfaces} \tag{3.10b}$$

$$\frac{\partial u_x}{\partial x} = 0,\ \frac{\partial u_y}{\partial x} = 0 \text{ at inlet and outlet} \tag{3.10c}$$

An implication of Eq.(3.10c) in the above boundary conditions is that the microchannel is sufficiently long, the end boundaries have no influences on the flow field near the hurdles (the converging-diverging section).

In this study, no pressure gradient is considered and the fluid flow is totally electrokinetically driven. The pressures at the two ends of the microchannel are specified as zero:

$$P = 0 \text{ at inlet and outlet} \tag{3.11}$$

Also, the pressure gradient is set to be zero at the channel wall, considering no flux across the wall:

$$n \cdot \nabla P = 0 \text{ at channel wall} \tag{3.12}$$

In the development of the numerical simulation, the following non-dimensionalization was used

$$u'_x = \frac{u_x}{U},\ u'_y = \frac{u_y}{U},\ x' = \frac{x}{H},\ y' = \frac{y}{H},\ P' = \frac{P - P_a}{\rho U^2} \tag{3.13}$$

Where U is the reference velocity, H is the width of the channel and P_a is the pressure of atmosphere.

The above 2-D pressure linked problem, i.e. Eqs. (3.1), (3.6), (3.9a) and (3.9b), was solved by the non-linear finite element solver of COMSOL MULTIPHYSICS® 3.2. The built-in steady incompressible Navier-Stokes model was utilized as the basic model to deal with the pressure linked equations. A user-defined integral coupling variable gave the connection between the induced zeta potential (Eq. (21.3) and Eq. (2.14)) and the corresponding boundary conditions of EOF (Eq. (3.10b)). A non-uniform spaced grid was employed for more accurate solutions. The total number of elements used in the computation was 27268. The physical properties for the fluid and the specifications for the microchannel used in the simulations are shown in Table 3.1.

Table 3.1 Constants used in the numerical simulations

Dielectric constant ε	80
Permittivity of vacuum ε_0 (C/V·m)	8.854×10^{-12}
Viscosity μ (kg/m·s)	0.9×10^{-3}
Density ρ (kg/m^3)	998
Microchannel length L (cm)	2
Microchannel depth d (μm)	40
Microchannel width H (μm)	300
Zeta potential on non-conducting channel wall (mV)	−50

The above equations and the matching boundary conditions for flow field were solved numerically. An electric strength of 50 V/cm was applied along the microchannel. For the purpose of comparison, both the cases of conducing and non-conducting hurdles were simulated. As mentioned earlier, when the conducting hurdles are immersed in the applied electric field, a non-uniform zeta potential distribution will be induced on the conducting surfaces, causing a varying driving force of the electroosmotic flow. Consequently, the slipping velocity on the conducting surfaces changes with position, resulting in a non-uniform flow field. Figure 3.4 shows the flow fields of the two cases. The most notable feature in the flow field is that the flow is significantly changed with the presence of the conducting hurdles. Due to the oppositely charged surfaces (Figure 3.2), flow circulations are generated near the converging-diverging zone in the channel. The opposite signs of the induced zeta potential indicate opposite EOF driving forces, which are responsible for the flow circulations. In the region with positive induced zeta potential, a negative net charge exists in the EDL, generating a negative flow towards the inlet of the channel. In the region with a negative induced zeta potential, a positive net charge exits in the EDL, generating a positive flow towards the outlet of the channel. Thus, flow circulation is produced to ensure the fluid continuity. Clearly, such flow behavior can be used to enhance the flow mixing. Another potential application is the electrokinetic flow regulating effect, which will be discussed in the later sections.

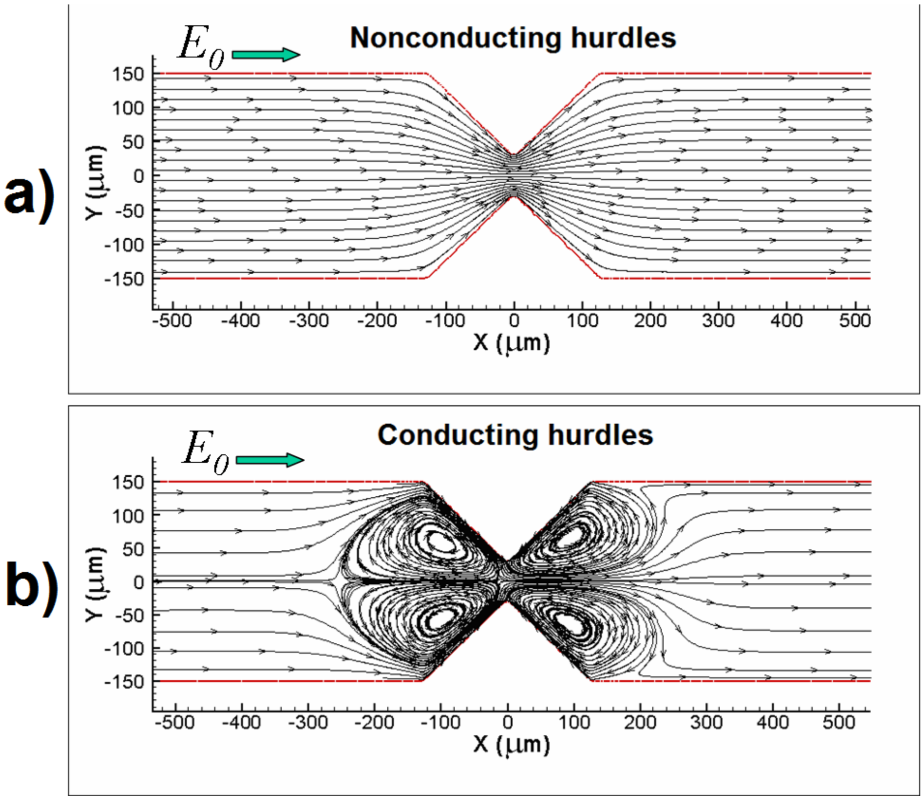

Figure 3.4 Flow fields with (a) a pair of non-conducting hurdles and (b) a pair of conducting hurdles. The lines are stream lines. E_0 = 50 V/cm.

3.3 Species micro mixing using ICEKF

3.3.1 Numerical simulation of ICEK micro mixing

To investigate the feasibility of using the above induced-charge electrokinetic flow to enhance species mixing, we examined two parallel streams entering the channel from the inlet, with a non-dimensional/normalized concentration of 1 and 0, respectively. The two parallel streams enter the inlet and initially separated by the channel center line. The concentration field of electrolytes or other chemical components in such an electroosmotic flow can be described by

$$\frac{\partial C}{\partial t} + (\vec{u} + \vec{u}_{ep}) \cdot \vec{\nabla} C = D \nabla^2 C \tag{3.14}$$

where C is the concentration of the species, D is the diffusion coefficient of the species and $\vec{u}_{ep}$ is the electrophoretic velocity of the species. In most microfluidic applications, electroosmotic velocity is on the order of 1 mm/s and the diffusion coefficient of most simple electrolytes is approximately $1.0\times10^{-10}\text{m}^2/\text{s}$. It can be found that the order of magnitude of the convection term in Eq. (3.14) is approximately 1000 times of that of the diffusion term. Therefore, the flow field should give a good indication of the concentration field, consequently, a basic understanding of the mixing effectiveness. Generally, the stronger local flow circulation is, the better the mixing is. Thus, it can be expected that the flow circulation resulted from the induced non-uniform zeta potential on the conducting hurdle surfaces can greatly enhance the species mixing.

The coupled concentration field and the flow field are solved using COMSOL MULTIPHYSICS® 3.2. The Petrov-Galerkin type artificial diffusion was selected to increase the stability of convection-type equation. The results are shown in Figure 3.5.

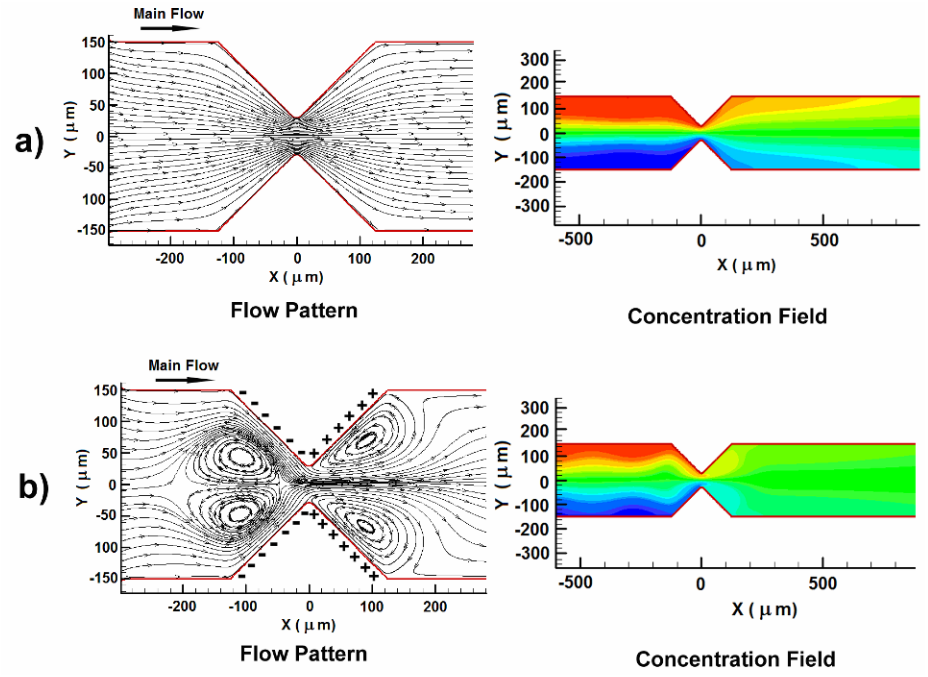

Figure 3.5 Flow and concentration fields with (a) a pair of non-conducting hurdles and (b) a pair of conducting hurdles. (E_0=50 V/cm, D=1.0×10^{-10} m^2/s)

As indicated in an earlier study (Lee et al. 2005), a simple non-conducting converging–diverging microchannel can generate linear and spatially stable concentration gradients in electroosmotic flows (see Figure 3.5a). However, to mix the species well in the downstream, a long mixing length is needed if no flow circulation presents. Thus, the vortex generation as shown in Figure 3.5b will enhance the flow mixing. As indicated in Figure 3.5b, the conducting hurdles produce significantly better mixing and a more uniform concentration profile right after the converging-diverging zone. The mixing length thus can be reduced considerably.

3.3.2 Experimental validation

The microchannels in this study were fabricated using a rapid prototyping/soft lithography technique (Duffy et al. 1998). Photomasks were designed in AutoCAD and printed on a 20000 DPI image setter (CAD/Art Services Inc., Bandon, OR). Glass slides were soaked overnight in acetone, dried on a hot plate at 150°C, exposed to oxygen plasma (Harrick Plasma Cleaner model PDC-32G) for 8 minutes to prepare the surface for photoresist spin coating. A 1.5 mL sample of SU-8 25 negative photoresist (MicroChem, Newton, MA) was distributed onto each glass slide and degassed in a high vacuum for 1-2 hours. The photoresist was then spin coated at 300 rpm for 6s and at 1450 rpm for 25s to form a smooth photoresist film of 36 μm on the glass surface (Special Coating System G3P-8). The coated slides were baked at 65^{o} C for 5 min and at 95^{o} C for 15 min to pre-harden. The pre-designed photomasks were then positioned on the photoresist films and the films were exposed to UV light for 7s. The postexposure baking at 65^{o} C for 1 min and 95^{o} C for 4 min was then conducted. The positive masters were manufactured after developing the exposed photoresist films in 1-Methoxy-2-Propanol Acetate (MicroChem, Newton, MA). The masters were then baked at 250 ^{o}C for 25 minutes to be hardened. The microchannels were formed from polydimethylsiloxane (PDMS) using a Sylgard 184 silicone elastomer kit (Dow Corning, Midland, MI) with an elastomer-to-curing agent ratio of 20:1. The PDMS was poured over the masters and degassed at a high vacuum for 1 hour, followed by a curing process at 70^{o} C for 2 hours. The cured PDMS slabs with the microchannel patterns (see Figure 3.6) were then cut and peeled off from the masters and ready for use.

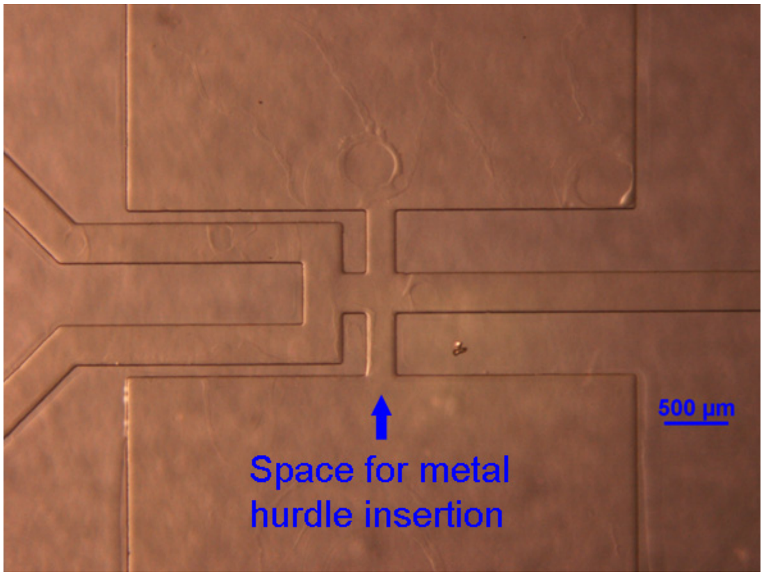

Figure 3.6 The microchannel fabricated using PDMS based soft lithography technique

The hurdles (GeSim Ltd, Dresden, Germany) used in this study are made of silicon and all have a triangular-shaped head of 200 μm in width, 125 μm in height and 36 μm in thickness. The non-conducting hurdles are silicon coated with 1.5 μm SiO_2 insulation layer. The conducting hurdles have a thin-platinum-film (150 nm) covered triangle head. The conducting hurdles were inserted into the microchannel through the pre-designed insertion space (Figure 3.6) in the channel (Figure 3.7). The entire PDMS slab was then treated by oxygen plasma for 1 min and bonded with another flat PDMS slab forming the bottom wall to finalize the chip structure (see Figure 3.7). The microchannel has two branches at the left, connected with the anode of a DC power supply, for parallel delivery of two different chemical species (S1 with a normalized concentration of 1 and S2 with a normalized concentration of 0). The right single branch forms a mixing channel and is connected with the cathode of the power source.

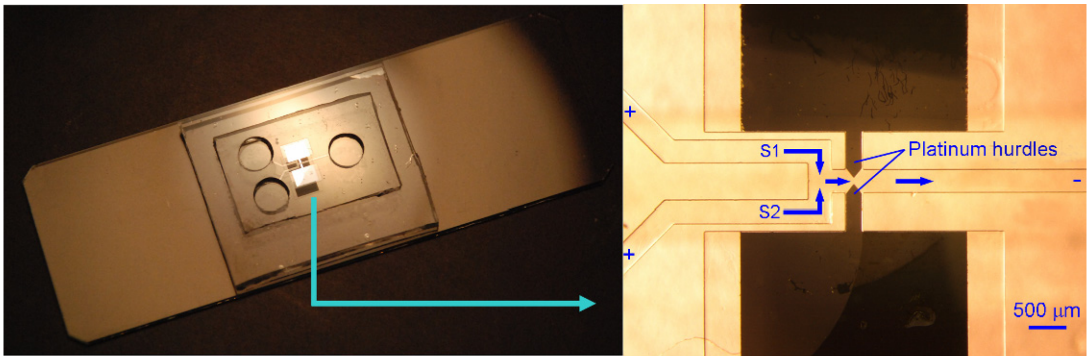

Figure 3.7 The microchannel with embedded triangular platinum hurdles.

All the solutions used in the experiment were prepared using deionized filtered water. Sodium bicarbonate, 1 M, and sodium carbonate, 1 M, were combined in equal ratio to form a sodium carbonate/bicarbonate buffer with an ionic strength, I = 0.05 and pH=9.0. The buffer was diluted with water to 2.5 mM. Fluorescein (Sigma-Aldrich, St. Louis, MO) was dissolved with 2.5 mM buffer to a concentration of 100 μM for fluorescent imaging.

To perform the mixing experiments, 100 μM fluorescein solution (S1) and 2.5 mM sodium carbonate/bicarbonate buffer (S2) were introduced through the inlet branches.

The steady-state transport of fluorescent dye was observed using a Nikon ECLIPSE TE2000-U microscope with a 4× objective and captured using a QIMAGING Micropublisher CCD camera. Digital images were obtained by QCapture 1394 software and imported to NIS-Elements 2.10 software for digital processing. Concentration profiles in the mixing channel branch were developed directly from the values of pixel intensities and linearly scaled to range between 0 and 1. Results for the channels with embedded conducting platinum hurdles were compared to those with non-conducting hurdles.

To study the effectiveness of the mechanism of ICEK micro mixing enhancement, the earlier mentioned numerical scheme was used to simulate the experimental conditions. The fluorescein has a diffusion coefficient $D = 4.37 \times 10^{-10}$ m^2/s. The fluid properties are $\rho = 998$ kg/m3 and $\mu = 0.001$ kg/(m·s). The electroosmotic mobility is 5.9×10^{-4} cm^2/V·s for the non-conducting channel wall. The electrophoretic mobility of the fluorescein is 3.3×10^{-8} m^2/ V·s, thus negligible in comparison with the EOF mobility. The zeta potential on the conducting hurdle surfaces is given by Eq. (2.13) and Eq. (2.14).

The mixing efficiency, ε, is used to quantify the mixing enhancement by ICEKF,

$$\varepsilon = \left(1 - \frac{\int_0^W \left| C - C_\infty \right| \mathrm{dx}}{\int_0^W \left| C_0 - C_\infty \right| \mathrm{dx}} \right) \times 100\% \tag{3.15}$$

where C_∞ =0.5 corresponds with perfect mixing on a normalized scale, C_0 is the concentration distribution over the channel width, W, at the channel inlet and C is the concentration distribution at some distance downstream. A fully mixed state therefore would have a 100% mixing efficiency while the unmixed state would have a 0% mixing efficiency.

The experiments were conducted at an applied electric field of 50V/cm. Two different hurdle position cases were studied, the symmetric case with two hurdles directly opposite to each other and the non-symmetric case with an offsetting distance of 500 μm between the hurdles. Figure 3.8 and Figure 3.9 illustrate the concentration fields under the symmetric and non-symmetric cases respectively. As can be seen in the figures, experimental results compared well with the numerical simulations. As predicted earlier, by introducing conducting hurdles into the microchannels, the vortices generated near the hurdles facilitate the flow mixing. Therefore, the concentration fields downstream (after the hurdles) become more uniform than those of the channels with no conducting hurdles, thus the flow mixing is effectively enhanced. It is also seen that the symmetric conducting hurdle arrangement leads to a more uniform concentration field than that of the non-symmetric arrangement, thus providing better mixing effect.

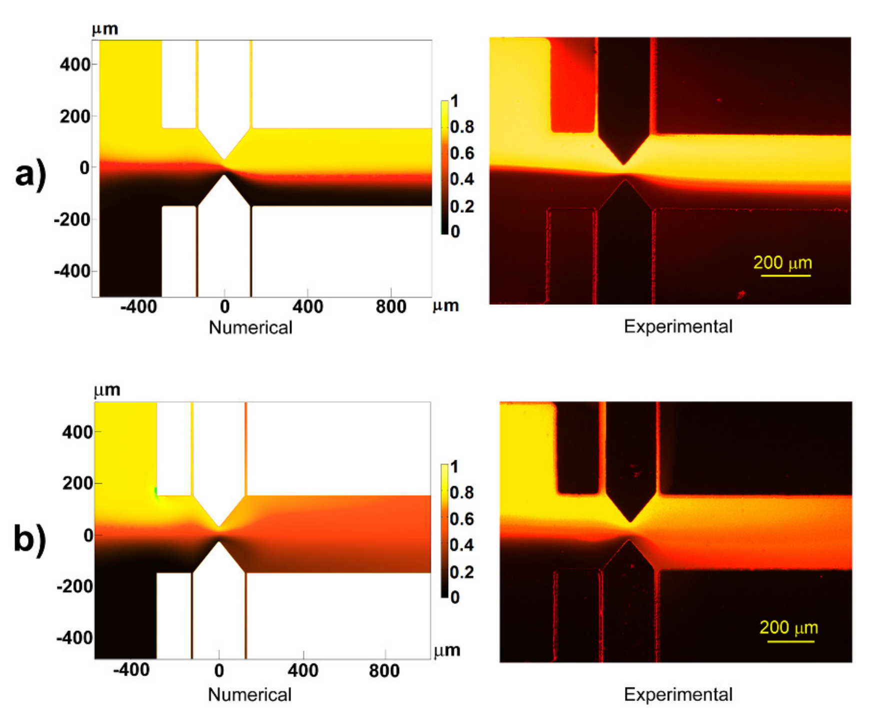

Figure 3.8 Concentration fields with symmetric hurdle arrangement for (a) non-conducting hurdles and (b) conducting hurdles. (Applied electric field E_0 = 50V/cm).

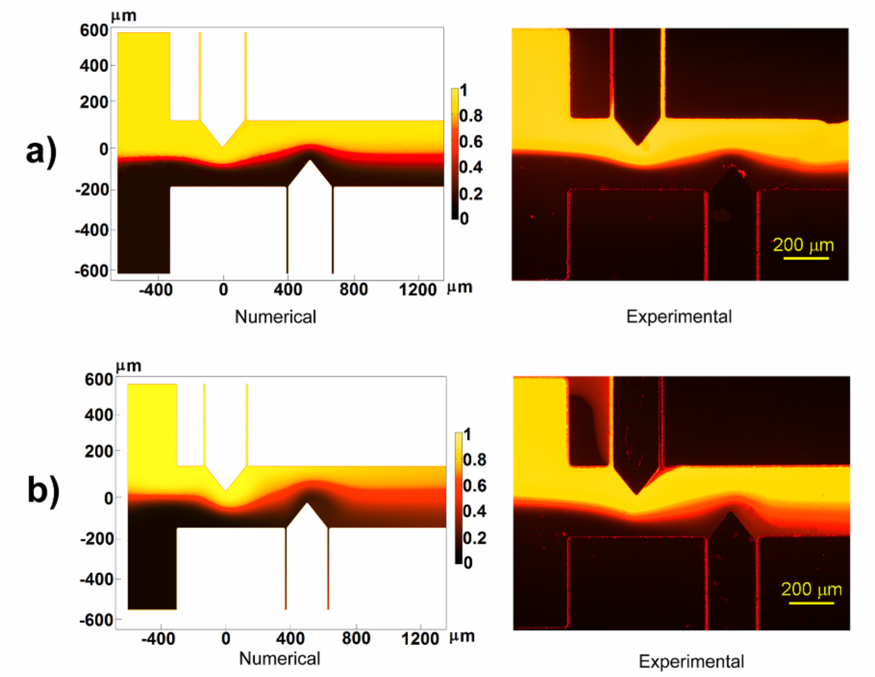

Figure 3.9 Concentration fields with non-symmetric hurdle arrangement for (a) non-conducting hurdles and (b) conducting hurdles. (Applied electric field E_0 = 50V/cm).

Comparisons of the concentration profiles between channels with conducting and non-conducting hurdles under both symmetric and non-symmetric arrangements are given in Figure 3.10. The profiles were plotted along the channel width and measurements were made at two downstream distances of 500 μm and 2000 μm, respectively. The distances are measured from the last hurdle edge. The results indicate a substantial increase in species mixing with consistent agreement between the numerical simulations and the experiments. Again, it has shown that the symmetric conducting hurdle arrangement gives better mixing enhancement with the mixing efficiencies of 76.24% at 500 μm downstream and 92.46% at 2000 μm downstream, respectively, while the non-symmetric arrangement gives an average mixing efficiency of 65.53%. The non-conducting hurdles produce the lowest average mixing efficiency of 45.37%.

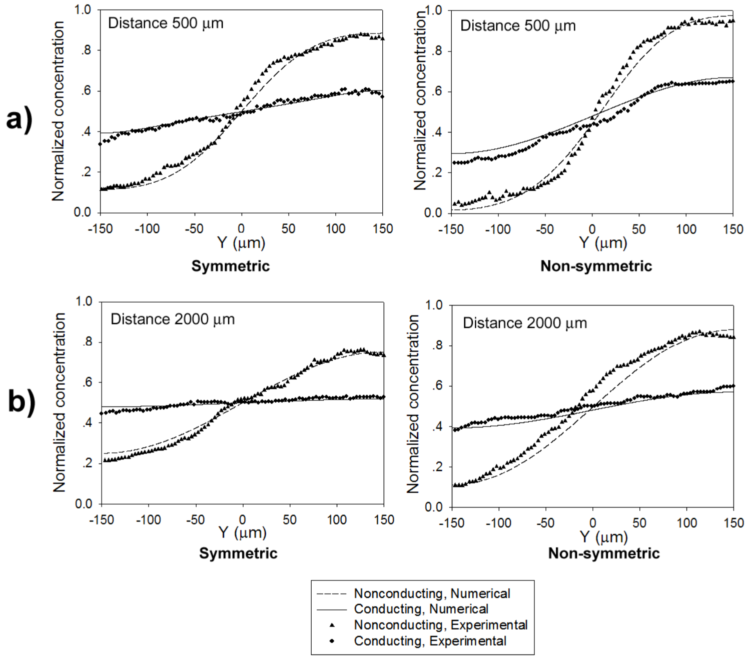

Figure 3.10 Concentration profiles under symmetric and non-symmetric hurdle placements at a downstream distance of (a) 500 μm and (b) 2000 μm

3.3.3 Numerical predictions – effects of geometry and electric field

Convinced by the above results of mixing enhancement, the effects of the hurdle geometry on the mixing enhancement were further investigated using the numerical model developed earlier. Figure 3.11a gives the flow fields of single embedded conducting hurdles with triangular, circular and rectangular shapes, respectively, under an electric strength of 100 V/cm. Figure 3.11b gives the flow fields of a triple hurdle series under the same conditions. It's found that the rectangular hurdle produces comparatively larger vortices and the triangular hurdle generates smaller vortices, implying that rectangular hurdles have a comparatively higher potential to enhance the species mixing. Also, adding more conducting hurdles will produce more vortices in the channel, as shown in Figure 3.11b. The corresponding concentration fields are given in Figure 3.12. The hurdles are placed at a distance of 3 mm from the inlet where the two streams contact, so that a stable concentration gradient will be produced right before the conducting hurdles. Clearly, the conducting hurdles produce significantly better mixing at the downstream side and the mixing effects can be further improved by using a series of conducting hurdles in the microchannel.

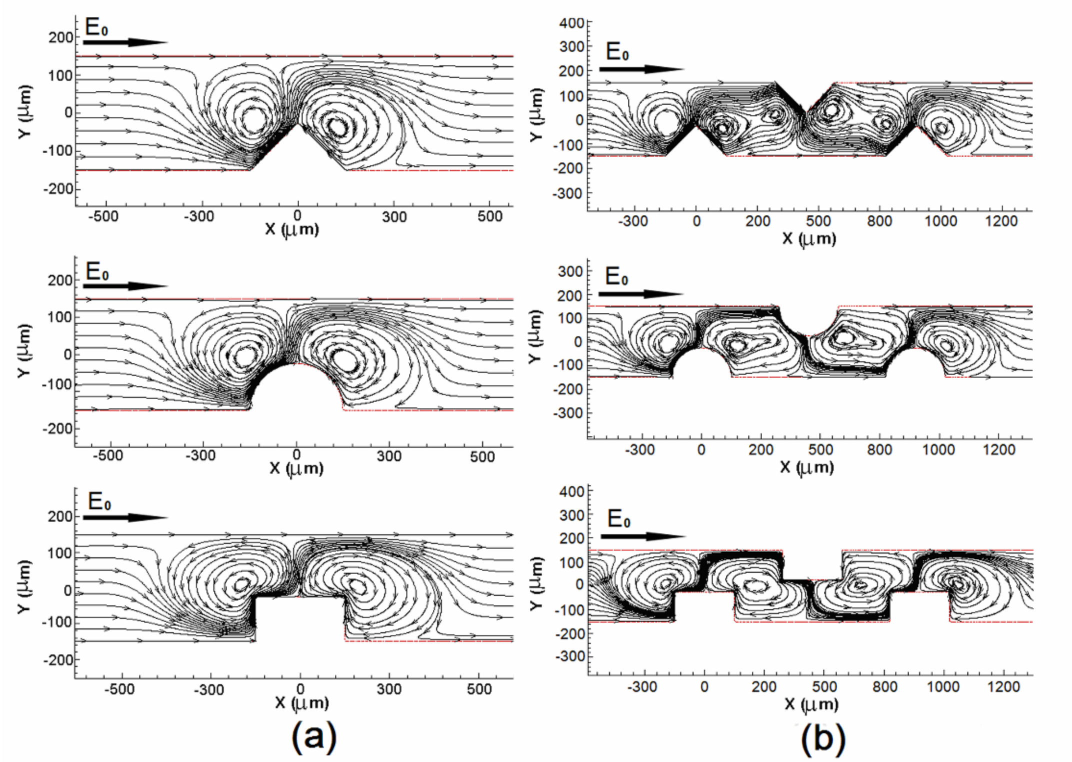

Figure 3.11 Flow fields with (a) single conducting hurdle. (b) three conducting hurdles. The lines are stream lines. E_0 = 100 V/cm.

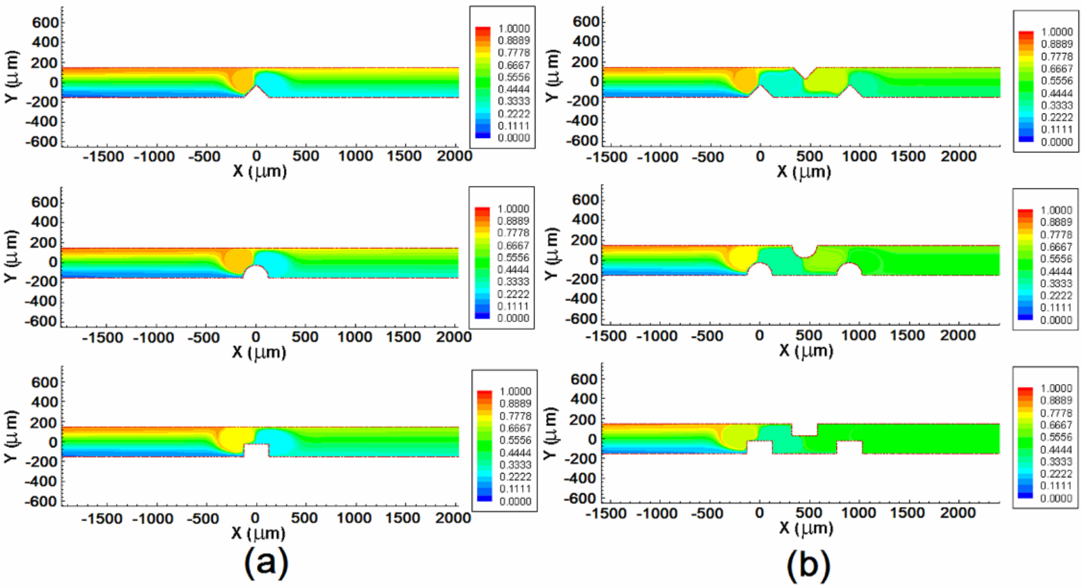

Figure 3.12 Concentration fields with (a) single conducting hurdle and (b) three conducting hurdles (E_0=100 V/cm). The color bar indicates the non-dimensional concentration.

Figure 3.13 gives the concentration profiles across the channel width at a fixed downstream position (x=1.5mm). Figure 3.13a shows the case of single embedded hurdle. Obviously, the conducting hurdles generated better mixing in comparison with non-conducting hurdles. As predicted earlier, the rectangular conducting hurdle gives the greatest degree of mixing with a mixing efficiency of 81.22%. The mixing efficiencies of the triangular and circular conducting hurdles are 62.19% and 72.23% respectively, lower than that of rectangular case but higher than the average value of non-conducting cases, which is 44.05%.

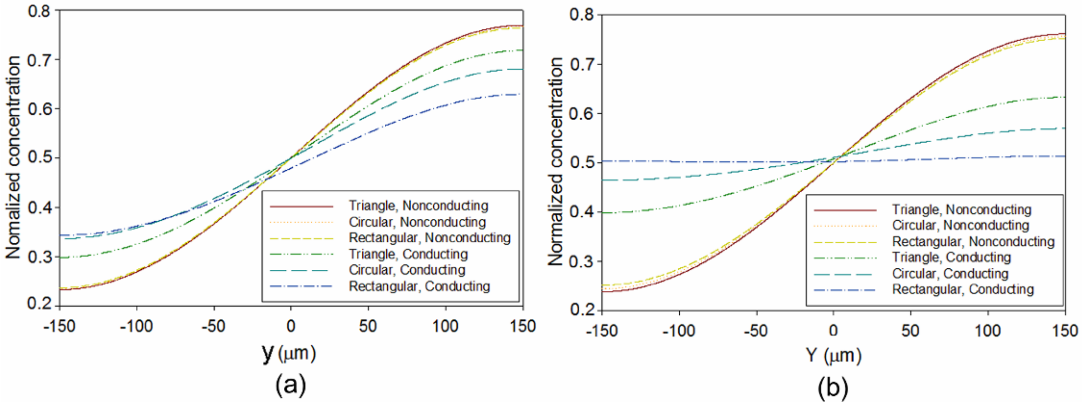

Figure 3.13 Concentration profiles across the channel width at a downstream position (x =1.5mm) under an applied potential of 100 V/cm for the configurations of a) single embedded non-conducting or conducting hurdles and b) three non-conducting or conducting hurdles.

If the single embedded hurdle is replaced by a series of multiple hurdles, as mentioned earlier, the species mixing in the microchannel can be further enhanced. Figure 3.13b gives the concentration profiles across the channel width at the same downstream position (x = 1.5 mm) with the case of triple hurdle series, the same configurations shown in Figure 11. The mixing efficiencies of the triangular, circular and rectangular hurdles are increased to 80.26%, 91.31% and 94.43% respectively, which are much higher than the average efficiency of nonconducting cases 51.5%. The rectangular hurdles still show the greatest mixing enhancement.

The dependence of the mixing on the applied electric field strength was also examined. Figure 3.14 present the mixing efficiencies varying with applied electric field strength for the cases of single hurdle and triple hurdle series, respectively. As shown in the figures, under a low applied electric field, both conducting or nonconducting hurdles give high mixing efficiencies. That's because the molecular diffusion is the dominant mixing mechanism at a low applied field, i.e., in a low speed flow. Thus, as long as the microchannel has a sufficient length, the species in the microchannel can always be well mixed after a certain distance in the channel. However, if the applied electric field is increased, the fluid convection becomes dominant over the diffusion and the mixing efficiency is decreasing rapidly if there is no flow circulation presented in the channel. However, the conducting hurdle in the microchannel produces vortices which are also dependent on the applied electric field because of the induced charge on conducting surfaces. Higher electric field will induce stronger surface charges and thus stronger local flow vortices, tending to increase the mixing efficiency. As shown in the figures, at high electric strengths, the conducting hurdles yield quite stable mixing efficiencies that are much higher than those of non-conducting hurdles. Apparently this is an effective way for fast fluid delivery with high effective species mixing. Similarly, the rectangular hurdles show the highest mixing ability, with stable mixing efficiencies of 81.18% for single hurdle configuration and 94.2% for triple hurdle series at an electric field of 150 V/cm.

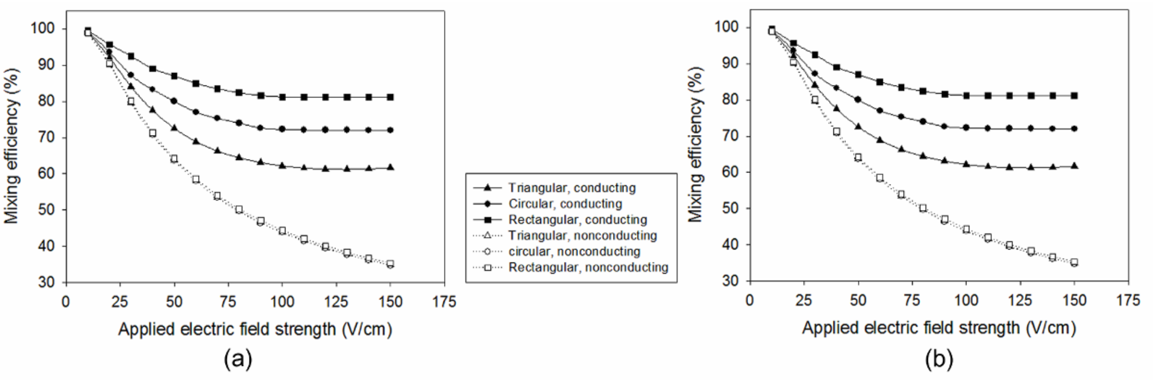

Figure 3.14 Dependence of mixing efficiency on applied electric strengths for the microchannel with a) single embedded conducting or non-conducting hurdle and b) triple conducting or non-conducting hurdle series.

3.4 Flow regulating using ICEKF

3.4.1 Local pumping mechanism of ICEKF

As mentioned earlier, the induced zeta potential has opposite signs between the upstream side and the downstream side of the conducting hurdle surfaces (Figure 3.2), resulting in the opposite driving forces for the induced EOF. Thus, if we do not consider the main flow stream generated from the non-conducting channel wall, the conducting triangle hurdles work as a pair of electrokinetic pumps with opposite pumping directions, as shown in Figure 3.15a. If the triangle hurdles have a symmetric geometry, i.e., the upstream and downstream hurdle angles are identical, the local electric field strength is symmetric, as shown in Figure. 3.15b. Additionally, the induced zeta potentials on the two sides of the symmetric hurdle have the same magnitudes but opposite signs (Figure 3.15c). According to the Helmholtz-Smoluchowski formula Eq. (3.8), the electrokinetic slipping velocities induced on the upstream and downstream hurdle surfaces have the same strength in opposite directions (Fig. 3.15d). Thus, a balance is built up between the forth and back flows and finally gives a zero net pumping effect. Mainstream EOF generated from the non-conducting channel wall will destroy this balance and result in a net positive flow.

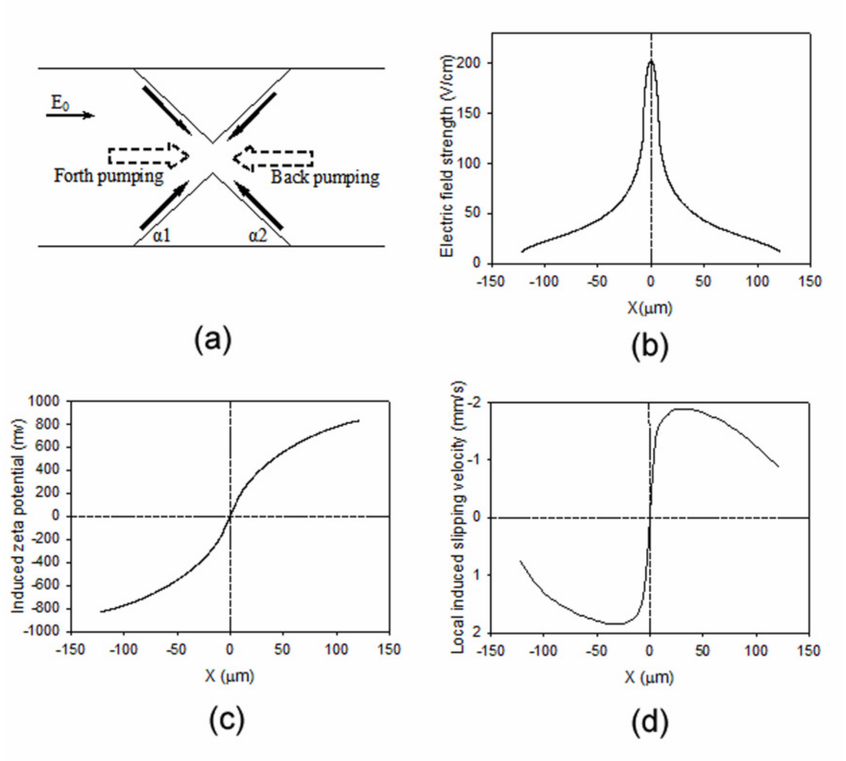

Figure 3.15 Balanced pumping effect of a pair of symmetric conducting triangle hurdles: a) schematic diagram of zero pumping effect of symmetric triangle hurdles ($\alpha 1 = \alpha 2 = 45^{\circ}$); b) local electric field strength along the hurdle surface; c) induced zeta potential distribution; d) local induced EO flow velocity. (E_0=25V/cm)

If the symmetry of triangle hurdle is broken by setting the downstream hurdle angle larger, as shown in Figure 3.16a, both the local electric field strength (Figure. 3.16b) and the induced zeta potential (Figure 3.16c) will distribute non-symmetrically. It was found that, with a larger downstream hurdle angle, the induced EOF from the downstream side of the hurdle becomes stronger (Figure 3.16d), resulting a stronger negative flow and a net backward pumping effect. This backward pumping depends on the applied electric field strength through the microchannel. Higher applied electric field will give a stronger backward pumping effect because of the nonlinear dependence of ICEKF on the electric strength. It can be expected that by adjusting the applied electric field, the backward pumping can be adjusted correspondingly to reduce, balance or overcome the mainstream flow generated from the non-conducting channel wall. Thus, a flow regulating effect can be obtained.

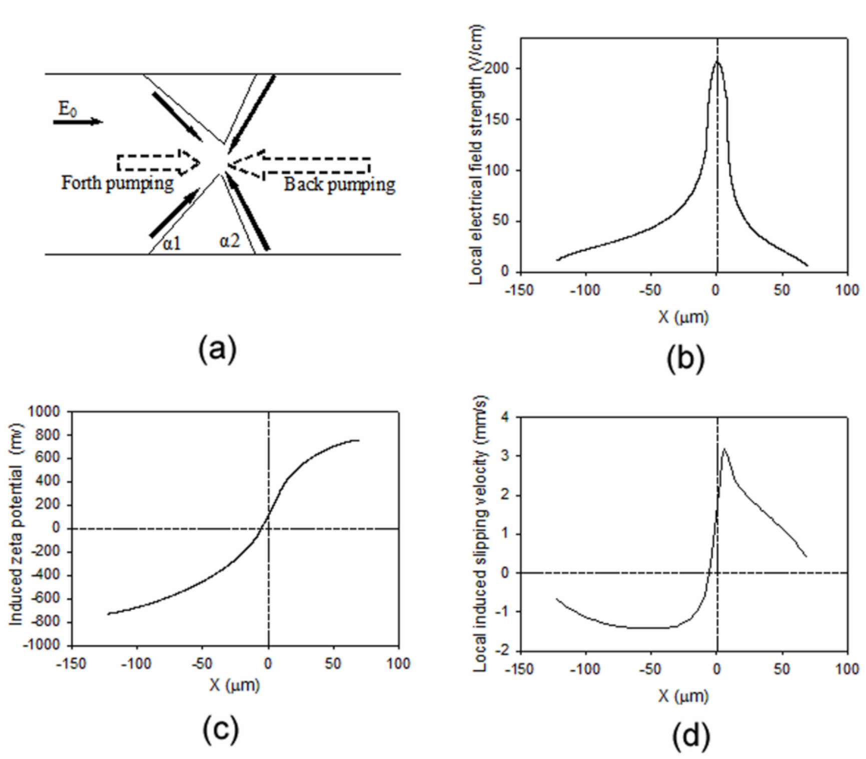

Figure 3.16 Backward pumping effect of a non-symmetric triangle hurdle pair: a) schematic diagram of net negative pumping effect of non-symmetric triangle hurdles ($\alpha 1=45^{\circ}$ $\alpha 2=60^{\circ}$); b) local electric field strength along the hurdle surface; c) induced zeta potential distribution; d) local induced EO flow velocity. (E_0=25V/cm)

3.4.2 ICEK flow regulating

As mentioned above, by introducing a non-symmetric conducting hurdle pair in the microchannel, it's possible to obtain a flow regulating effect by adjusting the external applied electric field strength. Figure 3.17 shows an enlarged view of the flow fields in the converging-diverging conjunction for the case of a pair of non-symmetric conducting hurdle ($\alpha 1=45^{\circ}$, $\alpha 2=60^{\circ}$) under three different applied field strengths, 25 V/cm, 45 V/cm and 100 V/cm, respectively. Under a comparatively weak electric field (25 V/cm), a small stream of forward flow can go through the converging-diverging conjunction, as shown in Figure 3.17a. Thus, a net positive flow is present. This is because, under such a weak electric field, the above mentioned back pumping near the conducting hurdles is not strong enough to stop the EOF generated from the upstream non-conducting channel wall. As the applied electric field strength increases, the back pumping effect is getting stronger and can block the EOF generated from the upstream non-conducting channel wall at a critical electric strength (45V/cm). That is, under such a critical electric field, no flow can go through the converging-diverging conjunction, as shown in Fig. 3.17b, equivalent to have a closed valve. If the applied electric field strength is increased further, the back flow near the downstream side of the conducting hurdles becomes stronger than the EOF generated from the upstream non-conducting channel wall. A net negative flow is formed in this case, as shown in Fig. 3.17c. Clearly, this flow regulating effect is important. It implies that we can use such a pair of non-symmetric conducting hurdles as a “valve” to control the flow rate and the flow direction simply by adjusting the applied electric field along the channel.

Figure 3.18 plots the flow rate through the channel as a function of the applied electric field strength. Clearly, the flow rate initially increases with the applied electric field and reaches a maximum positive value. After that, the flow rate begins decreasing and becomes zero at critical field strength. As the electric field increases further, the flow changes the direction and the negative flow rate increases. Thus, such electrokinetic flow regulating can be controlled by the applied electric field and no additional mechanical parts are needed.

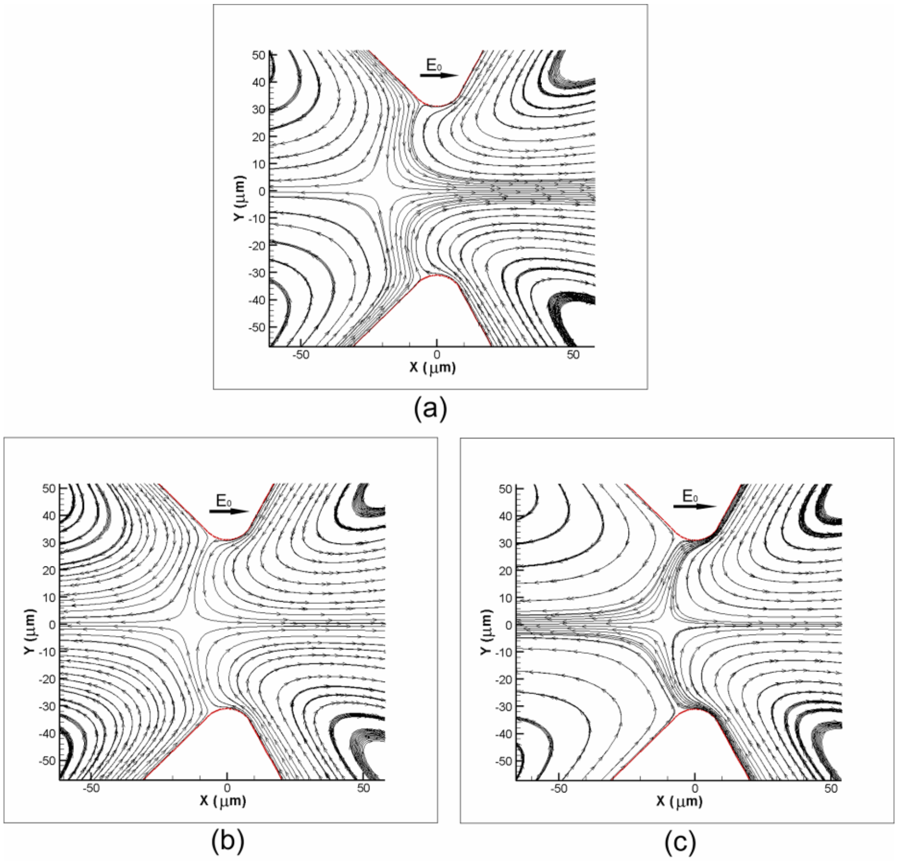

Figure 3.17 Flow fields near a non-symmetric hurdle pair (α1=45°, α2=60°) under different electric fields: (a) 25 V/cm (b) 45 V /cm (c) 100 V/cm.

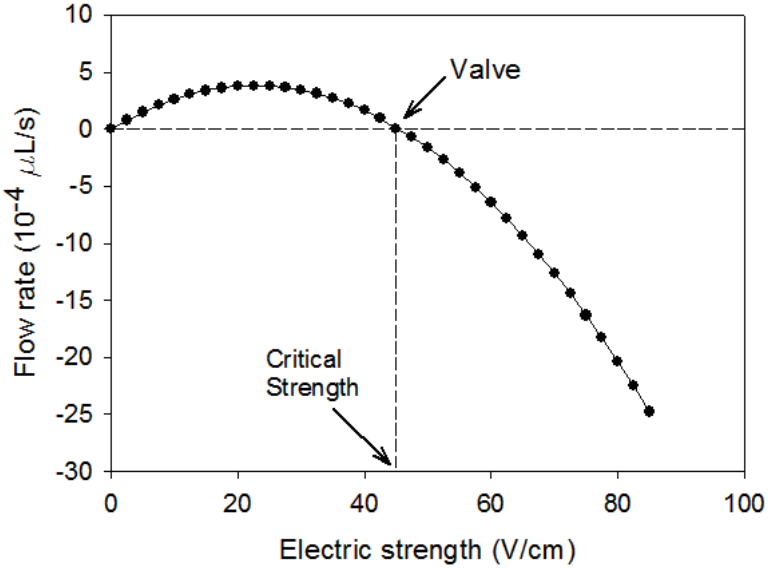

Figure 3.18 Flow rate as a function of the applied electric field strength.

3.4.3 Dimension dependence

Convinced by the above results that flow regulating effect can be obtained by adjusting the applied electric field strength, the dependence of the flow regulating on the hurdle angles was examined. Figure 3.19 shows the flow rates under different downstream hurdle angles and with a fixed upstream hurdle angel ($\alpha 1=45^{\circ}$) and fixed gap size of the converging-diverging junction, 50 μm. It's clearly seen that the flow regulating effect is dependent on the downstream hurdle angle. A smaller downstream angle gives a larger maximum value of positive flow rate and needs higher critical electric field strength to achieve the zero flow rate. It's found that there is a non-linear relation between the downstream hurdle angle and the critical field strength, as shown in Figure 3.20. It is worth to mention here that when the down stream hurdle angle approaches to the upstream hurdle angle, the critical electric field strength trends to be infinite. For a totally symmetric hurdle pair, the local forth and back pumping effects are balanced. Thus, we cannot get any stronger backward flow to balance the main EOF stream from the upstream non-conducting channel wall no matter how large the electric field strength we apply.

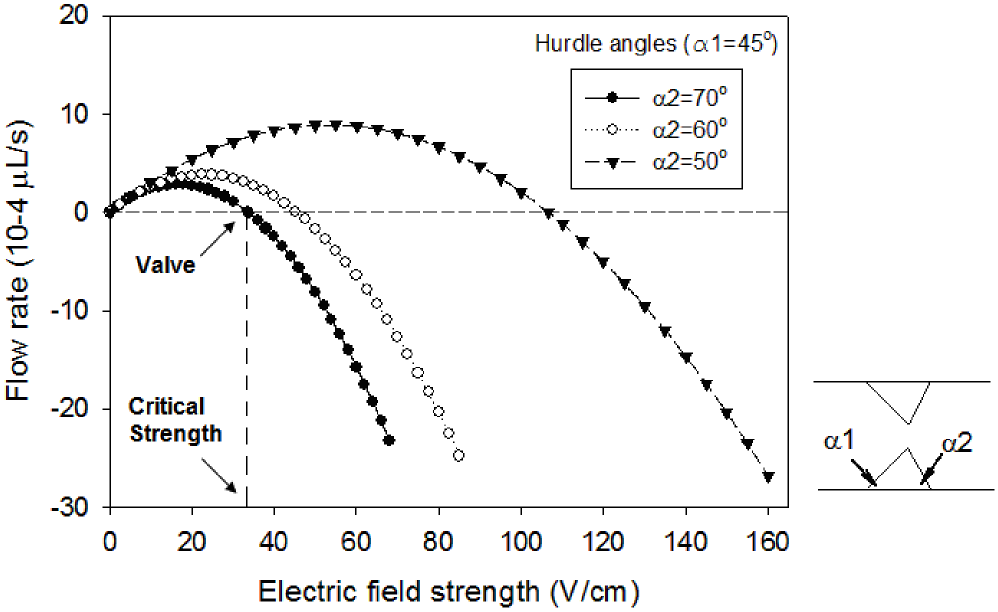

Figure 3.19 Flow rate varies with different hurdle angles and a constant gap size 50 μm

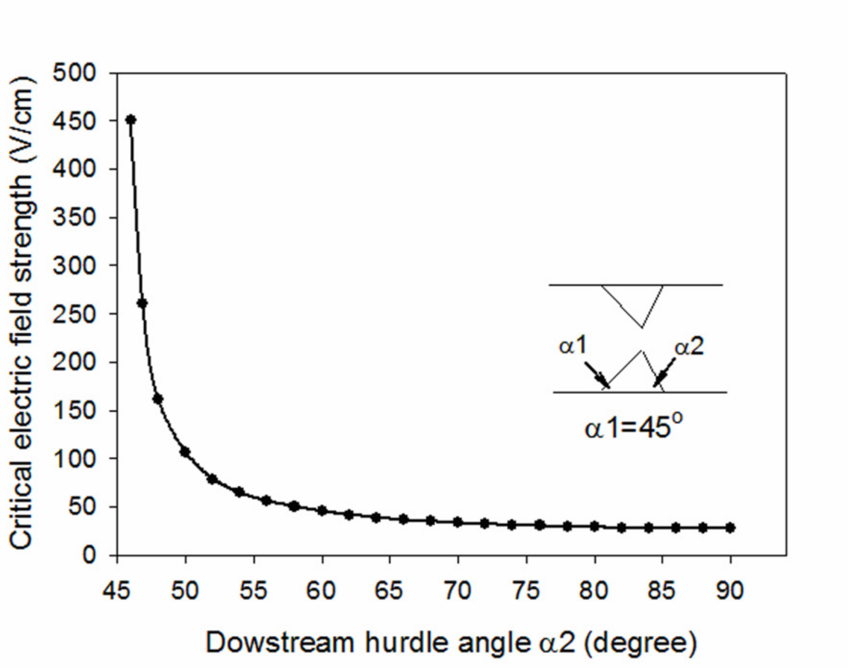

Figure 3.20 The critical electric field strength varying with the downstream hurdle angle.

The dependence of the flow regulating function on the gap size of the converging-diverging junction was also examined. Figure 3.21 shows the flow rates with different gap sizes and fixed hurdle angels ($\alpha 1$=45°, $\alpha 2$=60°). As is shown in the figure, the flow regulating effect is very sensitive to the gap size. The larger the gap size, the larger the maximum flow rate. Also, a larger gap requires a larger critical electric field to achieve the closed-valve state, i.e., zero flow rate. Figure 3.22 shows the relationship between the gap size and the critical electric field strength. It should be noted that the critical electric field strength increases very quickly with the gap size. However, under a very strong electric field, the induced-charge model discussed previously will be invalid because strong electrochemical reaction at the conductor-liquid interface will occur under strong electric field (Squires & Bazant 2004). Therefore, to obtain effective flow regulating under a relatively weak electric field, the larger gap size should be avoided. In the case studied here, the gap size of 80 μm is sufficiently large, corresponding to a maximum flow rate of 15.1×10^{-4} µL/s and a critical electric field strength of 151 V/cm.

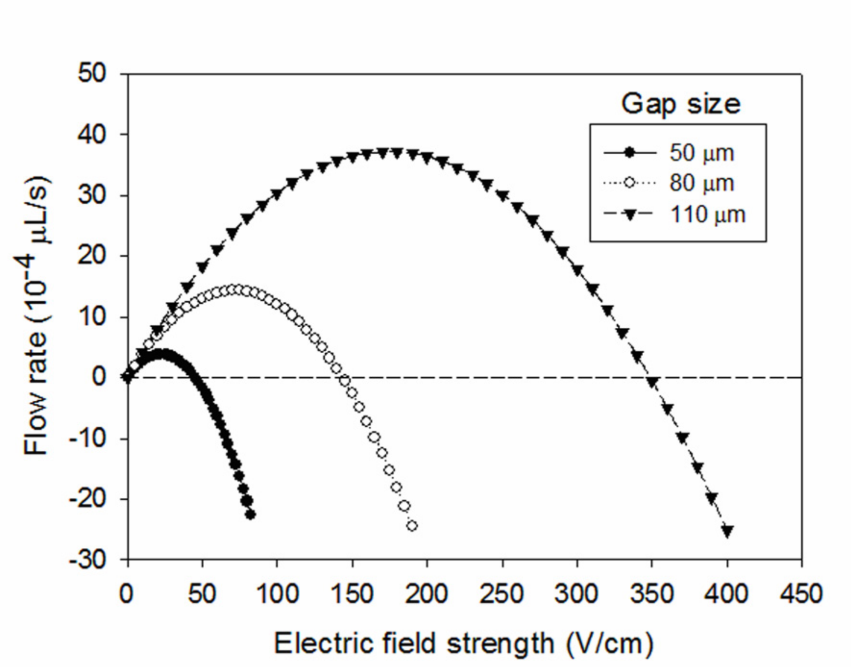

Figure 3.21 Flow rates with different gap sizes with fixed hurdle angles (α1=45º, α2=60º).

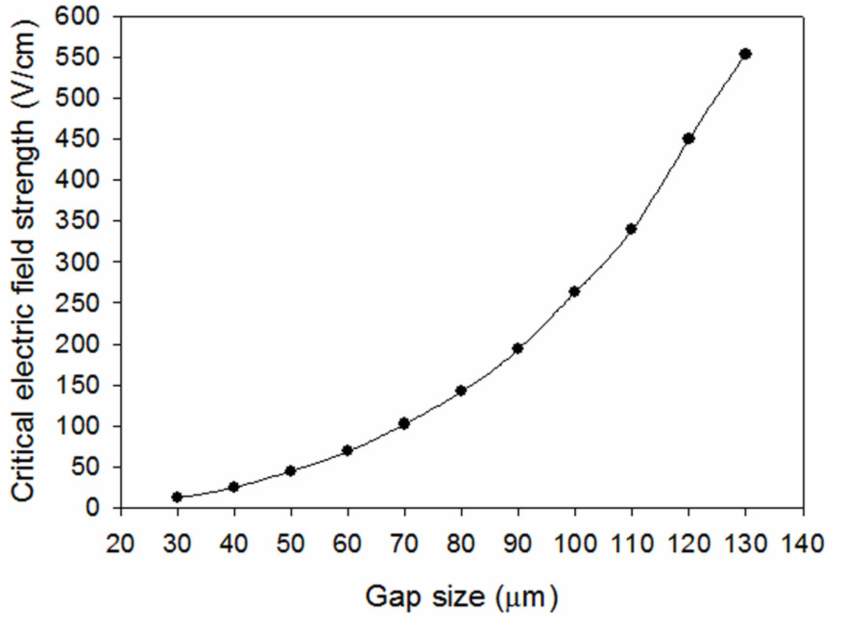

Figure 3.22 Critical electric field strength varying with the gap size under fixed hurdle angles (α1=45º,α2=60º).

3.5 Challenges in experimental studies

Induced-charge electrokinetic flow (ICEKF) mechanism studied in this chapter provides various promising lab-on-a-chip applications, such as micro vortex generation, species mixing enhancement and flow rate control in microchannels, which are numerically proven by CFD simulations. However, to fulfill the actual applications using ICEKF, experimental verifications are necessary. The micro species mixing using ICEKF was experimentally verified by using a PDMS based microfluidic device with integrated platinum triangular hurdles, as described in Section 3.3.2. However, there is still no effective way to successfully verify other phenomena, such as micro vortex generation and flow rate regulating effects. The following will discuss the challenges in the experimental verifications of ICEKF.

As discussed earlier, by introducing electric conducting hurdles into microchannels, micro vortexes can be generated near the conducting hurdle surfaces because of the non-linear induced zeta potential distribution along the hurdle surfaces. The vortexes can be used to enhance the species mixing, which was successfully verified. However, the visualization of the vortex structures in the microchannel is still a difficult task. As we know, particle image velocimetry (PIV) technique (Adrian 1984) is an effective way to visualize complex flow structure, which measures local fluid velocities in a fluid flow by optically observing large numbers of particles that are suspended in the fluid and move with it. However, the visualization of ICEKF structure using this method was not successfully. The major reason is that the conducting hurdles imbedded in the channel carries strong induced surface charge under an applied electric field. And on the other hand, the micro particles generally carry fixed electrostatic surface charge when contacting with an aqueous solution. Thus, the particles are easily attracted to the hurdle surface and huge particle adhesions on the hurdle surface will be obtained, as shown in Figure 3.23. As the result, the induced charges on hurdle surfaces will be basically neutralized because of the particle adhesions. The ICEK effects discussed earlier will totally disappear and no flow circulating structure could be obtained.

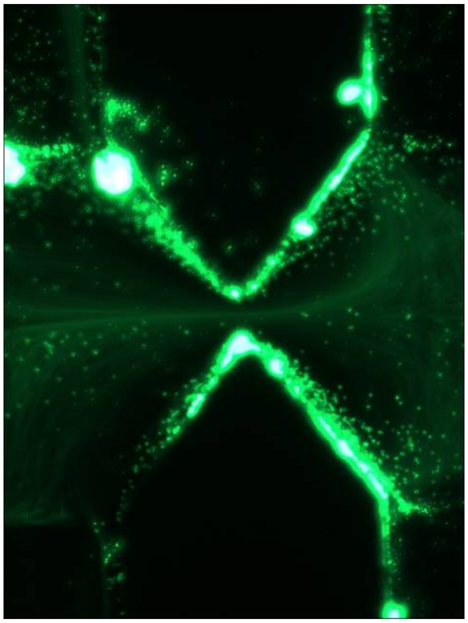

Figure 3.23 Particle adhesions to the surfaces of the imbedded conducting hurdles

Another challenge lies in the experimental verification of the flow regulating effect discussed in Section 3.4. The numerical prediction indicated that a flow rate regulating effect can be obtained by using a pair of asymmetric triangular hurdles embedded in the middle of a microchannel. However, to directly test this effect is challenging because of the distorted flow field in the microchannel. The non-uniform flow field leads difficulties of direct measurement of flow rate in the channel. Thus, an indirect flow testing approach seems necessary.

To fulfill this task, a particle tracking technique (Wu et al 2008) was designed. The schematic experimental setup is shown in Figure 3.24. Two small gaps with the sizes of 10 μm and 15 μm are fabricated at the downstream side of the microchannel after the embedded asymmetric triangular conducting hurdles. Non-conducting small particles with diameters of 2 μm are loaded into the microchannel from the upstream inlet. It's proved that, when a particle is passing through a small gap, an electric resistance change in the channel causes a current jump, which can be captured as a visualized signal using a differential amplification system (Wu et al 2008). Thus, the time period needed for a particle passing through both the two gaps can be interpreted as the distance between the two current signal peaks, which gives an estimation of the average particle velocity as

$$V_{particle} = d/\Delta t \tag{3.16}$$

where d is the average length between the two gaps and Δt is the time distance measured from the signal pair. This gives an approximation of the average flow velocity in the channel. On the other hand, the current signal intensity shows strong dependence on the gap size and smaller gap will give stronger signal peak (Wu et al 2008). Thus for a positive flow, the particle will pass through the smaller gap first, resulting in a bigger signal followed by a smaller signal. For a negative flow, the particle will pass through the bigger gap first, resulting in a smaller signal followed by a bigger signal. This was intentionally used to judge the flow direction in the channel thus capture the flow regulating effect.

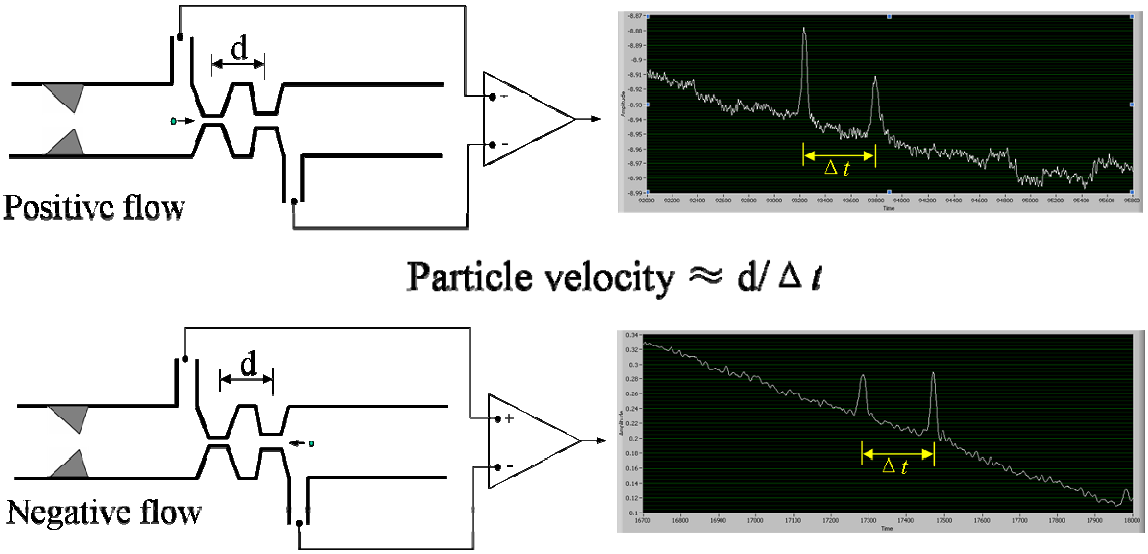

Figure 3.24 Experimental setup of ICEK flow regulating verification

However, the designed experimental verification of ICEK flow regulating didn’t work successfully. The reason was that the particle’s motions were still found non-uniform at the downstream side of the channel. We could not get uniform particle motions across the two gaps under a specified electric field. Figure 3.25 reflects this fact. The figure shows the particle motions right before the first gap at the downstream side of the microchannel under an electric field of 75.5 V/cm. As is shown in the figure, the particles were moving in different directions, those particles close to the channel wall were moving in positive direction while the particles close to the channel center moving in negative direction. Thus, we could not judge the flow direction by tracking the particle's motion like this.

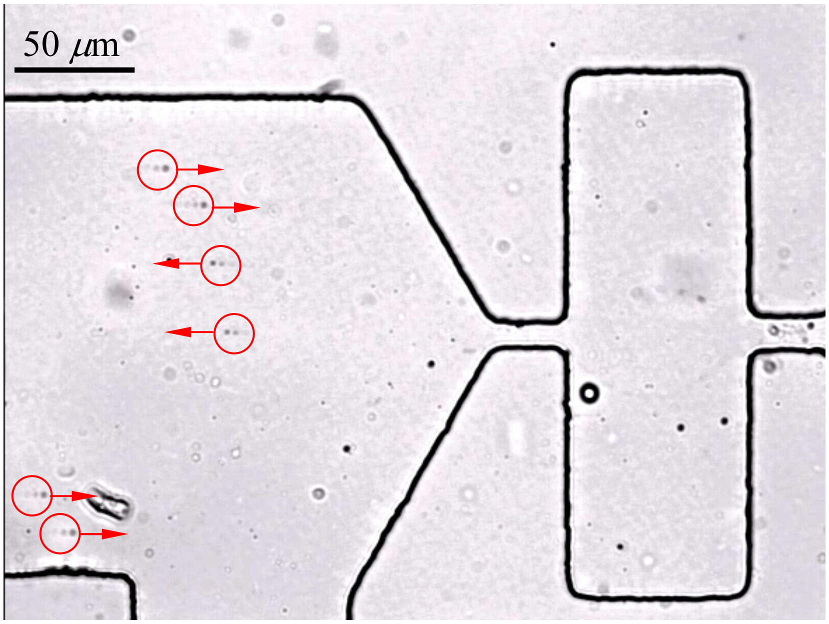

Figure 3.25 Particle motions at the downstream side of the microchannel (E_0= 75.5 V/cm)

To investigate the reason behind the failure of the experiment, we simulated the flow patterns at the downstream side of the channel under various electric fields. Figure 3.26 shows the velocity profiles at downstream side under the electric fields of 25 V/cm, 45 V/cm and 100 V/cm, corresponding to the cases (as indicated in Figure 3.17) of positive, zero and negative flow rates respectively. As is shown in the figure, under a weak electric field, the flow streams in the channel are all positive, giving a positive flow rate. When the electric increases to a critical value (45 V/cm), a valving effect with a zero flow rate is obtained. However, a zero flow rate in this case doesn't mean still flow in the channel. As is seen in the figure 3.26b, we get positive flow streams close to the channel wall and negative flow streams close to the channel center. This is because the channel walls are charged with a constant negative zeta potential (-50 mV), thus the flow velocity on the channel wall is always positive no matter how large the electric is applied. Thus, to fulfill the zero flow rate in the channel, a back flow is induced near the channel center, which implies a huge flow circulation exists in our system. Thus, if we put the particles into the channel, the particles will basically move in different directions, depend on where the particles are placed. This gives the reason why we could not get the information about the flow direction by tracking particles only. Similarly, when the electric field is further increased, the flow rate becomes negative and the back flow near the channel center gets stronger, as seen in Figure 3.26c. But the channel wall still carries positive flow velocities.

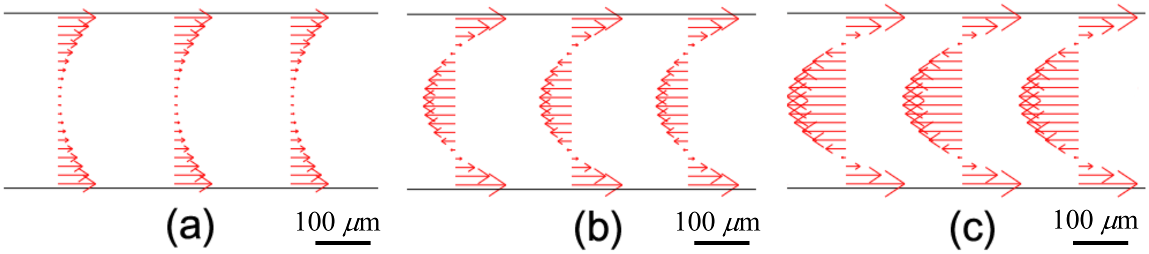

Figure 3.26 Flow profiles at the downstream side of the microchannel under the electric fields of a) 25 V/cm, b) 45 V/cm and c) 100 V/cm.

As discussed above, the flow field visualization of ICEKF and the verification of ICEK flow rate regulating are still challenging under current experimental conditions. Potentially, the caged-dye based velocimetry (Sinton & Li 2003) could be used to visualize cross-section flow profiles in a microchannel as those indicated in Figure 3.26. But the experimental verifications of the actual micro circulations and the flow regulating effect still require further investigations.

3.6 Summary

Induced-charge electrokinetic flow (ICEKF) in a microchannel with embedded conducting hurdles is studied in this chapter. A numerical scheme is provided to simulate the flow and concentration fields in the microchannel. The numerical results show that an induced non-uniform zeta potential distribution on the conducting surfaces causes varying electroosmotic flow velocity on the hurdle surfaces and circulating flows near the hurdles.

The simulation demonstrated that the species mixing can be enhanced significantly by the vortices near the hurdles. The mixing effect was validated experimentally using PDMS microchannels with embedded platinum hurdles. Both symmetric and non-symmetric hurdle placement patterns were tested in experiments, and the former showed a better ability to enhance the species mixing. The effects of hurdle geometry and the applied field on the flow mixing were investigated numerically. It’s found that the degree of enhancement highly depends on the hurdle geometry. Among the three hurdle shapes tested in this study, the rectangle hurdle produces the strongest mixing effect. Also, the mixing can be further enhanced by adding more conducting hurdles in series in the microchannel because of the more flow vortices produced. The conducting hurdle method provides a way to make fast liquid delivery with a comparatively stable and high mixing efficiency under strong applied electric field.

A flow regulating effect can be obtained by adjusting the electric field strength applied through the microchannel when a pair of non-symmetric conducting hurdle is employed. This flow regulating effect can be used to achieve different flow rates in different directions and the closed-valve state (zero flow rate). The flow regulating effect depends on the dimensions of the converging-diverging section. In the cases where the downstream hurdle angle is close to the upstream hurdle angle, or a larger gap size is used, a larger critical electric field strength is required to attain the zero flow rate. The critical electric field is more strongly dependent on gap size than on the hurdle angle. To obtain effective flow regulating under a relatively weak electric field, the combination of larger downstream hurdle angle and smaller gap size is recommended.

This study suggests a new and simple ICEKF method for enhanced flow mixing and flow regulating with simple fabrication and easy operation. The induced-charge electrokinetic flows described in this study can be used in various microfluidics and lab-on-a- chip applications.

CHAPTER IV

INDUCED-CHAGE ELECTROPHORESIS OF CONDUCTING PARTICLES

This chapter describes induced-charge electrophoretic (ICEP) motion of conducting particles in microchannel. A complete theoretical model of ICEP motion is set up and a moving grid technique is proposed to numerically solve the particle-liquid coupled multi-physics system. The ICEP motions of conducting particles under various conditions are successfully simulated. The corresponding effects of micro vortex generation, particle-wall interaction and particle-particle interaction are discussed.

4.1 Introduction

As indicated in Chapter II, electrophoresis is the migration of charged particles in solution in response to an electric field. The rate of migration depends on the strength of the electric field, the net surface charge, the size and shape of the particles, the ionic concentration, the viscosity and temperature of the medium in which the particles are moving. Electrophoresis has been one of the most widely used techniques for the separation of particles or biological cells. It has been applied in various disciplines such as biochemistry (Acquaah, 1992; Allen, 1994; Cheng and Mitchelson, 2001; Westermeier and Gronau, 2001), pharmaceutical science (Neubert and Rüttinger, 2003), biomedical science (Altria, 1996; Shintani and Polonský, 1997; Palfrey, 1999; Keren, 2003), food analysis (Frazier, 2000), environmental science (Shintani and Polonský, 1997; EI Rassi, 2002; Thibault and Honda, 2003), and etc.

There are two major electrophoretic separation methods currently in use: gel electrophoresis and capillary electrophoresis. In Gel electrophoresis, the composition of either agarose or polyacrylamide works as a separating medium in which macromolecules migrate in the presence of an electric field. The matrix formed by the gel creates a sieve-like screen used to sort the macromolecules. Gel electrophoresis produces high-resolution analysis, however, it has several disadvantages (Landers, 1994). The most obvious disadvantage is the speed of separation, which is ultimately limited by Joule heating (the heating of a conducting medium as current flows through it). The relatively poor heat dissipation restrains the use of low electric field. Compared with gel electrophoresis, capillary electrophoresis is a unique approach to separation and has several advantages. Generally, capillaries are made from fused silica with typical internal diameters of 10~200μm and length of 10~100cm. The required buffer solution is filled into the capillary, sample solution is then introduced at the end of the capillary, and the capillary ends are then dipped into reservoirs containing high-voltage electrodes and the required buffer solution. In capillary electrophoresis, the high surface-to-volume ratio of capillaries allows for the very efficient dissipation of Joule heat generated from applied fields, and the small cross-sectional area of the capillary permits a relatively low current even with high voltage. Thus, the high electric field up to 800V/cm can be applied to capillary and gives a relatively quick separation for a short period.

The rapid development of microfluidic lab-on-a-chip technology provides an alternative separation technique. On a microfluidic chip, electroosmotic flow (EOF) can be used as a pumping mechanism, allowing for fluid transport within the chip, without a need for pumps or even valves. Chemical reactions can be performed on-chip, followed by dispensation, separation and detection of the products. The cells or particles move through a relatively small microchannel (or capillary). The existence of the channel wall or other particles will influence the electrophoretic motion. Thus, it is important to understand the particle electrophoretic motion in a microchannel with various influences, such as the size and shape of particles, channel wall effects, zeta potentials, applied electric potentials and transient effects. So far almost all studies of electrophoresis are focused on non-conducting particles. Very little is known for the electrophoretic behavior of electrically conducting and polarizable particles. With the rapid development of microfluidics and nanotechnology, various electrically conducting and polarizable particles (e.g., carbon, gold, silver, and nickel) are involved in microfluidic systems for variety of applications such as biochemical sensing, separation and particle production (Lin et al. 2007; Sparks et al. 2003; Shim et al. 2008; Boleininger et al. 2006). Thus, the earlier mentioned induced-charge electrokinetics (ICEK) will play a very important role and it is important to develop fundamental understanding of the induced-charge electrophoretic (ICEP) motion of electrically polarizable conducting particles.

The induced-charge electrophoretic motion of polarizable particles has been studied for years. Yariv (2005) developed a general model to calculate the induced-charge electrophoretic (ICEP) velocities of non-spherical polarizable particles. A more systematic theoretical model of ICEP motion of polarizable particles was recently proposed to study the dependence of the ICEP velocities and directions on the effects of broken geometry symmetry (Squires & Bazant 2006). The transient alignment of asymmetric polarizable particles was theoretically studied (Squires & Bazant 2004; Yariv 2005; Squires & Bazant 2006) and similar effect was found in the ICEP dynamics of rod-like metal particles (Rose et al. 2007). Saintillan et al (2006) analyzed far-field hydrodynamic interactions in the ICEP of colloidal rod dispersions using a statistical method. Yossifon et al (2007) studied the rotational ICEP motion of a polarizable dielectric spheroid in the presence of a uniform arbitrarily oriented external electric field.

For real microfluidic applications, the change of microchannel geometry (i.e., size and turns) and the particle's position to the wall will change the local electric field, and hence the induced charge electrophoretic motion of polarizable particles will be transient generally. Additionally, the existence of channel wall will produce electroosmotic flow and definitely affect the particle motion. So far, there are a few published works studying the wall effects on induced-charge electrokinetics. Levitan et al. (2005) studied the perturbation of the ICEO flow around a metal cylinder in contact with an insulating wall in a slit microchannel and Zhao & Bau (2007) analyzed similar problem with a 2-D ideally polarizable cylindrical particle positioned next to a planar surface both under the thin and thick double layer approximations and calculated the electrostatic and hydrodynamic forces on the particle, but both works did not consider the cylinder's motion. Gangwal et al (2008) experimentally studied the translational ICEP in microfluidic devices and observed the attraction of Janus particles to a glass wall.

To fulfill fundamental understanding of the characteristics of the electrophoretic motion of particles in microchannels, either physical experiments or theoretical modeling combined with numerical simulation can be utilized. Physical experiments are fundamental in understanding basic physical phenomena and setting up basic laws of physics to either explain physical phenomena that have been observed or predict what will happen in future. Since physical experiments are always costly, they cannot be applied under every circumstance. On the other hand, for complex systems, due to complicated coupling multi-physical effects, observation made from experiments are not always easy to either reveal real nature of physical phenomena or to be interpreted. Because of this, numerical simulations provides a feasible alternative to study the physical phenomena taking place in complex systems through verified numerical methods based on rigorous theories. So far, there is no published work conducting complete transient numerical simulation of ICEP motion of ideally polarizable particles and all the above mentioned systematic theoretical works (Yariv 2005; Squires & Bazant 2006) developed the ICEP models using steady flow approximations on an unbounded large field with no channel wall effects.

This chapter presents a computational fluid dynamics (CFD) based numerical simulations of transient ICEP motion of ideally polarizable conducting particles. A complete time-dependant coupled multi-physics model is set up to describe the nonlinear ICEP phenomena, which combines the basic principles of continuum fluid flow, induced-charge electric double layer, electroosmosis and electrophoresis. The effects of micro vortex generation, particle-wall interaction, particle-particle interaction, electric field strength, particle size, particle densities and the corresponding potential microfluidic applications are discussed.

4.2 Theoretical model of induced-charge electrophoresis

4.2.1 Problem definition and assumptions

This study initially considers a simplified 2-D particle-channel system: a circular conducting particle moving in a straight slit channel, as shown in Figure 4.1. The microchannel is horizontally located and is filled with aqueous electrolyte solutions whose concentrations are higher than 20mM (which implying the assumption of the thin electrical double layers). The ends of the channels are connected to open reservoirs, so that no overall pressure gradient is present in the systems. The channel wall carries uniform negative electrical charges that are characterized by the zeta potential ζ_w. The particle is perfectly conducting and is assumed initially electric neutral. An external electric field is applied uniformly along the channel. The density of the particle is assumed to be the same as that of the aqueous solution so that the gravitational force and the buoyancy force can be neglected. The particle and the channel wall are rigid and the aqueous electrolyte solution is Newtonian and incompressible.

As indicated in chapter II, when the particle is initially immersed in the external applied electric field, a non-zero current drives ions in the aqueous solution into the conducting surface. The current drives positive ions into a thin layer on one side of the particle and the negative ions into the other, inducing an equal and opposite surface charge on the opposite side surfaces of the particle (see Figure 4.1). Consequently, a dipolar screening cloud of ions adjacent to the solid-liquid surface is forming in the liquid. After the immediate polarization of the particle, the particle behaviors like an insulator because an induced dipolar double layer is formed. Then, a steady-state electric field is established. This steady-state electrostatic configuration is equivalent to the no-flux electrostatic boundary condition assumed in standard electrokinetic analysis. The resultant induced steady-state zeta potential on the particle surface ζ_p is proportional to the local electric strength E and varies with position on the conducting surface, resulting in micro vortices generated near the particle surface. On the other hand, the fixed charges on the non-conducting channel wall will also cause a main stream electroosmotic flow (EOF) in the channel, brings the particle into motion.

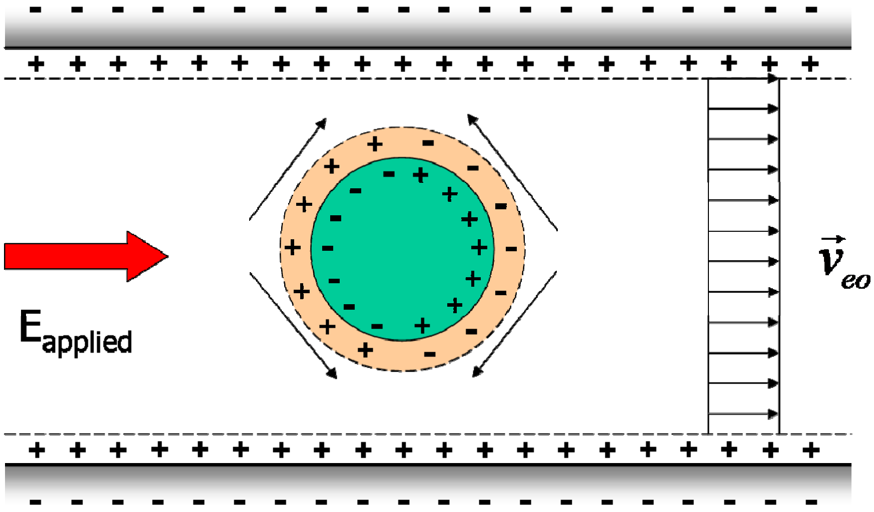

Figure 4.1 Schematic diagram of induced-charge electrophoresis of conducting particle

4.2.2 Electric field and flow field

Once the particle is perfectly polarized and a steady state induced double layer is setup on the conducting surface, the applied electrical potential in the liquid ϕ_e is governed by the Laplace's equation

$$\nabla^2\phi_e = 0 \tag{4.1}$$

and the corresponding boundary conditions:

$$n\cdot\nabla\phi = 0 \text{ at channel wall and particle surface} \tag{4.2}$$

$$\phi = \phi_0 \text{ at channel inlet} \tag{4.3}$$

$$\phi = 0 \text{ at channel outlet.} \tag{4.4}$$

The equations governing incompressible liquid flow are the Navier-Stokes equation and the continuity equation.

$$\rho\left[\frac{\partial\vec{u}}{\partial t}+\vec{u}\cdot\nabla\vec{u}\right]=-\nabla p+\mu\nabla^2\vec{u} \tag{4.5}$$

$$\nabla\cdot\vec{u}=0 \tag{4.6}$$

with the boundary conditions (Ye and Li, 2004)

$$\vec{u}=-\frac{\varepsilon_0\varepsilon\zeta_w}{\mu}\vec{E} \quad \text{at channel wall} \tag{4.7}$$

$$\vec{u}=\vec{V}_p+\vec{\omega}_p\times\left(\vec{x}-\vec{X}_p\right)-\frac{\varepsilon_0\varepsilon\zeta_p}{\mu}\vec{E} \ \text{ at particle surface} \tag{4.8}$$

$$\vec{n}\cdot\nabla\vec{u}=0 \ \text{ at inlet and outlet} \tag{4.9}$$

where ζ_w is the zeta potential on the channel wall, $\vec{E}=-\nabla\phi_e$ is the local applied electric field, $\vec{V}_p$ is the translational velocity of the particle, $\vec{\omega}_p$ is the rotational velocity of the particle, $\vec{x}_p$ is the position vector on the particle surface, $\vec{X}_p$ is the position vector of the particle center and ζ_p is the induced nonlinear zeta potential on the particle surface, given by Eq. (2.13) and Eq. (2.14).

Here, the transient term in Eq. (4.5), $\frac{\partial\vec{u}}{\partial t}$ can not be dropped off because the system is physically time-dependent. The particle considered in the system has a fairly big size (20~30 μm) which can not be negligible compared with the channel size (100 μm ~300 μm). The fluid flow induces the particle's motion and the particle itself will also affect the flow field. Thus the model presented here describes a coupled transient particle-fluid interaction.

4.2.3 Particle motion

Since the particle carries induced surface charge, there is electrostatic force acting on the particle by the applied electric field. At the same time, the flow field exerts a hydrodynamic force on the particle. The net force acting on the particle is (Ye & Li 2004)

$$\vec{F}_{net} = \vec{F}_E + \vec{F}_h \tag{4.10}$$

where F_E is electrostatic force and F_h is total hydrodynamic force, which combines two components

$$\vec{F}_h = \vec{F}_{ho} + \vec{F}_{hin} \tag{4.11}$$

where F_{ho} is the hydrodynamic force acting on the particle by the liquid flow in the region outside the EDL, and F_{hin} is the hydrodynamic force acting on the particle by the liquid flow in the region inside the EDL.

In the model presented here, the electrical double layers are assumed thin so that the Debye length can be neglected in comparison with the size of the particle (20~30 μm) and the size of the channel (100~300 μm). Thus, detailed flow field in the region inside the EDL will not be considered, and the effect of flow field in the EDL is replaced by the electroosmotic velocity which acts as a slipping flow boundary condition for the flow field in the region just outside the EDL. In this way the flow field around the particles is the flow field originated outside the EDL and subject to the slipping flow boundary condition at the particle surface. Under this assumption, it can be shown that the F_E is balanced by F_{hin}, and the net force on the particle is thus given by (Ye & Li 2004)

$$\vec{F}_{net} = \vec{F}_{ho} = \vec{G} - \oint_{\Gamma} \sigma_p \cdot \vec{n} \mathrm{dS} = (\rho - \rho_p) g V_p - \oint_{\Gamma} \sigma_p \cdot \vec{n} \mathrm{dS} \tag{4.12}$$

and the total torque acting on the particle is given by

$$T_{net} = -\oint_{\Gamma} (\vec{x}_p - \vec{X}_p) \times (\sigma_P \cdot \vec{n}) \mathrm{dS} \tag{4.13}$$

where $\vec{G}$ is the total body force, ρ_p is the density of the particle, V_p is the volume of the particle, g is acceleration due to gravity and σ_p is the stress tensor given by

$$\sigma_p = -p\bar{\bar{I}} + \mu\left[\nabla\vec{u} + (\nabla\vec{u})^T\right] \tag{4.14}$$

where $\bar{\bar{I}}$ is identity tensor.

The Newton's second law governs the particle motion. The equations governing the particle motion are

$$m_p \frac{\mathrm{d}\vec{V}_p}{\mathrm{d}t} = \vec{F}_{net} \tag{4.15}$$

$$J_p \frac{\mathrm{d}\vec{\omega}_p}{\mathrm{d}t} = \vec{T}_{net} \tag{4.16}$$

where m_p and J_p are the mass and the moment of inertia of the particle, respectively. The displacement of the particle center is governed by

$$\frac{\mathrm{d}\vec{X}_p}{\mathrm{d}t} = \vec{V}_p \tag{4.17}$$

The initial conditions of the particle motion and the flow velocity are set as zero, that is

$$\vec{V}_p\Big|_{t=0} = 0,\ \vec{\omega}_p\Big|_{t=0} = 0 \text{ and } \vec{u}\Big|_{t=0} = 0 \tag{4.18}$$

In the development of the numerical simulation, the following non-dimensionalized parameters were used:

$$\bar{\phi}_e = \frac{\phi_e}{\zeta_w},\ \bar{\vec{u}} = \frac{\vec{u}}{U_{\text{ref}}},\ \bar{\vec{x}} = \frac{\vec{x}}{d},\ \bar{t} = \frac{t}{d / U_{\text{ref}}},\ \bar{P} = \frac{p - P_a}{\rho U_{\text{ref}}{}^2},\ \bar{\vec{E}} = \frac{\vec{E}}{\zeta_w / d}$$

where $U_{\text{ref}} = \frac{\varepsilon\varepsilon_0}{\mu} \cdot \frac{\zeta_w}{d}$ is the reference velocity.

4.3 Two-dimensional numerical simulation of ICEP

The theoretical model established above, i.e. Eqs. (4.1), (4.5), (4.6), (4.15), (4.16) and (4.17), describes a totally coupled multi-physics system. The most notable feature of the model is that, because of the particle motion, the boundaries of the computational domain are no longer fixed. The boundary corresponding to the particle's surface is moving and thus a moving mesh technique is necessary to carry out the transient numerical simulation. A technique called Arbitrary Lagrangian-Eulerian (ALE) provides a solution to this issue.

4.3.1 Arbitrary Lagrangian-Eulerian (ALE) moving mesh technique

The Arbitrary Lagrangian-Eulerian (ALE) technique (Hughes et al., 1981; Donea et al. 1982) provides a method to track the moving boundary of the variable computational domain by mapping its initial fixed mesh node coordinates (X,Y) to the deformed spatial coordinates (*x,y*) corresponding to the moving geometry of the fluid-particle system. The mapping functions are given by

$$x = x(X, Y, t) \tag{4.19a}$$

$$y = y(X, Y, t) \tag{4.19b}$$

where *t* is time. For this model, we assume that initially, at *t*=0, the two coordinate systems coincide. Therefore, the mapping says that the node point initially located at (*X,Y*) moves to the moving point (*x,y*) at *t*, as shown in Figure 4.2.

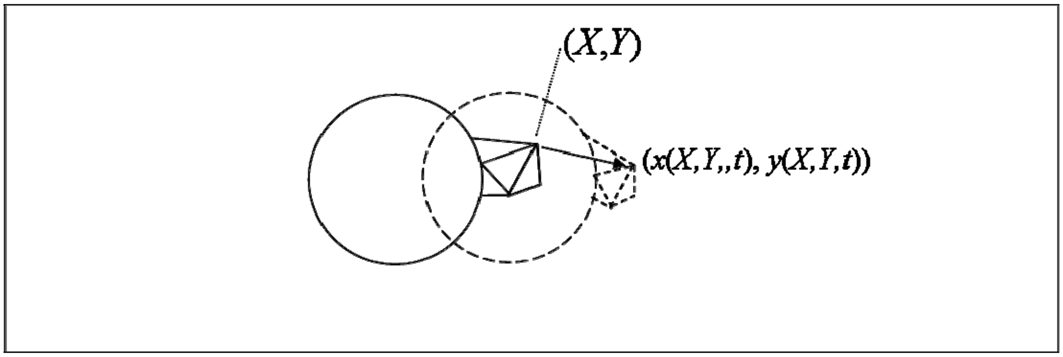

Figure 4.2 Schematic diagram of the coordinate mapping in a fluid-particle system

Thus the original ICEP model based on the moving coordinates (*x,y*) can be transformed to a model based on the fixed coordinates (*X,Y*) using the following coordinate transformation

$$dxdy = \left|J\right| dXdY \tag{4.20}$$

where *J* is the Jacobian matrix of the transformation, given by

$$J = \begin{pmatrix} \dfrac{\partial x}{\partial X} & \dfrac{\partial x}{\partial Y} \\ \dfrac{\partial y}{\partial X} & \dfrac{\partial y}{\partial Y} \end{pmatrix} \tag{4.21}$$

For a particle-liquid system, the mesh motion in the interior of the fluid can be assumed to satisfy Laplace's equation to guarantee its smooth variation (Hu et al. 1992)

$$\nabla^2 \psi_x = 0 \tag{4.22a}$$

$$\nabla^2 \psi_y = 0 \tag{4.22b}$$

$$x = X + \int_0^t \psi_x \mathrm{dt} \tag{4.23a}$$

$$y = Y + \int_0^t \psi_y \mathrm{dt} \tag{4.23b}$$

where $(\psi_x, \psi_y) = \bar{\psi}$ is the mesh velocity in the deformed coordinates. The boundary conditions for the mesh movement are given so that on the fluid-particle interface the mesh velocity equals the velocity of the particle.

Comsol Multiphysics® 3.2 is utilized to solve the above mentioned two-dimensional ICEP model coupled with the moving mesh scheme. In addition to the electric field (Eq. (4.1)), flow field (Eqs. (4.5) and (4.6)) and the particle motion (Eqs. (4.15~4.17)), a PDE based module is used to solve the ALE formulation, Eq. (4.22) and Eq. (4.23), for the purpose of the mesh and boundary updating. The physical properties of the fluid, particle and the specifications of the microchannel used in the simulations are listed in Table 4.1.

Table 4.1 Properties used in the simulations of ICEP

Dielectric constant ε	80
Permittivity of vacuum ε_0 (C/V·m)	8.854×10^{-12}
Viscosity μ (kg/m·s)	0.9×10^{-3}
Density ρ (kg/m^3)	998
Microchannel width H (μm)	100
Particle diameter D (μm)	30
Zeta potential of channel wall (mV)	−50

4.3.2 Model benchmark

To check the feasibility of the model mentioned above, a benchmark problem is tested and the result is compared with an earlier published model (Ye & Li, 2003). The benchmark describes electrophoretic motion of a non-conducting circular particle in a T-shaped slit microchannel filled with an aqueous electrolyte solution, as shown in Figure 4.3. Both the particle and the channel surface are non-conducting and carry uniform negative zeta potentials, $\zeta_w = -25$ mV and $\zeta_p = -50$ mV respectively. The particle is initially placed at the T-shape junction region, which is also set as the computational domain. The width of the left horizontal main channel is 300 μm and the width of the vertical channel is 150 μm. The particle has a diameter of 30 μm. The other dimensions are shown in Figure 4.3. In the simulations, the particle diameter is set as the characteristic length to calculate the non-dimensional channel specifications. The applied electric potential at the inlet and the upper outlet are fixed at ϕ_1= 0 V and ϕ_2 =1 V. The applied electric potential at the lower outlet ϕ_3 takes the values of 1 V, 0.75 V, 0.5 V and 0.25 V respectively. The simulated paths of the particle moving in the junction region during a certain time are shown in Figure 4.4. It can be concluded that the particle motion is influenced by the electric potential applied at the lower outlet of the channel and the direction of the particle motion is controlled by the direction of the electric field. The results calculated from the current model match the earlier results given by Ye and Li in 2003, which proves the feasibility of the current numerical approach.

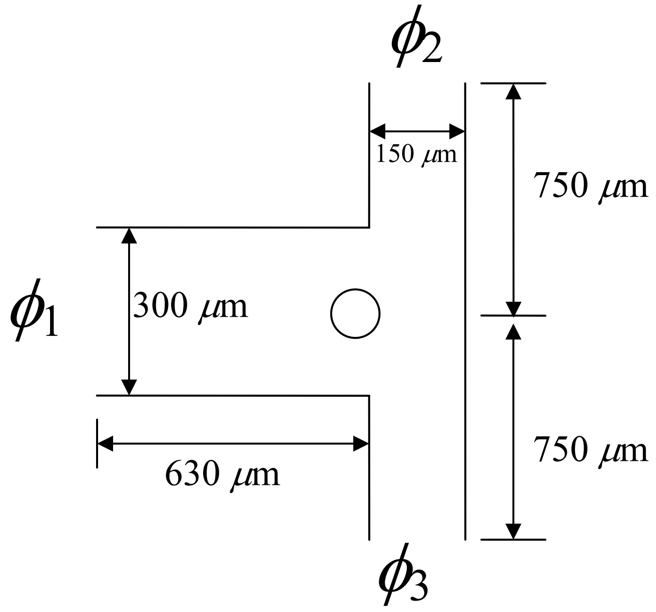

Figure 4.3 Schematic diagram of a circular particle in a T-shaped slit channel

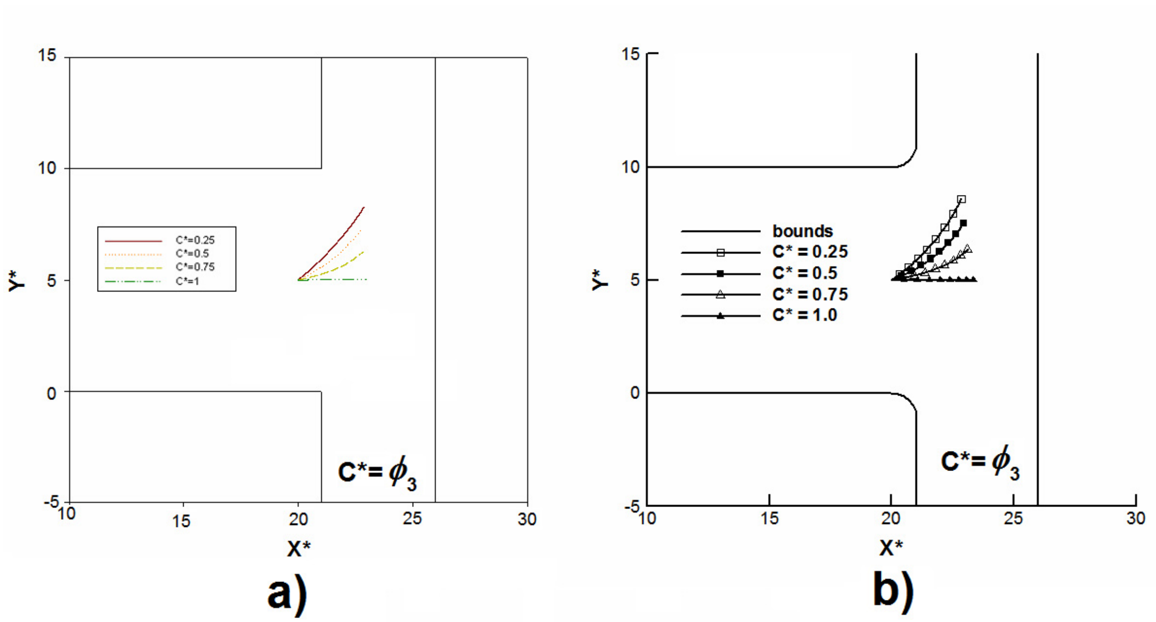

Figure 4.4 Particle trajectories calculated from (a) current model (b) Ye & Li 2003

4.3.3 Two-dimensional ICEP of conducting particles

The induced-charge electrophoretic motion of a conducting particle placed at the center line of a straight microchannel is investigated. The microchannel has a width of 100 μm and the particle has a diameter of 30 μm. The electric field strength applied through the microchannel is 100 V/cm. The zeta potential of channel wall is set as -50 mV. Figure 4.5 shows the ICEP motion of a conducting particle in the microchannel compared with the EP motion a non-conducting particle under the same conditions. The surface patterns in the figure are electric field. The contour lines correspond to the equi-potential lines. The stream lines of the flow fields are also plotted. It's clearly shown that, different from the non-conducting particles, conducting particle will induce strong micro vortexes on particle surface while it's moving in the microchannel. Thus the flow field in the microchannel is totally distorted because of the presence of the conducting particle.

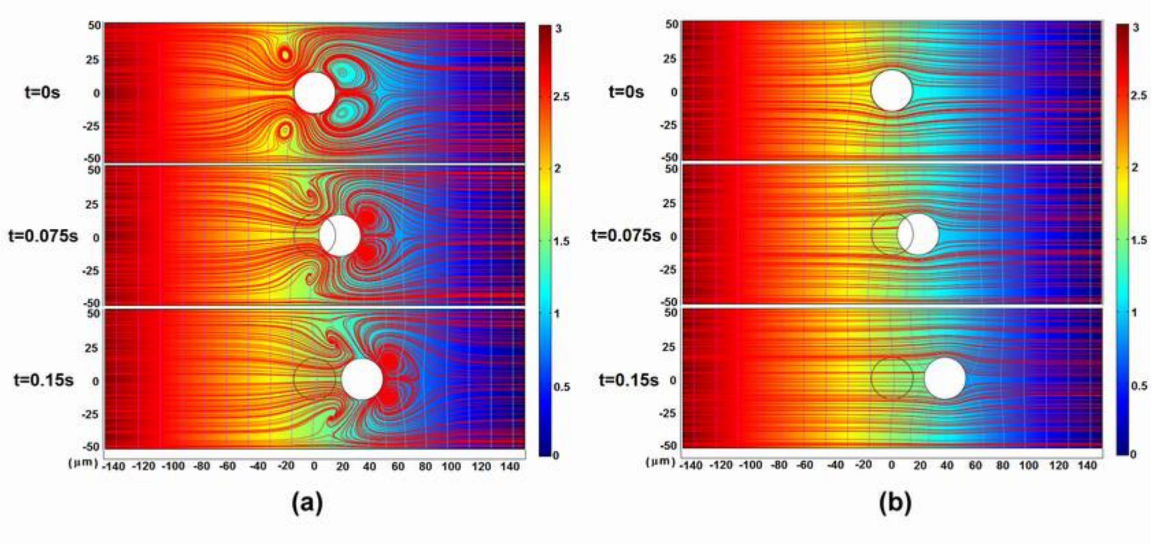

Figure 4.5 Two-dimensional electrophoretic motion of (a) a conducting particle (b) a non-conducting particle in a microchannel

To study the channel wall effect on the electrophoretic motion of particles, the particle was placed at a distance of 15 μm from the bottom channel wall. An earlier study indicated that the hydrodynamic force provides a lifting effect when a non-conducting particle is placed close to the channel wall (Ye & Li 2002). The effect is greatly strengthened when the non-conducitng particle is replaced with a conducting particle with induced micro vortexes generated on its surface. Figure 4.6 shows the ICEP and EP motions of a particle placed close to the channel wall. It's found that ICEP of conducting particle shows a much stronger lifting effect than that of non-conducting EP motion.

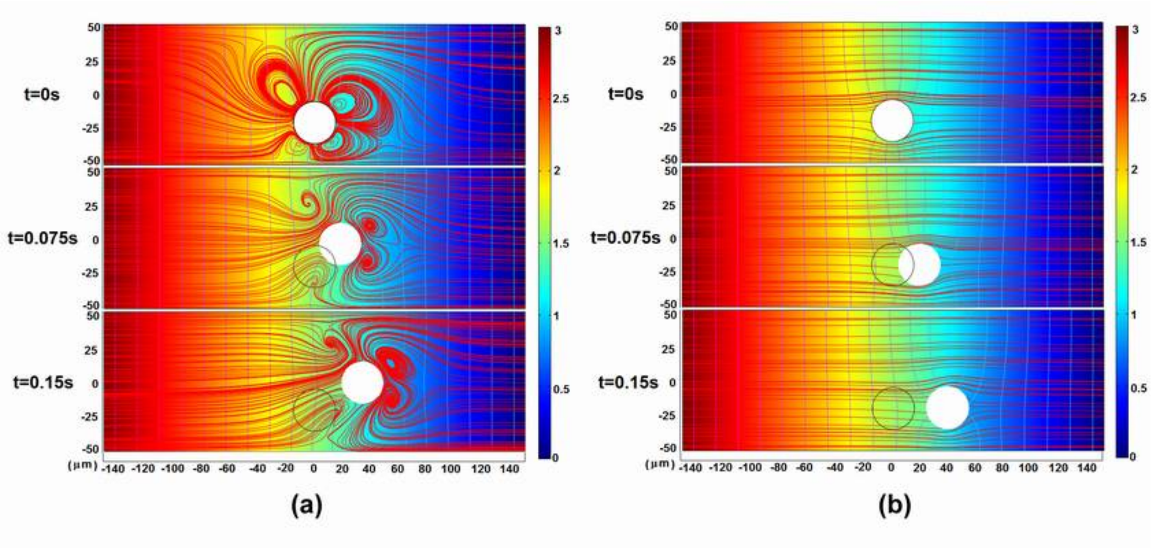

Figure 4.6 Two-dimensional electrophoretic motion of (a) a conducting particle (b) a non-conducting particle with wall effect

To study the induced-charge electrophoretic particle-particle interactions, two identical particles with diameters of 30 μm were placed in an unbounded large field with a separation distance of 100 μm. Figure 4.7 shows the motions of the particles under two different orientations of the external applied electric field. It's was found that the ICEP motion between particles is highly dependent on the directions of the external field. When the applied electric field is parallel to the placement of the particles, the resultant ICEP motion shows an attracting effect between the particles and the separation distance is decreasing with time, as shown in Figure 4.7a. However, if the two particles are placed vertically to the applied electric field, the particles tend to repel each other and the distance between the particles increase with time, as shown in 4.7b.

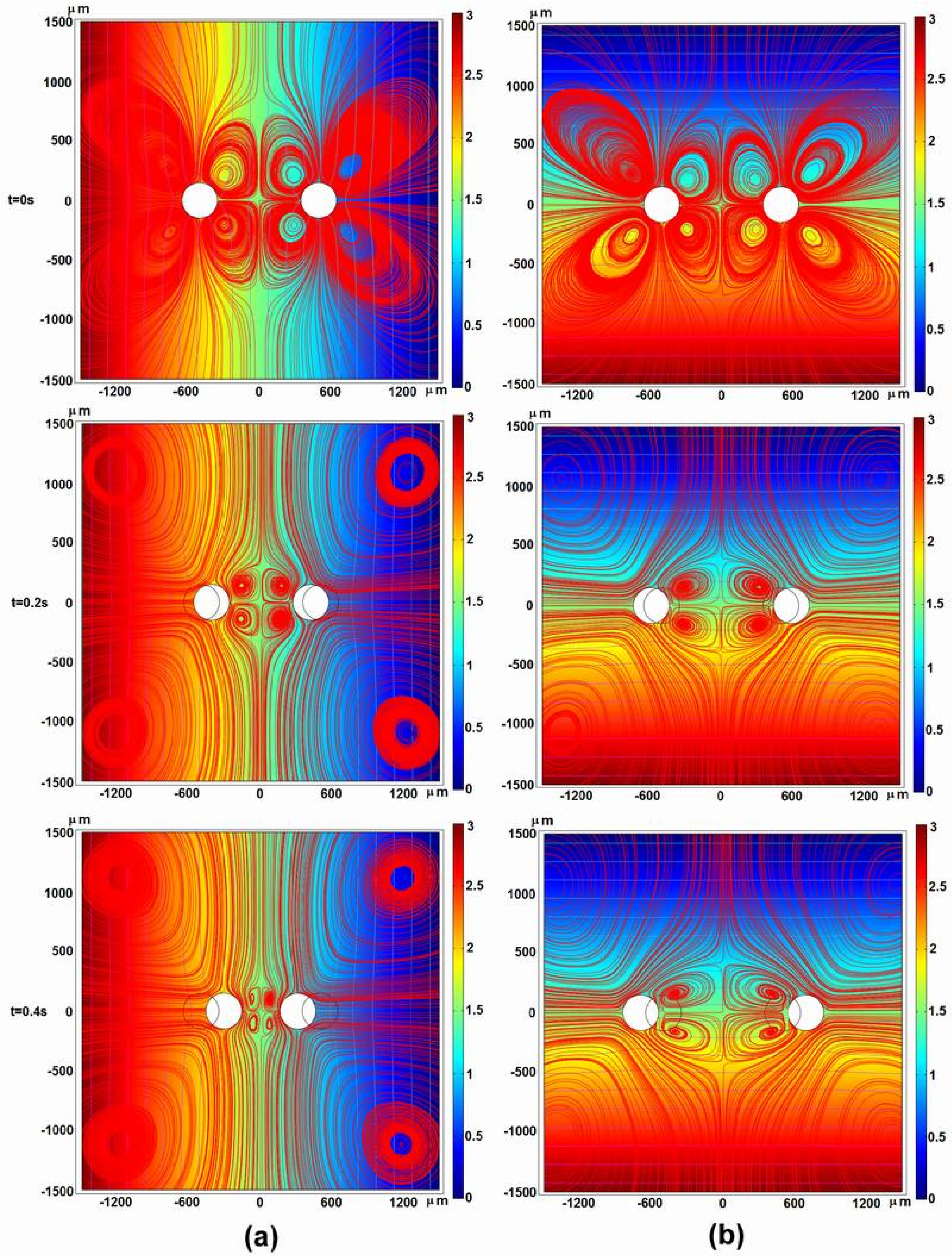

Figure 4.7 Particle-particle interactions with (a) parallel applied electric field and (b) vertical applied electric field

4.4 Three-dimensional numerical simulation of ICEP

Although the 2-D model developed above provides qualitatively predictable results, real particles are all in three dimensional and the complete 3-D model is necessary. Figure 4.8 illustrates a 3-dimensional particle-channel system. The microchannel with the dimensions of $H \times W \times L$ is placed horizontally and filled with an aqueous electrolyte solution. The ends of the channel are connected to open reservoirs, so that no overall pressure gradient is present in the system. The channel walls carry uniform negative electric charges that are characterized by the zeta potential ζ_w. The particle, with a diameter of d, is perfectly polarizable. An external electric field E_0 is applied uniformly along the channel. The particle and the channel walls are rigid and the aqueous electrolyte solution is Newtonian and incompressible.

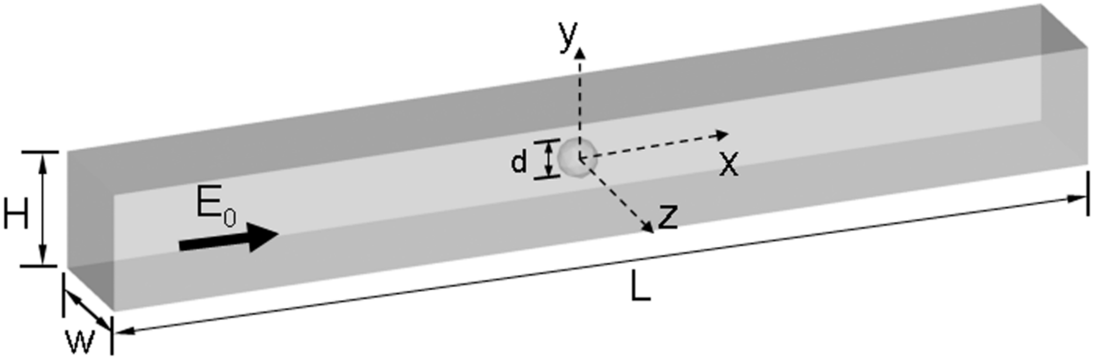

Figure 4.8 Schematics of a 3-D particle-channel system

The COMSOL® software utilized in Section 4.3 has two limitations in 3D modeling. Firstly, it has clear reported memory efficiency problem with large mesh system in most of 3D transient problems. Secondly, to keep the correct mesh topology in 3D modeling, the ALE moving grid technique mentioned earlier requires frequent re-meshing to fulfill long distance object motion, which is not supported in COMSOL® software. As an alternative, FLUENT® software provides built-in dynamic re-meshing macros using its preset User Defined Functions (UDF), which can be utilized for the efficient simulation of 3-D moving boundary problems. Thus, FLUENT® replaces the COMSOL® package to fulfill the 3D ICEP simulation using the same theoretical model developed in Section 4.2. A non-uniform spaced grid system was produced using GAMBIT for more accurate solutions. The total number of elements used in the computation was 137,268.

4.4.1 3-D micro-vortex generation

As mentioned earlier, when the polarizable particle is immersed and fully polarized in the applied electric field, the particle behaves like an insulator because an induced dipolar double layer on the particle surface. Then, a steady-state electric field is established, as illustrated in Figure 4.9

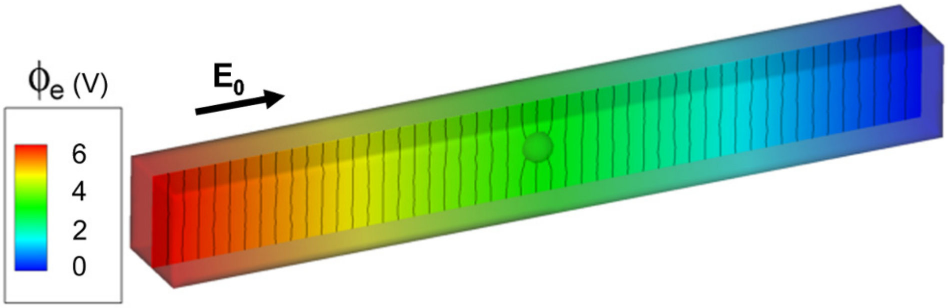

4.9 Steady state electric field in a particle-channel system (d=30 μm, W=H=150 μm, L=0.6 mm, E_0=100 V/cm). The color indicates the strength of the electric field; the lines are the equal potential lines.

Once the dipolar induced double layer is formed, a non-uniform zeta potential distribution will be induced on the conducting surfaces, causing a varying driving force of the electroosmotic flow. Consequently, the slipping velocity on the conducting surfaces changes with position, resulting in a non-uniform flow field. Figure 4.10 shows the typical steady state flow fields in the particle-channel system with applied electric field strengths of 100 V/cm, 70 V/cm and 40 V/cm respectively. Figure 4.10a shows the 3-D flow stream patterns with the representative stream lines plotted in the microchannel and Figure 4.10b shows the flow vectors near the polarizable particle's surface on the plane at $z = 0$. To study the pure induced-charge effects, we assume the particle is initially electric neutral, i.e., no initial zeta potential on the particle surface is considered. As we can see in the figure, the streamlines of the liquid flow near the particle surface is distorted and micro vortexes are generated because of the non-uniform induced charge distribution on the polarizable particle's surface. The flow pattern clearly depends on the electric field. Under relatively higher electric field, the induced zeta potential on the conducting surface is stronger and vortexes with relatively larger sizes are generated at both upstream and downstream sides of the particle. The mainstream EOF in the channel is not strong enough to break this structure. Under lower electric field, the induced zeta potential on the particle's surface is weaker, resulting in smaller vortexes. The EOF generated from the non-conducting channel wall will affect the flow field near the particle. Under low applied electric fields, the flow circulations at the upstream side are swept off by the main stream flow in the channel and only vortexes at the downstream side are retained.

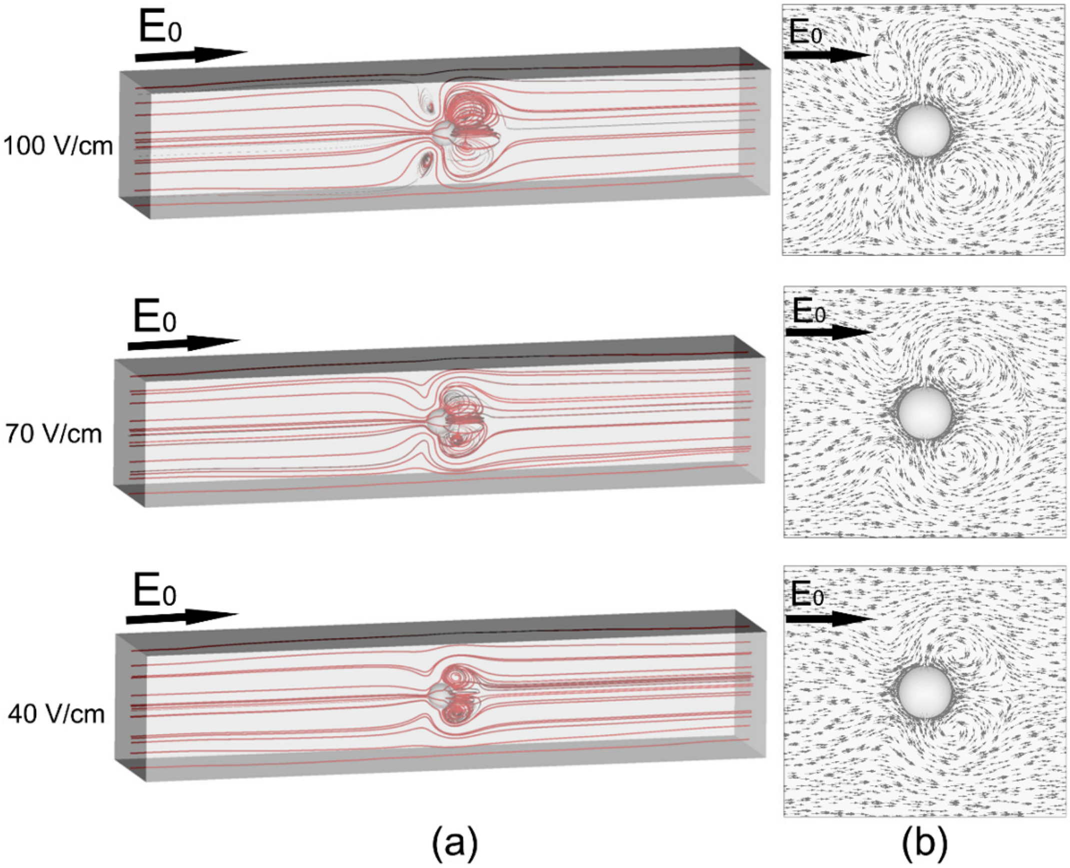

4.10 Steady state flow fields in the particle-channel system with different applied electric field strengths: (a) 3-D flow stream patterns (b) flow vectors near the polarizable conducting particle's surface at the *z* = 0 plane (*d*=30 μm, *W*=*H*=150 μm, *L*=0.8 mm).

4.4.2 Transient ICEP motion of 3-D conducting particles along the center of a microchannel

The induced-charge electrophoretic motion of an ideally polarizable conducting spherical placed at the center line of a straight microchannel was investigated. The microchannel's width and height are both 150 μm and the length of the channel is 0.8 mm. The particle has a diameter of 30 µm and is initially placed at the origin point (0,0,0) at the center of the channel. The electric field strength applied through the microchannel is set as 100 V/cm. The initial uniform zeta potential on the particle surface is set as −15 mV. The density of the particle is set as the same as that of the fluid, so that no gravity force on the particle is considered in this case. Clearly, the system is symmetrical to the $z = 0$ plane. Figure 4.11 shows the ICEP motion of an ideally polarizable particle in the microchannel compared with the EP motion a non-conducting particle with the same static uniform zeta potential of −15 mV, under the same conditions. The stream lines of the flow field are plotted. The figures only show the right half branch of the channel, where the particle's motion takes place. It's clearly shown that, different from the non-conducting particle, polarizable particle will induce strong micro vortexes near the particle surface while it's moving in the microchannel. Figure 4.12 shows the developing velocities of EP motion and ICEP motion, respectively. It's found that for both EP and ICEP motions, there is a short period of transient particle acceleration. After that, both the polarizable and non-conducting particles reach a steady motion with an equal constant velocity. This is because the average induced zeta potential over the polarizable particle's surface (Eq. (2.13)) is zero, leading to a zero contribution to the electrokinetic driving force on the particle. This is consistent with the well known conclusion made by O'Brien and White (1978) that the electrophoretic mobility is independent on electrostatic boundary conditions.

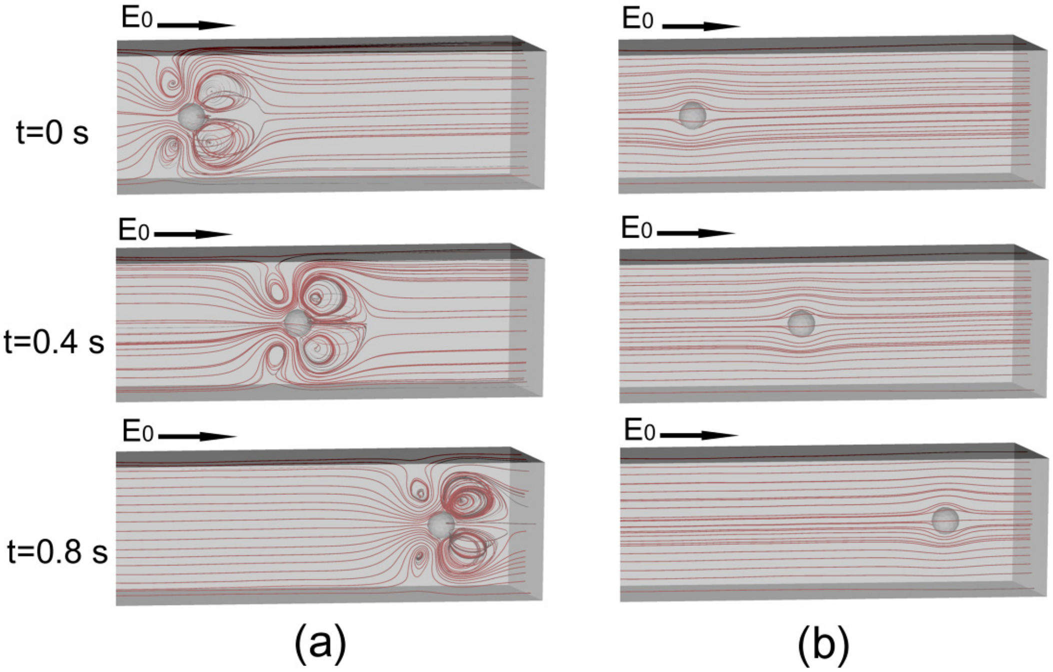

4.11 Three-dimensional electrophoretic motion of (a) an ideally polarizable particle (b) a non-conducting particle in a microchannel (d=30 μm, W=H=150 μm, L=0.8 mm, E_0=100 V/cm)

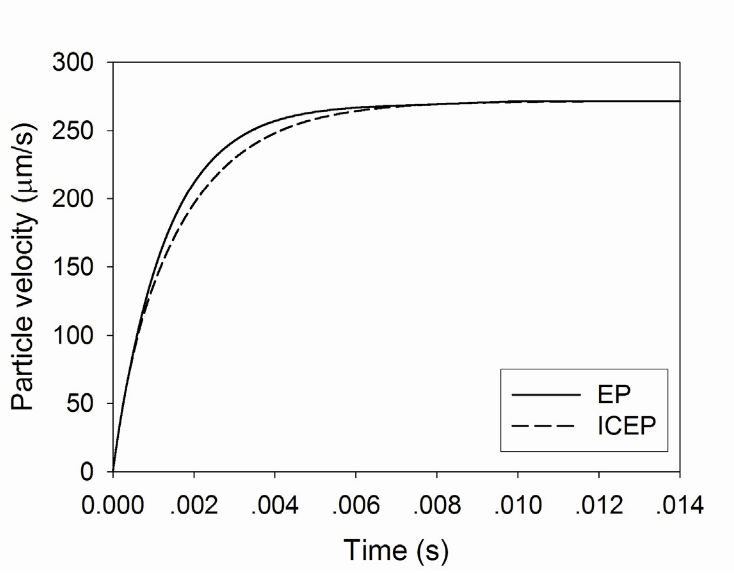

4.12 Developing particle velocities of EP and ICEP (d=30 μm, W=H=150 μm, L=0.8 mm, E_0=100 V/cm)

4.4.3 Wall effects on ICEP motion

Same as Section 4.3, to study the channel wall effects on the electrophoretic motion of particles, a spherical particle of 30 μm in diameter was placed at a distance of 15 μm (half diameter of the particle) from the bottom channel wall. To investigate the pure induced-charge effects, we do not consider any initial zeta potential on the particle surface. The simulation shows significant lifting effect that brings the polarizable particle from the region near the wall to the center of the channel. Figure 4.13 shows the ICEP and EP motions of a particle initially placed close to the channel wall. As mentioned earlier, the system is symmetrical to the $z = 0$ plane. We present the corresponding particle trajectories (based on the particle center) in the x-y plane, as shown in Figure 4.14. Due to the unbalanced interaction of the vortices with the channel wall, there is a net lifting force acting on the particle. ICEP motion of a polarizable particle shows a strong lifting effect and a clear tendency of retuning to the channel center. This is because the lifting force on the particle only vanishes when the particle is moving along the channel center line. Figure 4.15 plots out the non-dimensional lifting force, $\bar{F}_{\text{lift}} = \bar{F}_{net,y} = \dfrac{F_{net,y} \cdot \mu^2}{\rho\left(\varepsilon\varepsilon_0\zeta^2{}_w\right)^2}$, exerted on the polarizable particle with the different particle positions in the microchannel, where $\vec{F}_{net}$ is the net force on the particle defined in Eq. (4.12). As we can see in the figure, if the particle is close to the bottom wall, a positive lifting force is obtained, which will bring the particle into upward motion. If the particle is close to the upper wall, a negative force is shown and this pushes the particle downward. Thus, the steady level of the particle motion in the channel must be the channel center. Strictly speaking, if the particle is placed extremely close to the channel wall, the electric field between the particle and the channel wall will be highly distorted and dielectrophoretic (DEP) force will provide additional lifting on the particle. However, the DEP force may be effective only during a very short initial period (milliseconds) when the particle is close to bottom wall. The induced vortices will immediately lift the particles from the wall; and thereafter the gap between the particle and the wall is sufficiently large (e.g., the size of the vortices, see Figure 4.13) so that non-uniformity of the electric field around the particles is sufficiently small and the DEP effect is negligible. In other words, the lifting effect caused by the vortices is dominant and has much large effective distance. Furthermore, in this study, the particle is initially placed sufficiently far from the bottom channel wall to keep the uniformity of the electric field, thus no DEP effects are considered. It should be also mentioned here that, in this case, the density of the particle is set as the same as that of the liquid and no gravity force is considered. If the particle is subject to any additional body force, the final level of the particle motion will be different from the channel center, which will be discussed later.

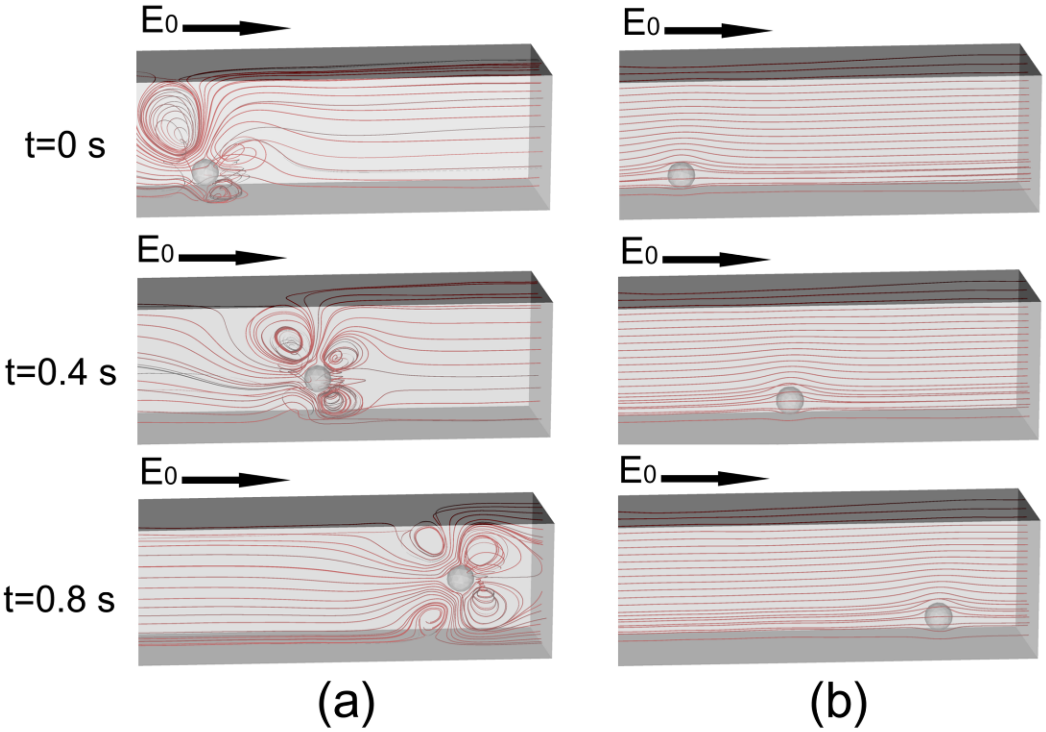

4.13 Wall effects on electrophoretic motions of (a) an ideally polarizable particle (b) a non-conducting particle (*d*=30 μm, *W*=*H*=150 μm, *L*=0.8 mm, E_0=100 V/cm)

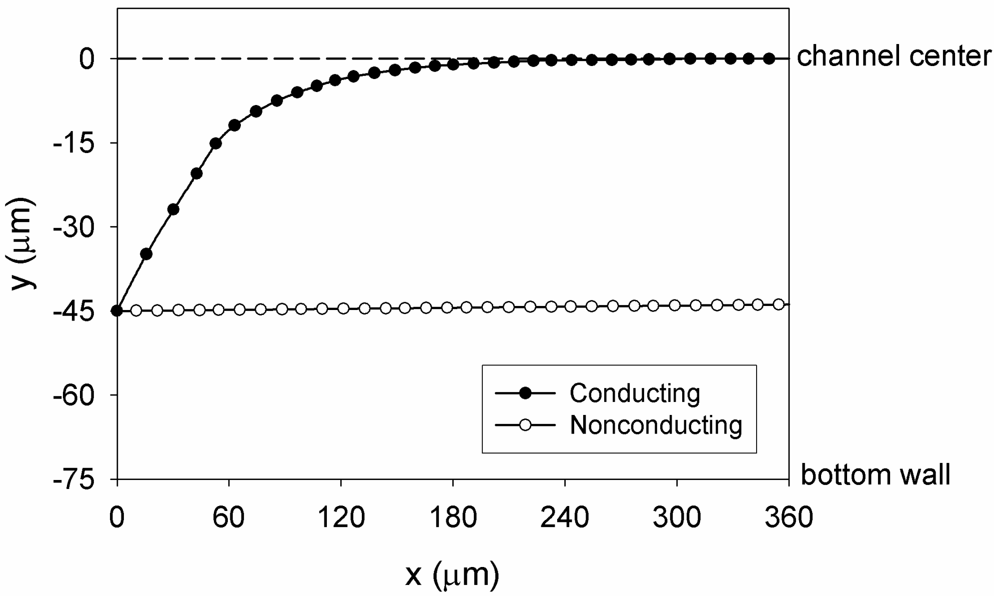

4.14 Particle trajectories of EP and ICEP motion with wall effects (*d*=30 μm, *W*=*H*=150 μm, *L*=0.8 mm, E_0=100 V/cm)

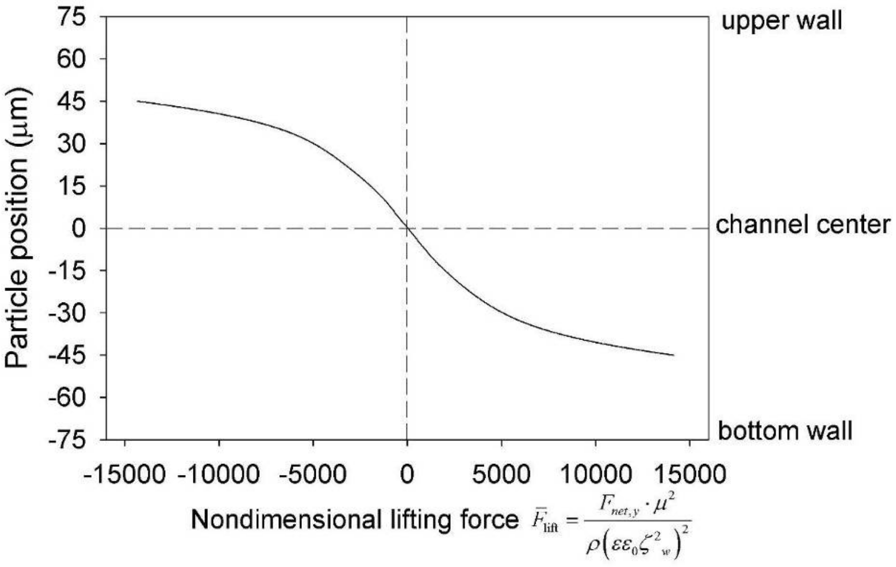

4.15 Lifting force on the ideally polarizable particle (d=30 μm, W=H=150 μm, L=0.3 mm, E_0=100 V/cm)

The following will further investigate the influence of the electric field strength and the particle size on the lifting effect of ICEP motion. Figure 4.16 shows the ICEP trajectories under different electric field strengths. The particle has a diameter of 30 μm and the width and height of the channel are both 150 μm. The particle is initially placed at (0, -52.5μm, 0), corresponding to a distance of 7.5 μm to the bottom wall. It is clearly shown in the figure that larger electric field will give stronger lifting effect on polarizable particle's ICEP motion. The particle returns to the channel center in a shorter period of time under a stronger applied field. This is because higher electric field strength gives stronger induced electrokinetic vortexes near the polarizable particle's surface, leading to higher lifting force.

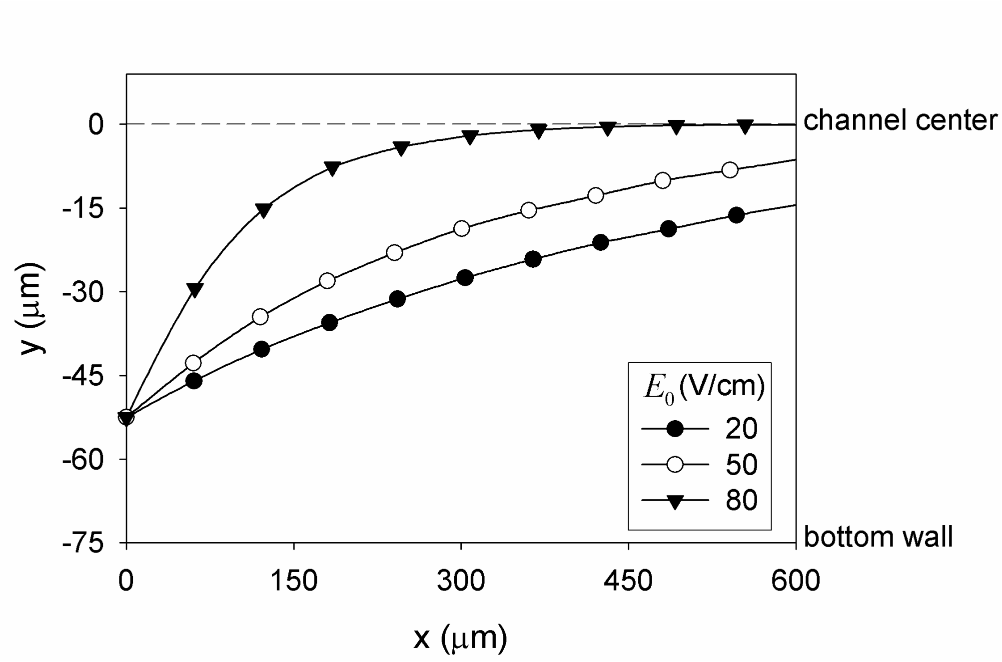

4.16 ICEP particle trajectories under different applied electric field strengths (*d*=30 μm, *W*=*H*=150 μm, *L*=0.8 mm)

The lifting effect also depends on the particle size. Figure 4.17 shows the ICEP trajectories with different particle sizes under the same applied electric field. The diameters of the particle are 10 μm, 20 μm and 40 μm respectively. The width and height of the channel are both 150 μm. The applied field strength is 100 V/cm. The particle is initially placed at (0, −45 μm, 0). Clearly, larger particle shows stronger climbing effect although all the particles have the same trend of returning to the channel center.

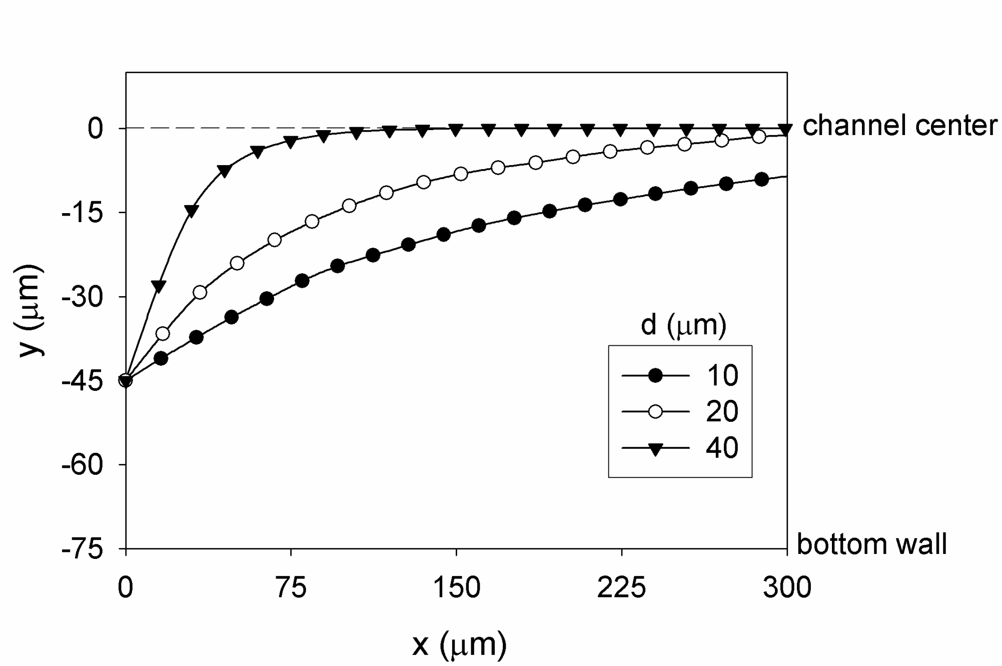

4.17 ICEP trajectories with different particle sizes (*W*=*H*=150 μm, *L*=0.8 mm, E_0=100 V/cm)

As discussed above, the induced-charge electrophoretic motion of ideally polarizable particles in a microchannel show a clear wall-repelling effect when the particle is moving close to the channel wall. This is due to the interaction between the induced electrokinetic micro vortexes near the particle's surface and the channel wall. The steady level of the particle motion in the channel is the channel center line. Thus, it can be predicted that, no matter where the polarizable particle is initially placed, the particle will finally move along the channel centerline. Figure 4.18 shows the particle trajectories in the microchannel with different initial positions. The particle's diameter is 30 μm. The channel's dimension is 150 μm×150 μm×0.8 mm. The applied electric field is 100 V/cm. As we can see in the figure, although the particles were released at different locations, the trajectories are finally focused to the channel centerline. This is useful in the applications that require particle focusing process such as microfluidic flow cytometer. The wall-repelling effect of the induced-charge electrokinetic motion of the ideally polarizable particles provides an automatic focusing mechanism with easy operations, without need of any additional adjustments of the electric field or complex channel design.

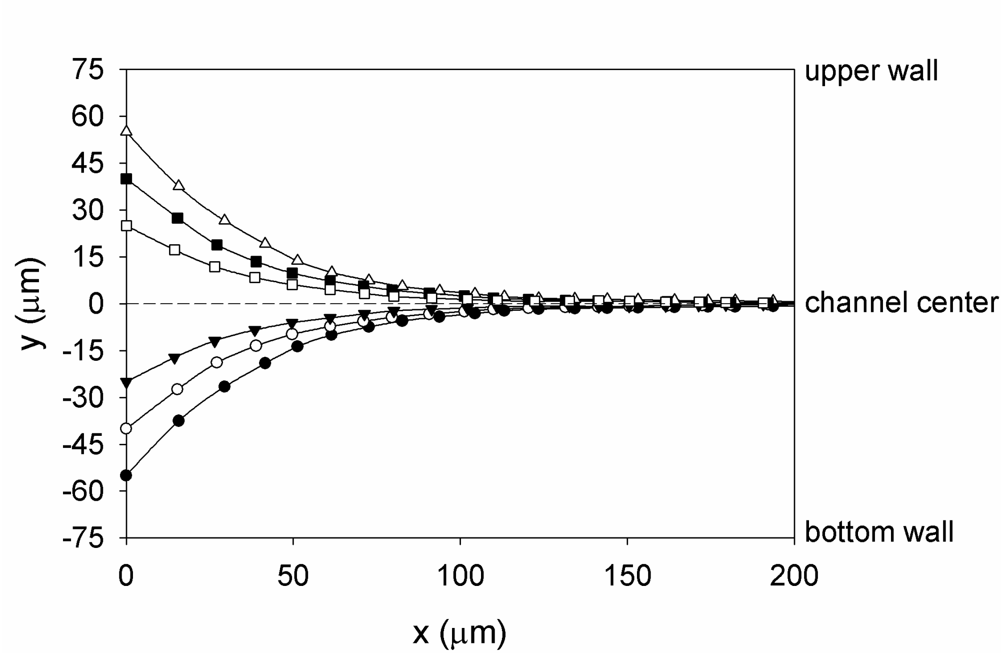

4.18 ICEP particle trajectories with different initial particle locations (*d*=30 μm, *W*=*H*=150 μm, *L*=0.8 mm, E_0=100 V/cm)

So far, the additional body force on the particle resulted from gravity and buoyancy is assumed to be zero by the assumption that the particle's density is the same as that of the liquid. However, this is not always the case and the particle's density will definitely affect the trajectory of the particle motion. Figure 4.19 shows the density effects on the particle's ICEP motion. The particle has a diameter of 10 μm. The applied electric field strength is 150 V/cm. The particles densities are set as 0.5ρ, 1.0 ρ and 1.5 ρ respectively, where ρ is the density of the liquid. As we can see in the figure, when the particle's density is the same as the liquid, the particle will finally move along the channel centerline, just as mentioned earlier. However, if the particle's density is larger than that of the liquid, a gravity force in y direction will be exerted on the particle. To balance this body force, a positive lifting force is needed, which corresponds to a lower lever of the particle motion close to the bottom channel wall. If the particle's density is smaller than that of the liquid, the opposite effect applies and the particle will finally move at a higher level close to the upper wall. Thus, a particle separation by density can be obtained. As we can see in the figure, a 50% density difference approximately results in a separation distance of around 30 μm, which is about 3 times of the particle's diameter. It can be expected that the separation effect will be further strengthen if we increase the density difference between particles.

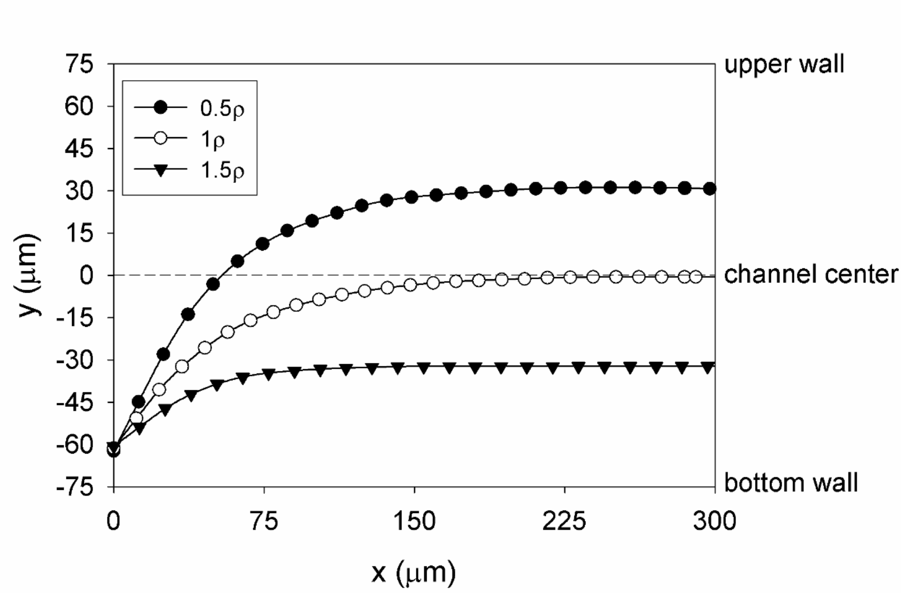

4.19 ICEP trajectories with different particle densities (*d*=10 μm, *W*=*H*=150 μm, *L*=0.8 mm, E_0=150 V/cm)

4.4.4 Particle-particle interactions

Same as in Section 4.3.3, to study the induced-charge electrophoretic particle-particle interactions, two identical spherical particles with diameters of 30 μm were placed in an unbounded large field with an initial separation distance of 150 μm. To study the pure induced-charge effects, we assume the particles are initially electric neutral. Figure 4.20 shows the motion of the particles under an external electric field parallelly applied to the orientation of the two particles with the representative stream lines plotted. It's clearly shown that ICEP motion shows an attracting effect between the particles under a parallel applied field. We label the particle on the left as P1 and the particle on the right as P2. Figure 4.21 shows the developing velocities of the two particles and the separation distance varying with time. As we can see in the figure 4.21a, particle P1 shows positive velocity while particle P2 shows negative velocity, giving a decreasing separation distance (*D*) between the two particles, as shown in Figure 4.21b. This is consistent to the 2D predictions made in Section 4.3.3.

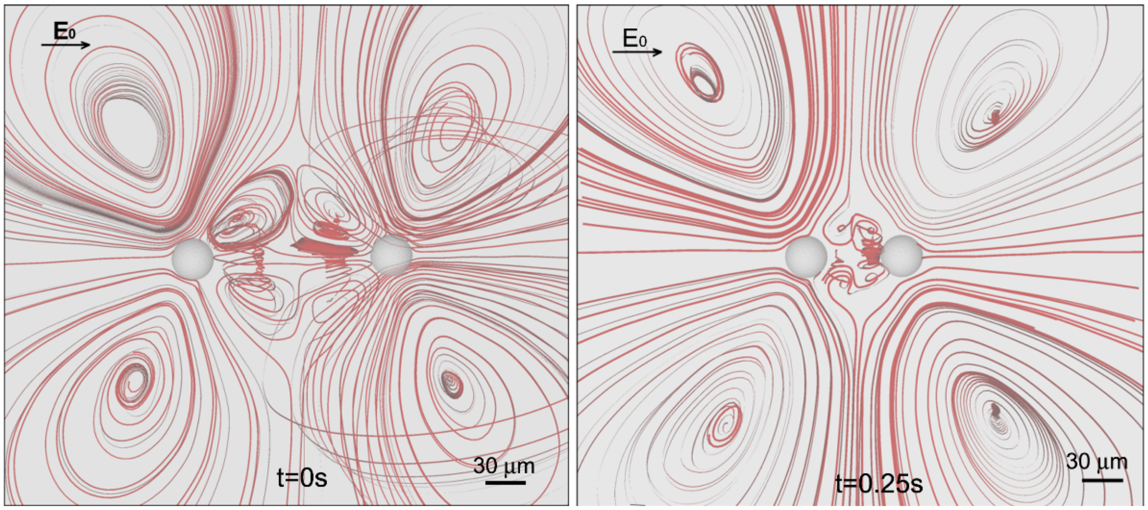

Figure 4.20 Particle-particle interactions with parallel applied electric field (E_0=100 V/cm, d=30 μm)

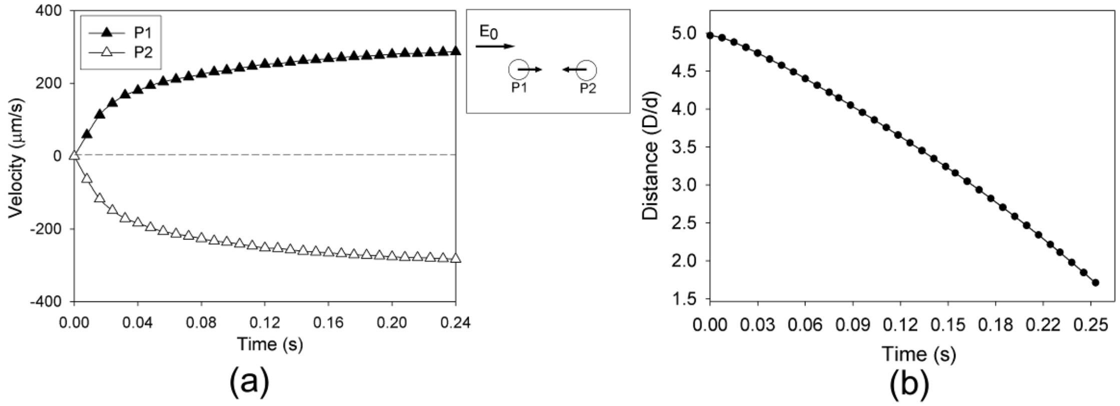

(a)

(b)

Figure 4.21 a) Particle velocities and b) separation distance under a parallel applied electric field (E_0=100 V/cm, d=30 μm)

To investigate the reason giving the particle-particle attracting under a parallel electric field, we plot out the flow vectors and the corresponding pressure distribution near the particles on the plane at z = 0, as shown in Figure 4.22. It's found that, under a parallel electric field, the micro vortexes generated on the particle surfaces are non-symmetric when the particles are close to each other. Also, the vortexes between the two particles show clear inward rotations (see Figure 4.22a). This gives an induced pressure distribution and a lower pressure zone is found between the two particles, as shown in Figure 4.22b. Thus, the two particles are pushed to get closer. This effect also depends on the distance between the two particles. Figure 4.23 shows the nondimensional attracting forces, $\bar{F} = \bar{F}_{net,y} = \dfrac{F_{net,y} \cdot \mu^2}{\rho\left(\varepsilon\varepsilon_0 \zeta^2_{\mathrm{ref}}\right)^2}$, exerted on the particles with different separation distances. It's clear that particle P1 experience positive force while particle P2 experience negative force, giving the inward motion of the two particles. The forces decrease with the separation distance quickly. If the two particles are separated by more than 8 diameters, the forces on the particles vanish, as shown in Figure 4.23. This means the particles will not feel the existence of the other particle if they are placed sufficient far away from each other and the forces exerted on the particles will be basically balanced.

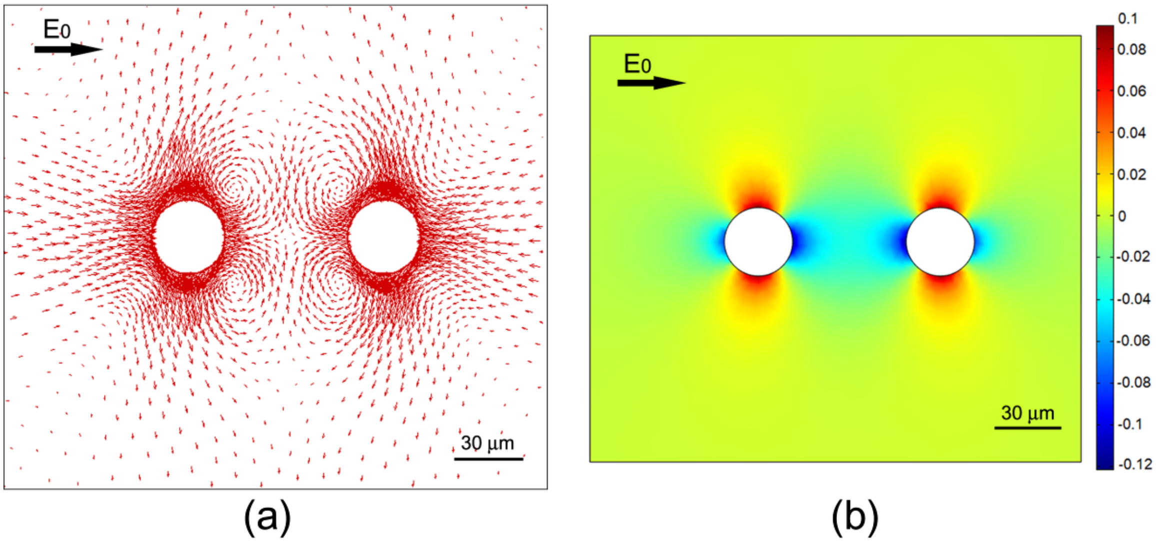

Figure 4.22 a) Inward micro vortexes and b) induced pressure distribution between two polarizable conducting particles under a parallel applied electric field (E_0=100 V/cm, d=30 μm)

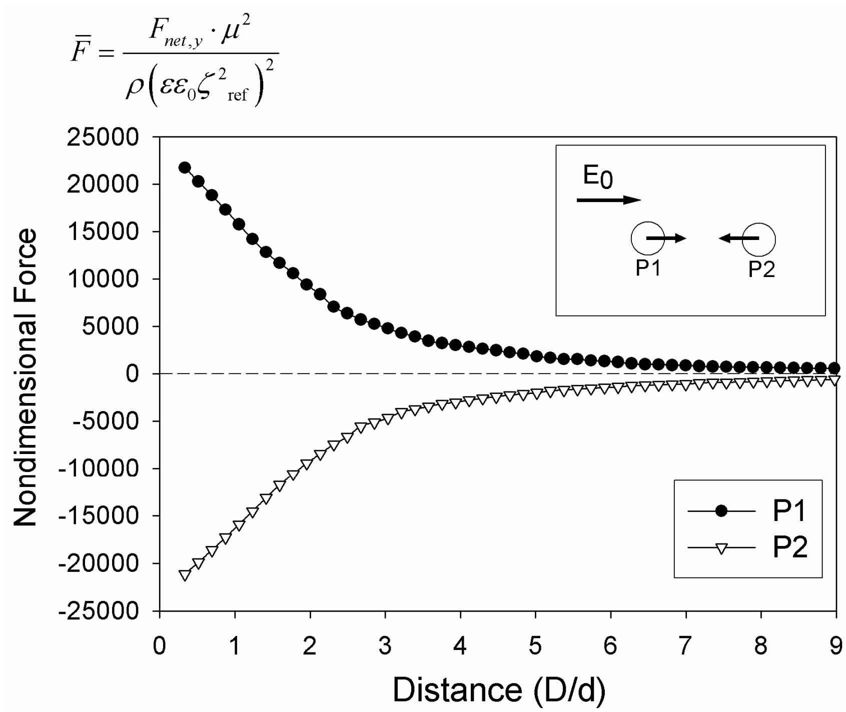

4.23 Attracting forces on the polarizable conducting particles under a parallel applied electric field (E_0=100 V/cm, d=30 μm)

The following will change the electric field orientation from parallel to vertical. Figure 4.24 shows the corresponding motions of the particles. Opposite to the parallel case discussed above, the particles show a clear repelling effect under a vertical field. Figure 4.25 shows the corresponding particle velocities and the separation distance varying with time. As shown in figure 4.25a, particle P1 shows negative velocity while particle P2 shows positive velocity, giving an increasing separation distance, as shown in Figure 4.25b.

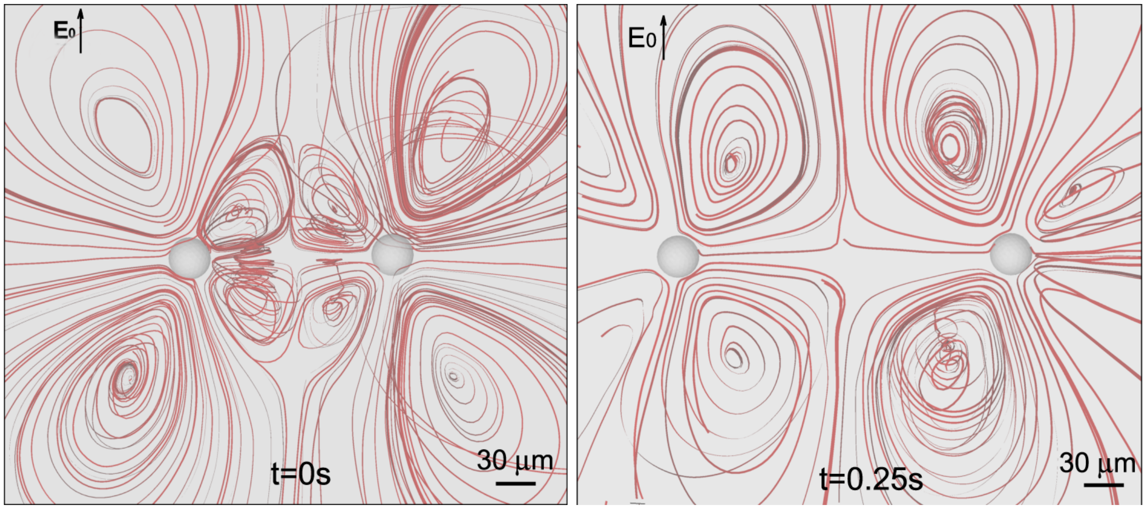

Figure 4.24 Particle-particle interactions with vertical applied electric field (E_0=100 V/cm, d=30 μm)

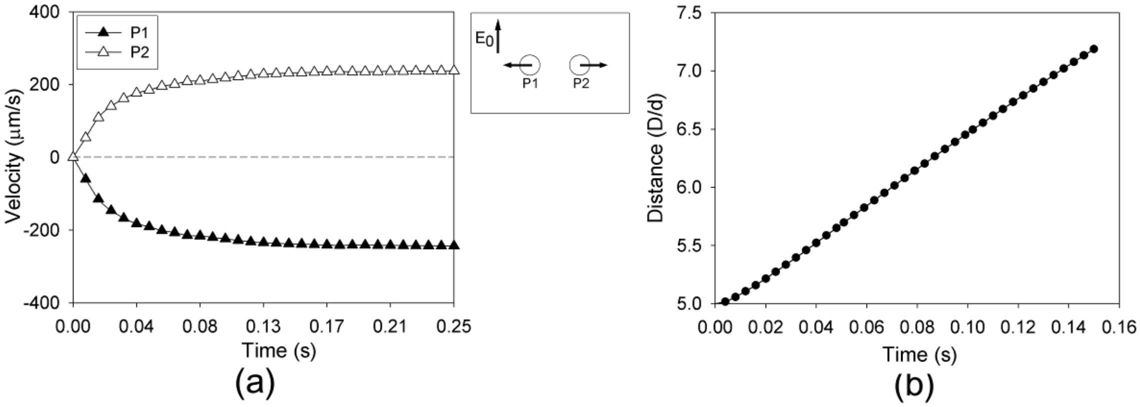

Figure 4.25 a) Particle velocities and b) separation distance under a vertical applied electric field (E_0=100 V/cm, d=30 μm)

Again, we plot out the flow vectors and the corresponding pressure distribution near the particles on the plane at z = 0, as shown in Figure 4.26. In this case, the vortexes between the two particles show clear outward rotations, giving an induced pressure distribution with a higher pressure zone generated between the two particles, as shown in Figure 4.26b. Thus, the two particles are repelled from each other. Figure 4.27 shows the nondimensional repelling forces exerted on the particles with different separation distances. It’s clear that particle P1 experience negative force while particle P2 experience positive force, giving the outward motion of the two particles. Again, the particles will not affect each other if they are separated more than 8 diameters, given the balanced forces.

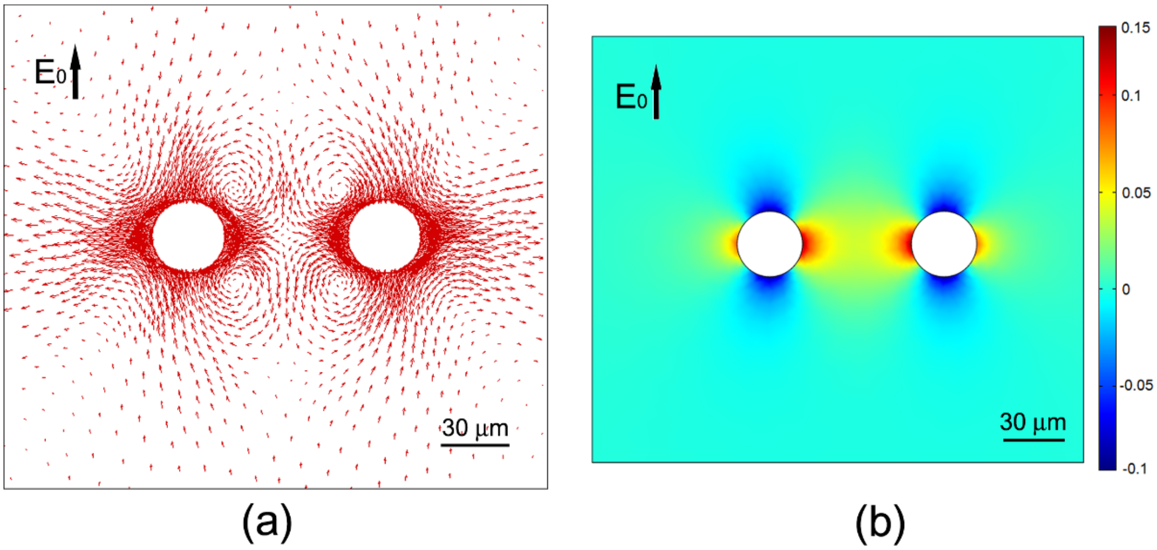

Figure 4.26 a) Outward micro vortexes and b) induced pressure distribution between two polarizable conducting particles under a vertical applied electric field (E_0=100 V/cm, d=30 μm)

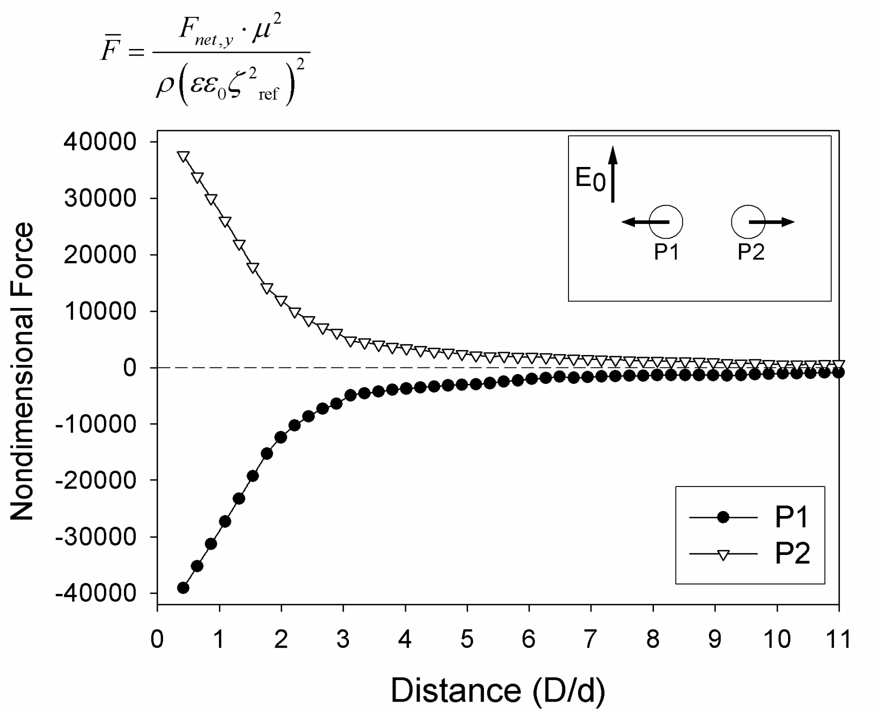

4.27 Repelling forces on the polarizable conducting particles under a vertical applied electric field (E_0=100 V/cm, d=30 μm)

Figure 4.28 and Figure 4.29 further study the influences of the electric field strength and the particle size on the ICEP particle-particle interactions. Figure 4.24 shows the developing particle velocities under electric strengths of 50 V/cm, 100 V/cm and 150 V/cm respectively. Same as discussed earlier, the parallel electric field gives an attracting effect between the two particles (Figure 4.24a) while the vertical electric field gives a repelling effect (Figure 4.24b). Further, higher electric field gives higher particle velocities, corresponding to stronger attracting or repelling effects. This is because higher electric field strength gives stronger induced electrokinetic vortexes near the polarizable particle's surfaces, leading to higher attracting or repelling forces.

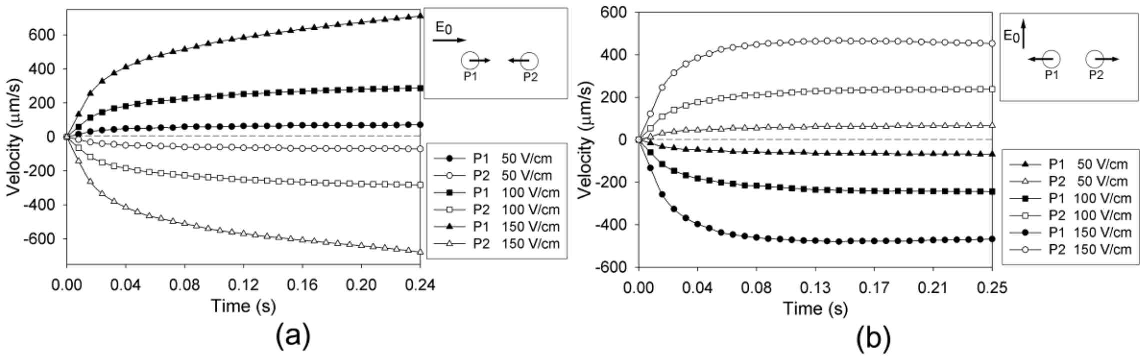

4.28 Electric strength effects on ICEP particle-particle interactions: a) particle velocities under a parallel electric field and b) particle velocities under a vertical applied electric field (*d*=30 μm)

To study the particle size effects, we fixed the size of the left particle P1 and changed the diameter of the right particle P2 by different diameter ratios, $\alpha = \frac{d_{\mathrm{P2}}}{d_{P1}}$=1/3, 1/2 and 1 respectively. Figure 4.29 shows the corresponding particle velocities under a parallel or a vertical electric field. As is shown in the figure, when the two particles have same sizes, the two particles' velocities show same magnitude but in opposite directions, giving attracting or repelling effects as discussed earlier. This is because the two particles generate micro vortexes with same sizes and strengths, giving same induced-charge electrokinetic driving forces to each other. However, when one of the particle decreases its size, the particle with the bigger fixed size (particle P1) will experience significant velocity drop while the smaller particle (P2) keeps moving almost with the same speed. This is because the smaller particle (P2) gives smaller driving force to particle P1 since it generates weaker vortexes, but particle P2 itself experience the same force since particle P1 does not change size. Thus we can conclude that the particle's velocity only depends on the other particle's size in this case. Extremely, we can predict that, if particle P2 has a negligibly small size compared to that of particle P1, the bigger particle (P1) will just look like a huge solid wall to the smaller particle (P2), thus particle P1 will not move at all and particle P2 will be attracted to or repelled from particle P1 with same speed, depending on the orientations of the applied electric field.

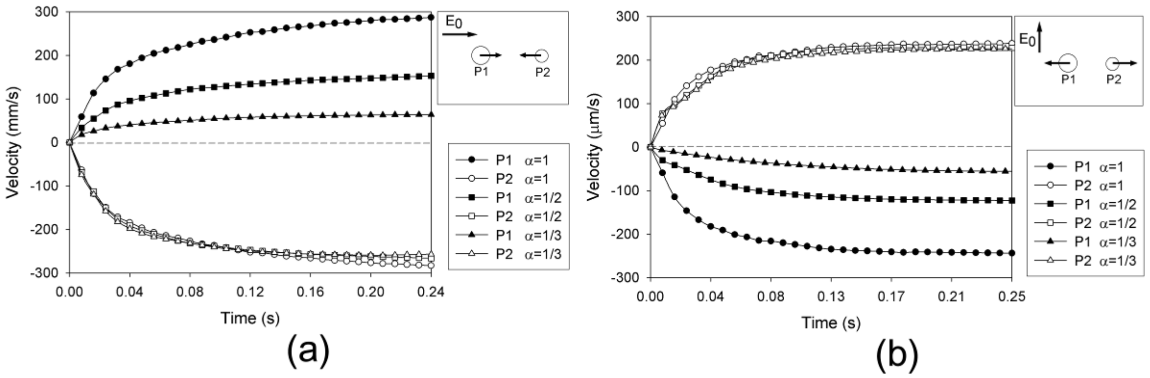

4.29 Particle size effects on ICEP particle-particle interactions: a) particle velocities under a parallel electric field and b) particle velocities under a vertical applied electric field (E_0=100 V/cm)

4.5 Summary

A complete theoretical model of induced-charge electrophoretic motion of conducting particles is established in this chapter. A numerical approach based on Arbitrary Lagrangian-Eulerian (ALE) moving mesh technique is proposed to simulate the coupled particle-liquid multi-physics system. The numerical scheme was validated by a bench mark model of particle electrophoretic (EP) motion in a T-shaped slit microchannel. The 2D and 3D induced-charge electrophoretic (ICEP) motions of conducting particles in a straight microchannel and ICEP particle-particle interactions in an unbounded large field were successfully simulated.

The numerical simulations indicate that an induced non-uniform zeta potential distribution on the conducting surface causes varying electroosmotic flow velocity on the polarizable particle's surface and circulating flows near the particle. It's numerically proven that, although the ICEP motion of an ideally polarizable conducting particle has a very different flow field from that of the EP motion of a non-conducting particle, the electrophoretic velocity is the same for the two cases under the assumption that the particles have the same initial zeta potential. It's also found that ICEP motion of ideally polarizable particles has a very strong wall-repelling effect when the particle is moving close to the channel wall, due to the interaction of the vortices around the particle and the channel walls. The effect depends on the electric field and the particle size. Higher electric field and larger particle size both give stronger wall-repelling. The polarizable particles show a clear trend of returning to the channel's centerline under the assumption that the particles have the same density as that of the liquid, making particle auto focusing possible. Particle's density will also affect its final steady level of the ICEP motion in the microchannel. This provides a potentially effective way for particle separation by density.

ICEP particle-particle interactions in an unbounded large field were also studied. The simulations show that an attracting effect can be obtained between the two polarizable conducting particles under a parallel applied field about the orientation of the two particles while a repelling effect is found under a vertical applied electric field. This is basically because of the non-symmetric micro vortexes generated between the two particles when they are placed close to each other. Under a parallel electric field, the micro vortexes are inward rotating, inducing a low pressure zone between the two particles, pushing the particles to get closer. Oppositely, under a vertical electric field, the vortexes are outward rotating, inducing a high pressure zone between the two particles, driving the particles to repel each other. The ICEP attracting or repelling effects depend on the particles' separation distance. When the particles are placed sufficient far away from each other with a separation distance greater than a critical value, the particles will not feel the existence of the others and the driving forces on the particles are balanced, thus the ICEP interacting effects will basically vanish. The effects also depend on the electric field strength and the particle size. Higher electric field strength gives stronger attracting or repelling effects between the two particles. Also, the particle's velocity only depends on the other particle's size. Smaller particle gives smaller driving force to others, but the speed of itself will not be affected if the other particle does fix the size.

The simulations of induced-charge electrophoresis (ICEP) described in this chapter provide qualitatively predictable behaviors of electrophoretic motion of perfectly polarizable conducting particles, which can be used in various microfluidics and lab-on-a- chip applications.

CHAPTER V

CONCLUSIONS

This dissertation presents a fundamental study of non-linear induced-charge electrokinetic (ICEK) phenomena and the corresponding applications. A fundamental theory of induced charge electrokinetics was set up. It's found that a nonlinear induced surface charge distribution is immediately caused when a conducting object is immersed in an external applied electric field. The induced charge on the conducting surfaces results in a non-linear zeta potential distribution and an induced electric double layer when the surfaces contact with an aqueous buffer solution. The non-constant zeta potential gives a varying slipping velocity along the conducting surface, which produces micro vortexes in the liquid. A correction method was suggested to numerically estimate the induced zeta potential on the conducting surfaces. The numerical calculations of induced-zeta potential distribution matches well with reported analytical solutions.

Induced-charge electrokinetic flow (ICEKF) in a microchannel with embedded conducting hurdles was studied. A numerical scheme was provided to simulate the flow and concentration fields in the microchannel. The numerical results show that an induced non-uniform zeta potential distribution on the conducting surfaces causes varying electroosmotic flow velocity on the hurdle surfaces and circulating flows near the hurdles.

The simulation demonstrated that the species mixing can be enhanced significantly by the vortices near the hurdles. The mixing effect was validated experimentally using PDMS microchannels with embedded platinum hurdles. Both symmetric and non-symmetric hurdle placement patterns were tested in experiments, and the former showed a better ability to enhance the species mixing. The effects of hurdle geometry and the applied field on the flow mixing were investigated numerically. It's found that the degree of enhancement highly depends on the hurdle geometry. Among the three hurdle shapes tested in this study, the rectangle hurdle produces the strongest mixing effect. Also, the mixing can be further enhanced by adding more conducting hurdles in series in the microchannel because of the more flow vortices produced. The conducting hurdle method provides a way to make fast liquid delivery with a comparatively stable and high mixing efficiency under strong applied electric field.

A flow rate regulating effect can be obtained by adjusting the electric field strength applied through the microchannel when a pair of non-symmetric conducting hurdle is employed. This flow regulating effect can be used to achieve different flow rates in different directions and the closed-valve state (zero flow rate). The flow regulating effect depends on the dimensions of the converging-diverging section. In the cases where the downstream hurdle angle is close to the upstream hurdle angle, or a larger gap size is used, a larger critical electric field strength is required to attain the zero flow rate. The critical electric field is more strongly dependent on gap size than on the hurdle angle. To obtain effective flow regulating under a relatively weak electric field, the combination of larger downstream hurdle angle and smaller gap size is recommended.

The induced-charge electrophoretic (ICEP) motion of polarizable conducting particles was also theoretically investigated in this dissertation. A complete theoretical model of ICEP motion of conducting particles was established. A numerical approach based on Arbitrary Lagrangian-Eulerian (ALE) moving mesh technique was proposed to simulate the coupled particle-liquid multi-physics system. The induced-charge electrophoretic (ICEP) motions of conducting particles in a straight microchannel and ICEP particle-particle interactions in an unbounded large field were successfully simulated.

The numerical simulations indicate that an induced non-uniform zeta potential distribution on the conducting surface causes varying electroosmotic flow velocity on the polarizable particle's surface and circulating flows near the particle. It's numerically proven that, although the ICEP motion of an ideally polarizable conducting particle has a very different flow field from that of the EP motion of a non-conducting particle, the electrophoretic velocity is the same for the two cases under the assumption that the particles have the same initial zeta potential. It's also found that ICEP motion of ideally polarizable particles has a very strong wall-repelling effect when the particle is moving close to the channel wall, due to the interaction of the vortices around the particle and the channel walls. The effect depends on the electric field and the particle size. Higher electric field and larger particle size both give stronger wall-repelling. The polarizable particles show a clear trend of returning to the channel's centerline under the assumption that the particles have the same density as that of the liquid, making particle auto focusing possible. Particle's density will also affect its final steady level of the ICEP motion in the microchannel. This provides a potentially effective way for particle separation by density.

ICEP particle-particle interactions in an unbounded large field were also studied. The simulations show that an attracting effect can be obtained between the two polarizable conducting particles under a parallel applied field about the orientation of the two particles while a repelling effect is found under a vertical applied electric field. This is basically because of the non-symmetric micro vortexes generated between the two particles when they are placed close to each other. Under a parallel electric field, the micro vortexes are inward rotating, inducing a low pressure zone between the two particles, pushing the particles to get closer. Oppositely, under a vertical electric field, the vortexes are outward rotating, inducing a high pressure zone between the two particles, driving the particles to repel each other. The ICEP attracting or repelling effects depend on the particles' separation distance. When the particles are placed sufficient far away from each other with a separation distance greater than a critical value, the particles will not feel the existence of the others and the driving forces on the particles are balanced, thus the ICEP interacting effects will basically vanish. The effects also depend on the electric field strength and the particle size. Higher electric field strength gives stronger attracting or repelling effects between the two particles. Also, the particle's velocity only depends on the other particle's size. Smaller particle gives smaller driving force to others, but the speed of itself will not be affected if the other particle does fix the size.

This study provides fundamental understandings of ICEK flows in microchannels and ICEP motion of conducting particles. A new and simple ICEKF method for enhanced flow mixing and flow regulating with simple fabrication and easy operation was suggested and the qualitatively predictable behaviors of electrophoretic motion of perfectly polarizable conducting particles were also provided. The induced-charge electrokinetic phenomena described in this study can be used in various microfluidics and lab-on-a- chip applications.

REFERENCES

Acquaah, G. (1992) Practical Protein Electrophoresis for Genetic Research, Dioscorides Press, Portland.

Adrian RJ (1984) *Appl. Opt.* **23**:1690–1691

Allen, R. C. (1994) Gel Elec trophoresis of Proteins and Nucleic Acids: Selected Techniques, W. de Gruyter, New York.

Altria, K. D. (1996) Capillary Electrophoresis Guidebook: Principles, Operation, and Applications, Humana Press, New Jersey.

Anderson, J.L. (1985) *J. Colloid Interface Sci.* **105**: 45-54

Anderson, J.L., Idol, W.K. (1985) *Chem. Engng. Commun.* **38**: 93-106

Barker, S.L.R., Ross, D., Tarlov, M.J., Gaitan, M., Locascio, L. (2000) *Anal. Chem.* **72:** 5925-5929

Barany, S., Mishchuk, N.A., Prieve, D.C. (1998) *J. Colloid. Interf. Sci.* **207**: 240-250.

Bazant, M.Z., Ben, Y. (2006) *Lab on a chip.* **6**: 1455-1461

Ben, Y., Cang, H.C. (2002) *J. Fluid Mech.* **461**: 229-238

Ben, Y., Demekhin, E.A., Chang, H.C. (2004) *J. Colloid. Interf. Sci.* **276**: 483-497.

Biddiss, E., Erickson, D., Li, D. (2004) *Anal. Chem.* **76**: 3208-3213

Boleininger, J., Kurz, A., Reuss, V., Sönnichsen, C. (2006) *Phys. Chem. Chem. Phys.* **8**: 3824 – 3827

Borman, S. (1999) *Chemcial & Engineering News* **Feb**: 30-31

Cheng, J., Mitchelson, K. R. (2001) Capillary Electrophoresis of Nucleic Acids, Humana Press, New Jersey.

Chin, C.D., Linder, V., Sia, S.K. (2007) *Lab on a chip* **7**:41-57

DeMello, A.J. (2006) *Nature* **442**: 394-402

Dertinger, S.K.W., Chiu, D.T., Jeon, N.L., Whitesides, G.M. (2001) *Anal. Chem.* **73**: 1240-1246

Dittrich, P.S., Manz A. (2006) *Nature Reviews Drug Discovery* **5**: 210-218

Donea, J., Giuliani, S., Halleux, J. P. (1982) *Computer Methods in Applied Mechanics and Engineering* **33**: 689-723

Duffy, D.C., McDonald, J.C., Schueller, O.J.A., Whitesides, G.M. (1998) *Anal. Chem.* **70** 4974-4984

Dukhin A.S. (1986) *Colloid J. USSR* **48**: 376-381

Dukhin A.S., Murtsovkin, V.A. (1986) *Colloid J. USSR* **48**: 203-209

Dukhin S.S. (1991) *Adv. Colloid. Interf. Sci.,* **35:** 173-196

EI Rassi, Ziad (2002) Carbohydrate Analysis by Moden Chromatography and Electrophoresis, Elsevier, Boston.

El-Ali, J., Sorger, P.K., Jensen, K.F. (2006) *Nature* **442**: 403-411

Erickson, D., Li, D. (2002) *Langmuir* **18**: 1883-1892

Frazier, R. A. (2000) Capillary Electrophoresis for food analysis: method development, Royal Society of Chemistry, Cambridge.

Freemantle, M. (1999) *Chemical & Engineering News* **77**: 27-36

Gamayunov, N.I., Murtsovkin, V.A., Dukhin, A.S. (1986) *Colloid J. USSR* **48**: 197-203

Gangwal, S., Cayre, O.J., Bazant, M.Z., Velev, O.D. (2008) *Physical Review Letters* **100**: 058302

Harrison, D.J., Manz A., Fan, Z., Luedi, H., Widmer, H.M. (1992) *Anal. Chem.* **64**:1926-1932

Harrison, D.J., Fluri, k., Seiler, K., Fan, Z., Effenhauser, C.S., Manz, A. (1993) *Science* **261**: 895-897

Hau, W.L.W., Trau, D.W., Sucher, N.J., Wong, M., Zohar, Y. (2003) *J. Micromech. Microeng.* 13: 272-278

Hayes, M.A., Ewing, A.G. (1992) *Anal. Chem.* **64**: 512-516

Hu, H. H., Joseph, D. D., Crochet, M. J. (1992) *Theoretical and Computational Fluid Dynamics* **3**: 285-306.

Hunter R.J. (1981), Zeta Potential in Colloid Science: Principles and Applications, Academic Press, New York

Hughes, T. J. R., Liu, W. K., Zimmerman, T. K. (1981) *Computer Methods in Applied Mechanics and Engineering* **29**: 329-349.

Ismagilov, R.F., Rosmarin, D., Kenis, P.J.A., Chiu, D.T., Zhang, W., Stone, H.A., Whitesides, G.M. (2001) *Anal. Chem.* **73**: 4682-4687

Jacobson, S.C., Hergenroder, R., Koutny, L.B., Warmack, R.J., Ramsey, J.M. (1994) *Anal. Chem.* **66**: 1107-1113

Jacobson, S.C., Ramsey, J.M. (1997) *Anal. Chem.* **69**: 3212-3217

Jacobson, S.C., McKnight, T.E., Ramsey, J.M. (1999) *Anal. Chem.* **71:** 4455-4459

Jacobson, S.C., Ermakov, S.V., Ramsey, J.M. (1999) *Anal. Chem.* **71**: 3273-3276

Jeon, N.L., Chiu, D.T., Wargo, C.J., Wu, H. (2002) *Biomed. Microdevices.* **4**: 117-121

Keh, H.J., Anderson, J.L. (1985) *J. Fluid. Mech.* **153**: 417-439

Keren, D. F. (2003) Protein Electrophoresis in Clinical Diagnosis, Arnold, London.

Knight, J. (2002), Nature, ***418***: 474-475

Johnson, T.J., Ross, D., Gaitan, M., Locascio, L.E. (2001) *Anal. Chem.* **73**: 3656-3661

Landers, J. P. (1994) Handbook of Capillary Electrophoresis, CRC Press, London.

Laser, D.J., Santiago, J.G. (2004) *J. Micromech. Microeng.* **14**: R35-R64

Lee, C.S., Blanchard, W.C., Wu, C.T. (1990) *Anal. Chem.* **62**: 1550-1552

Lee, J., Hu, Y., Li, D. (2005) *Analytica Chimica Acta* **543**: 99-108

Levich, V.G. (1962) Physicochemical Hydrodynamics. Englewood Cliffs, N.J.: Prentice-Hall, Inc

Levitan, J.A., Devasenathipathy, S., Studer, V., Ben, Y., Thorsen, T., Squires, T.M., Bazant, M.Z. (2005) *Colloids and Surfaces A* **267**: 122-132

Lin, H., Storey, B.D., Oddy, M.H., Chen C-H., Santiago J.G. (2004) *Phys. Fluids.*, **16**: 1922-1935

Lin, Y., Wong, T.S., Bhardwaj, U., Chen, J.M., McCabe., E., Ho, C.M. (2007) *J. Micromech. Microeng.* **17**: 1299–1306

Liu, Y., Fanguy, J.C., Bledsoe, J.M., Henry, C.S. (2000) *Anal. Chem.* **72**: 5939-5944

Murtsovkin V.A. (1996) *Colloid Journal* **58**: 341-349

Neubert, R., Rüttinger, H. (2003) Affinity Capillary Electrophoresis in Pharmaceutics and Biopharmaceutics, Marcel Dekker, New York.

O'Brien, R.W., White, L.R. (1978) *J. Chem. Soc. Faraday II* **74**: 1607-1626

Oddy, M.H., Santiago, J.G., Mikkelsen, J.C. (2001) *Anal. Chem.* **73**: 5822-5832

Palfrey, S. M. (1999) Clinical Application of Capillary Electrophoresis, Humana Press, New Jersey.

Rose, K. A., Meier, J.A. Dougherty, G.M., Santiago, J. G. (2007) *Physical Review E* **75**: 011503.

Saintillan, D. Darve, E., Shaqfeh, E.S.G. (2006) *Journal of Fluid Mechanics* **563**: 223-259

Schasfoort, R.B.M., Schlautmann, S., Hendrikse, L., Van den Berg, A. (1999) *Science* **286**: 942-945

Seiler, K., Harrison, D.J., Manz, A. (1993) *Anal. Chem.* **65**: 1481-1488

Shim, S.Y., Lim, D.K., Nam, J.M. (2008) *Nanomedicine* **3**: 215-232

Shin, S.M., Kang, I.S., Cho, Y-K . (2005) *J. Micromech. Microeng.* **15**: 455-462

Shintani, H., Polonský, J. (1997) Handbook of Capillary Electrophoresis Applications, Blackie Academic and Professional, New York.

Sinha, G. (1999) *Popular Science* **Aug**: 48-52

Sinton D., Li, D. (2003) *Colloids & Surfaces A*. **222:** 273-283

Sparks, D., Smith, R., Straayer, M., Cripe, J., Schneider, R., Massoud-Ansari, S., Najafi, N. (2003) *TRANSDUCERS, Solid-State Sensors, Actuators and Microsystems, 12th International Conference on*, **1**: 300 – 303

Squires, T.M., Bazant, M.Z. (2004) *Physical Review Letters* **92**: 066101-1

Squires, T.M., Bazant, M.Z. (2004) *J. Fluid Mech.* **509**: 217-252

Squires, T.M., Bazant, M.Z. (2006) *J. Fluid Mech.* **560**: 65-101

Stroock, A.D., Weck, M., Chiu, D.T., Huck, W.T.S., Kenis, P.J.A., Ismagilov, R.F., Whitesides, G.M. (2000) *Phys. Rev. Lett.,* **84**: 3314-3317

Thibault, P., Honda, S. (2003) Capillary Electrophoresis of Carbohydrates, Humana Press, New Jersey.

Unger, M.A., Chou, H.P., Thorsen, T., Scherer, A., Quake, S.R. (2000) *Science* **288**:113-116

Wang S-C., Lai, Y-W., Ben, Y., Chang, H-C. (2004) *Ind. Eng. Chem. Res.* **43**: 2902-2911

Westermeier, R., Gronau, S. (2001) Electrophoresis in Practice: a Guide to Methods and Applications of DNA and Protein Separations, Wiley-VCH, New York.

Whitesides, G.M. (2006) *Nature* **442**: 368-373

Wickelgren, I. (1998) *Popular Science* **Nov**: 57-61

Woias, P., Hauser, K., Yacoub-George, E. (2000) Micro Total Analysis Systems, Kluwer Academic Publishers, Dordrecht, p. 277.

Wu., X., Kang, Y., Wang, Y., Xu, D., Li, D-Y., Li, D. (2008) *Electrophoresis*, published online 2008

Yang, Z., Goto, H., Matsumoto, M., Maeda R. (2000) *Electrophoresis* **21**: 116-119

Yariv, E. (2005) *Phys. Fluids*, **17**: 051702

Yasuda K. (2000) *Sens. Actuators B* **64**: 128-135

Ye, C., Li, D. (2002) *J. Colloid. Interf. Sci.,* **251**: 331-338

Ye, C., Li, D. (2003) *Proceedings of IMECE'03*, ASME, Washington, D.C., 603-611

Ye, C., Li, D. (2004) *J. Colloid. Interf. Sci.* **272**: 480-488

Yossifon, G., Frankel, I., Miloh, T. (2007) *Physics of Fluids*, **19**: 068105

Zhao, H., Bau, H.H. (2007) *Langmuir* **23**: 4053-4063